Magma Plumbing Systems along the Juan de Fuca Ridge

Thesis

Presented in Partial Fulfillment of the Requirements for the Degree Master of Science in the Graduate School of The Ohio State University

By

Lindsey Danielle Hernandez

Graduate Program in Earth Sciences

The Ohio State University

2020

Thesis Committee

Michael Barton, Advisor

Thomas Darrah

Elizabeth Griffith

Daniel Kelley

Abstract

The depth of magma storage beneath volcanoes has been a primary focus of recent geophysical and petrological research. Investigation of magma plumbing systems has important implications for volcanic hazard mitigation and eruption forecasting, and also for our understanding of the origin and evolution of magmas. This work is particularly important at mid-ocean ridges, as they are responsible for the formation of the majority of Earth's crust. Previous petrologic studies of mid-ocean ridges have suggested that olivine-plagioclase-clinopyroxene-liquid cotectic crystallization begins at mantle depths, which has far-reaching implications for our understanding of the mechanisms for crustal accretion. We demonstrate a procedure for processing pressure results using the Kelley & Barton (2008) geobarometer, which significantly changes the interpretation of these results. This process allows for high-resolution interpretation of the pressures, and thus depths, of partial crystallization in mafic systems. Application of this approach to data from the Juan de Fuca Ridge suggests that olivine-plagioclase-clinopyroxene-liquid cotectic crystallization occurs within the crust, and not in the mantle as suggested previously. The results suggest that partial crystallization along the ridge is polybaric. In the southern portion of the ridge, seismically imaged melt lenses are within range of the calculated pressures, however, the average pressures suggest that the majority of olivine-plagioclase-clinopyroxene-liquid cotectic crystallization occurs at greater depths than the imaged melt lenses. This suggests

multi-depth magma storage along much of the Juan de Fuca Ridge, with only the shallowest magma reservoirs being imaged by seismic studies.

Dedication

This work is dedicated to my family because they made my education possible. My parents, Jon and Tricia Lawson, have worked to give me opportunities that they never had. My grandparents, Brenda and Robert Lawson, are a light in the world and never fail to make me laugh. My husband, Josealberto Hernandez, sacrificed some of his dreams and worked hard to support my education. My brother, JT Lawson, taught me resiliency, tenacity, and the value of hard work. My husband's parents, Mirna and Elwin Hernandez, never fail to give advice whenever I need it. The rest of family, Heather, Zane, Marleny, Eduardo, Wilson, Ana, Edwin, Juan, Andrea, and Matías, are incredible cheerleaders and comic relief. I am very grateful for all of my family's unconditional love and encouragement.

Esta obra está dedicada a mi familia porque sin ellos, mi educación no habría sido posible. Mis papás, Jon y Tricia Lawson, se esforzaron para darme las oportunidades que ellos no tuvieron. Mis abuelos, Brenda y Robert Lawson, son una luz en este mundo y nunca fallan en hacerme reír. Mi esposo, Josealberto Hernández, sacrificó algunos de sus sueños y se esforzó para ayudarme a alcanzar mis sueños. Mi hermano, JT Lawson, me enseño el valor de trabajar duro. Mis suegros, Mirna y Elwin Hernández, nunca fallan en darme consejos cuando los necesito. Mis cuñados y sobrinos, Marleny, Eduardo, Wilson, Ana, Edwin, Juan, Andrea, Matías, Heather, y Zane, que siempre nos animan y llenan nuestra vida de alegría. Agradezco mucho el amor y el apoyo de toda mi familia.

Acknowledgments

I am grateful for the help of Dr. Jameson Scott, who taught me all I know about mid-ocean ridges and geobarometry, and who was generous with his time and kept me on track with this project. I addition, this work would not have been possible without the constant support, guidance, and proofreading from Dr. Michael Barton. I also thank Dr. Dan Kelley for his advice on this project and for generously providing edits, and to Dr. Liz Griffith and Dr. Tom Darrah for their helpful input.

I extend additional thanks to all of the people who have provided helpful comments, support, and advice throughout this project. I appreciate Ken Peterman's knowledge and his helpfulness in answering my constant questions. I am grateful for friendly discussion and encouragement from Ji-Eun Kim, Brittan Wogsland, and Casey Saup, who were always there to bounce ideas off of, proof various drafts and grant proposals, and who kept me sane. In addition, my success would not have been possible without the help and cariño of my husband, Josealberto Hernandez. I especially thank my mom, Tricia Lawson, for being the best proofreader, despite not understanding a thing about petrology. I also extend a special thank you to Dr. Erik Klemetti for his guidance and help throughout my undergraduate education and beyond, and to Dr. David Goodwin and Katie Scott for relentlessly encouraging me to go to graduate school.

Funding for this research was generously provided by The Friends of Orton Hall.

Vita

May 2012	Fairless High School
May 2016	B.S. Geosciences, Denison University
June 2016	International Volcanology Field School, University of Alaska Fairbanks
2018 to 2019	University Fellow, The Ohio State University, School of Earth Sciences
June 2019	Tinker Fellow, The Ohio State University, Center of Latin American Studies
2019 to Present	Graduate Teaching Associate, The Ohio State University, School of Earth Sciences

Publications

Hernandez, Lindsey. "Small Volcanoes with 'Big Footprints.'" Speaking of Geoscience (blog), December 17, 2019.

Hernandez, Lindsey. "New Research in the Latin American Dry Corridor Provides Graduate Students with International Research Experience to Address Global Resilience Against Climate Change." Speaking of Geoscience (blog), December 13, 2019.

Fields of Study

Major Field: Earth Sciences

Table of Contents

Abstract ii
Dedication iv
Acknowledgments v
Vita vi
Table of Contents viii
List of Tables x
List of Figures xi
Chapter 1. Introduction 1
1.1 Determining Depths of Magma Reservoirs 1
1.2 Geobarometry at Mid-Ocean Ridges 4
1.3 Hypotheses 5
Chapter 2. Calculation of Partial Pressures of Crystallization: Importance of Filtering Input Data and Results 6
2.1 Petrologic Methods 6
2.2 Kelley and Barton (2008) Method for Calculation of Pressures of Partial Crystallization 7
Cotectic Filtration Examples 12
2.3 Other Approaches for Calculation of Pressures of Partial Crystallization Based on the Yang et al. (1996) Method 17
2.4 Conclusions 20
Chapter 3. Magma Storage along the Juan de Fuca Ridge 32
3.1 Geologic Background 32
Evidence of Magma Plumbing Systems 33
Hotspot Influence 35
3.2 Methods 35
Data 36

Data Processing 36
3.3 KB Method Unfiltered Results 38
3.4 Discussion 38
Filtration 38
Comparison of Filtered and Unfiltered Results 41
Mantle vs. Crustal Crystallization 41
Interpretation of Calculated Pressures 42
Agreement with Seismic Data 43
Agreement with Previous Geobarometric Studies 45
Crustal Thickness 46
Locating Melt Lenses 46
Gale Correction vs. Non-correction 47
Modeling of LLDs and Water Variation Along the Ridge 48
Effects of P_2O_5 on Calculated Pressures 50
Temperature and Depth of Melt Segregation from the Mantle Source 51
3.6 Conclusions 53
Chapter 4. Conclusions 83
Bibliography 85
Appendix A. Hartley et al. (2018) Modified Python Script 98
Appendix B: Effect of Changing Error for H18 Method 101
Appendix C. Major Element PetDb.org Download Parameters 108
Appendix D. $Temp_{8.0}$, $Water_{8.0}$, $Fe_{8.0}$, & $Na_{8.0}$ Calculation 109
Appendix E. Wt.% Water PetDb.org Download Parameters 110
Appendix F. Link to Data Files 111

List of Tables

Table 2.1: KB results for the Hartley et al. (2018) dataset 21
Table 2.2: H18 results for the Hartley et al. (2018) dataset 22
Table 3.1: Summary table of the unfiltered JdFR dataset. 55
Table 3.2: Summary table of the filtered JdFR dataset. 56
Table A.1: H18 Pressures with 5% error and modified error. 107

List of Figures

Figure 2.1: Position of the olivine, plagioclase, clinopyroxene cotectic at different pressures (in GPa)....23
Figure 2.2: Schematic example of variation diagram filtration....24
Figure 2.3: Major oxide variation diagrams for Juan de Fuca Ridge, Endeavor segment (sub-segment 25), showing filtration......25
Figure 2.4: Incompatible and alkali oxide variation diagrams for the Juan de Fuca Ridge, Endeavor segment (sub-segment 25), showing filtration....26
Figure 2.5: Major oxide variation diagrams for the Hartley et. al (2018) Holuhraun melt inclusion data, showing filtration by the KB method....27
Figure 2.6: Incompatible and alkali oxide variation diagrams for the Hartley et. al (2018) Holuhraun melt inclusion data, showing filtration by the KB method.....28
Figure 2.7: Major oxide variation diagrams for the Hartley et al. (2018) Holuhraun glass data, showing filtration by the KB and H18 methods. 29
Figure 2.8: Incompatible and alkali oxide variation diagrams for the Hartley et al. (2018) Holuhraun glass data, showing filtration by the KB and H18 methods....30
Figure 2.9: Key variation diagrams for olivine, clinopyroxene, and plagioclase melt inclusions compared to groundmass glass....31
Figure 3.1: JdFR segments and selected transects showing segment morphology....57
Figure 3.2: Depths of axial magma chamber depths below the seafloor along the JdFR....58
Figure 3.3: Unfiltered pressure results along the strike of the JdFR....59
Figure 3.4: Sub-segment 3a filtration example showing major oxides....60
Figure 3.5: Sub-segment 3a filtration example showing incompatible oxides....61
Figure 3.6: Sub-segment 14 filtration example....62
Figure 3.7: Pressure vs. Latitude along the strike of the JdFR. 63

Figure 3.8: Filtered dataset pressure and depth vs. latitude along the JdFR.....64
Figure 3.9: Filtered pressure histograms for the Cleft, Axial, and Endeavor Segments.....65
Figure 3.10: Filtered pressure histograms for three sub-segments from the Cleft segment...66
Figure 3.11: Filtered pressure histograms for three sub-segments from the Axial segment...67
Figure 3.12: Filtered pressure histograms for three sub-segments from the Endeavor segment.....68
Figure 3.13: Incompatible elements and alkalis from the Endeavor segment filtered dataset69
Figure 3.14: Sub-segments with potential melt lenses 70
Figure 3.15: Modeled LLDs for the southern portion of the JdFR, anhydrous 71
Figure 3.16: Modeled LLDs for the southern portion of the JdFR, 0.1 wt. % water. 72
Figure 3.17: Modeled LLDs for the Axial segment, anhydrous 73
Figure 3.18: Modeled LLDs for the Axial segment, 0.1 wt. % water. 74
Figure 3.19: Modeled LLDs for the Endeavor segment, anhydrous. 75
Figure 3.20: Modeled LLDs for the Endeavor segment, 0.1 wt. % water 76
Figure 3.21: Modeled LLDs for the Endeavor segment, 0.3 wt. % water. 77
Figure 3.22: Water variation along the strike of the JdFR.....78
Figure 3.23: Modeled P_2O_5 for the unfiltered JdFR dataset.....79
Figure 3.24: Modeled P_2O_5 and observed P_2O_5 pressures vs. latitude for the unfiltered JdFR dataset. 80
Figure 3.25: Temperature along the strike of the JdFR.....81
Figure 3.26: Variations in $Fe_{8.0}$ and $Na_{8.0}$ along the JdFR.....82

Chapter 1. Introduction

Investigation of magma plumbing systems beneath volcanoes has important implications for volcanic hazard mitigation and eruption forecasting, as the understanding of magma storage conditions allows us to better understand eruptive triggers and eruptive styles (Iyer, 1992; Kelley & Barton, 2008; Cashman & Sparks, 2013; Chadwick et al., 2016). The depths at which magma is stored in volcanic systems is important for understanding the origin and evolution of magmas, and for the interpretation of data in seismic velocity studies (e.g. Iyer, 1992; Kelley & Barton, 2008). Therefore, magma storage depths have been a primary focus of geophysical and petrological research. This work is especially significant at mid-ocean ridges (MORs), as the depth of magma chambers has important implications for understanding the mechanisms for the accretion of oceanic crust, which covers approximately 60% of the Earth's surface (Pan & Batiza, 2002, 2003; Turcotte & Schubert, 2002; Kelley & Barton, 2008).

1.1 Determining Depths of Magma Reservoirs

Geophysical and geodetic methods, including gravimetry, interferometric synthetic aperture radar (InSAR), continuous GPS leveling, and seismic reflection and refraction surveys are useful for determining the depth, size, and shape of sub-surface magma reservoirs in active volcanic systems (e.g. Dzurisin, 2003; Battaglia et al., 2008; Carbotte et

al., 2008; Nagaoka et al., 2012; Nooner & Chadwick Jr., 2016). These methods are less reliable for studies of inactive volcanic systems. In addition, many geophysical methods are not useful for studies of submarine volcanoes. Seismic surveys are reliable for studies of magma storage at MORs, but require the deployment of instrumental arrays and time-consuming collection and interpretation of data.

Major-element geobarometers are petrologic geobarometery methods based on phase-relations of minerals and melt (e.g. Grove et al., 1992; Yang et al., 1996; Putirka, 1997). These can be used to determine the depths of melt storage for both active and inactive volcanic systems, and can be used in locations for which there is not seismic data. It is important to note that pressures calculated through major element geobarometers require that the liquid and mineral phases of study be in thermodynamic equilibrium. Therefore, a calculated pressure can be assumed to represent the depth at which the melt was stored or ponded, allowing the melt and crystal phases to obtain equilibrium. Pressures obtained from these methods are termed *pressures of partial crystallization*. Because these methods rely on thermodynamic equilibrium, the results of major element geobarometers are difficult to interpret if disequilibrium crystallization or magma mixing and assimilation have occurred.

Major element geobarometers have been extensively used to determine the depths of partial crystallization of mafic magmas, including MOR basalts (MORB) (e.g. Herzberg, 2004; Kelley & Barton, 2008; Wanless & Shaw, 2012; Neave et al., 2015; Wanless & Behn, 2017; Hartley et al., 2018; Neave et al., 2019). Mafic systems are ideal for geobarometric study, as they generally have only a small number of phases present (olivine ± plagioclase ± clinopyroxene ± melt), and thus have simple phase relationships (Grove et al., 1992; Neave & Putirka, 2017).

Clinopyroxene geobarometry has been used in mafic systems (e.g. Geiger et al., 2016; Neave & Putirka, 2017; Neave et al., 2019). Equations for this method were developed by Putirka et al. (1996), which are based on the pressure-dependent incorporation of jadeite (*jd*) into clinopyroxene. There have been several revisions to this geobarometer. The recent work by Neave and Putirka (2017) and Neave et al. (2019) emphasizes the difficulty in obtaining accurate pressures estimates using clinopyroxene geobarometry due to multiple factors. These include complex clinopyroxene zoning, which causes major element variations within a single crystal, non-equilibrium crystallization, and a strong dependence on oxygen fugacity, which is often an unknown intensive variable in volcanic systems, as Fe^{3+} contents cannot be measured via microprobe.

Liquid-olivine-plagioclase-clinopyroxene equilibrium geobarometry relies on mafic glass analyses, which are not affected by complex mineral zoning. This method is appropriate for obtaining results for large datasets. These geobarometers use the pressure dependence of the saturation surface between olivine (*ol*), plagioclase (*plag*), clinopyroxene (*cpx*), and liquid (*liq*), which has been extensively studied through experimental work (e.g. O'Hara, 1968; Elthon & Scarfe, 1984; Grove et al., 1992; Yang et al., 1996; Herzberg & O'Hara, 1998). *Liq-ol-cpx-plag* equilibrium geobarometers require that melts be multiply saturated with respect to *ol, plag,* and *cpx*, and therefore cannot accurately predict pressures of off-cotectic crystallization. Various *liq-ol-cpx-plag* equilibrium geobarometers have been applied to mafic magmas (e.g. Yang et al. 1996; Ariskin, 1999; Herzberg, 2004; Villiger et al., 2007; Kelley & Barton, 2008; Hartley et al., 2018).

The results from different *liq-ol-cpx-plag* equilibrium methods sometimes disagree. This, in part, may be due to interlaboratory biases in analyses (e.g. Grove et al., 1992; Yang et

al., 1996; Gale et al., 2013). Yang et al. (1996) and Michael and Cornell (1998) show that results using the empirical equations derived by Yang et al. (1996) are sensitive to analytical uncertainties, which highlights the importance of using pseudoternary projections to reduce this sensitivity and assure that samples are lying on the *liq-ol-cpx-plag* cotectic. Much of the recent work in *liq-ol-cpx-plag* equilibrium geobarometry has focused on addressing these concerns (e.g. Grove et al., 1992, Michael & Cornell, 1998; Herzberg 2004; Kelley & Barton, 2008; Hartley et al., 2018).

1.2 Geobarometry at Mid-Ocean Ridges

MORs are responsible for the formation of 60% Earth's crust (Turcotte & Schubert, 2002), yet many unanswered questions remain about crustal accretion processes, the characteristics and depths of sub-surface magma bodies, and the dependence of these variables on the ridge spreading rate. Due to the difficulty of performing seismic studies beneath the ocean, seismic data are not available for all MORs or all segments of MORs. Therefore, petrologic studies are important to give insight into magma storage depths at MORs.

Recent petrologic and geophysical studies have suggested that crystallization at MORs is polybaric (e.g. Canales et al., 2009; Wanless & Shaw, 2012), which indicates that magma is likely stored in a series of stacked sills (Kelemen, 1997) or as a dispersed crystal mush (Sinton and Detrick, 1993; Maclennan et al., 2004). Several workers using petrologic methods have found evidence for lower-crustal to upper-mantle crystallization, especially at slow-spreading ridges (e.g. Herzberg et al., 2004; Villiger et al., 2007; Wanless & Shaw, 2012; Wanless & Behn, 2017; Bennett et al., 2019). The possibility of high-pressure crystallization

beneath MORs and its possible correlation to ridge spreading rate requires additional investigation.

1.3 Hypotheses

Based on the work described above, along with previous findings by Scott (2017), hypotheses are proposed for the characterization of magma storage at MORs:

1) Current *liq-ol-cpx-plag* equilibrium geobarometry methods can accurately constrain the depths of magma storage. However, in order to obtain the most reliable estimate of depths of *liq-ol-cpx-plag* cotectic crystallization, it is important to remove all potentially ambiguous samples from the datasets under consideration.
2) The majority of *liq-ol-cpx-plag* cotectic crystallization at intermediate-rate spreading ridges occurs primarily within the crust, contrary to the conclusions of previous studies (e.g. Herzberg, 2004; Villiger et al., 2007; Wanless & Behn, 2017).
3) Proper filtration of samples significantly changes the interpretation of pressure results for MORs.

Chapter 2. Calculation of Partial Pressures of Crystallization: Importance of Filtering Input Data and Results

2.1 Petrologic Methods

There are several petrological methods for determining pressures, and thus depths, of partial crystallization of mafic magmas. Yang et al. (1996) describe an elegant method of geobarometry that requires only major element analyses of mafic glasses for the calculation of pressures. This makes this method ideal for studying MORs, as mafic glasses are abundant in submarine environments due quenching of extruded lavas, and a large database of MORB major element analyses already exists.

To calculate pressures, the Yang et al. (1996) method uses experimentally established phase equilibrium constraints between the *liq-ol-plag-cpx* boundary**.** The location of this boundary is pressure-dependent (e.g. O'Hara, 1968; Grove et al., 1992), and thus can be used to determine the pressure at which the liquid and crystals last obtained equilibrium. Yang et al. (1996) fit four empirical equations to describe this relationship based on carefully selected experiments in which a close approach to equilibrium was demonstrated. These are used to calculate the position of the *liq-ol-cpx-plag* cotectic as a function of pressure for a specific composition, and project the positions of the cotectic onto pseudoternary planes. This method allows for estimation of the crystallization pressure for any basaltic melt in equilibrium with *ol*, *plag*, and *cpx*.

The Yang et al. (1996) method is calibrated for basaltic and mildly alkaline magmas, and cannot be used with confidence to determine pressures of partial crystallization for silica-rich magmas (SiO_2 > 52 wt.%). Also, the calculated pressures represent the lowest pressure at which the melt was in equilibrium with *ol*, *plag*, and *cpx* (Kelley & Barton, 2008). Any chemical signature of an earlier stage of magma crystallization at higher pressure may be overprinted by partial crystallization at lower pressures unless the magma has ascended rapidly. Lastly, because this method is based on the comparison of natural liquid compositions with experimental liquid compositions, whole-rock compositions cannot be used for these calculations because, except in rare cases, they do not represent the compositions of the liquids (Kelly & Barton, 2008).

2.2 Kelley and Barton (2008) Method for Calculation of Pressures of Partial Crystallization

Kelley and Barton (2008) use the Yang et al. (1996) equations to directly calculate pressures based on projection parameters of melt compositions from *plag* onto the plane *ol-cpx-qtz* and from *ol* onto the plane *plag-cpx-qtz*, following the procedure by Yang et al. (1996). The technique yields six pressure values for each sample (Figure 2.1). The average value is taken as the pressure of partial crystallization, and all values are used to calculate the uncertainty (1σ) associated with the average pressure. Comparison with experimental data suggests that the combined accuracy and precision of calculated pressures is ~126 MPa (1σ) (See Kelley & Barton, 2008, for discussion). This approach is hereafter called the KB method, and the Excel program CoPressCalc, provided by Kelley and Barton (2008), is used to carry out these pressure calculations.

Because the method assumes that samples lie on the *liq-ol-cpx-plag* cotectic, the significance of pressure results calculated for off-cotectic samples is unclear. Therefore, in order to find the best pressure estimate, it is necessary to remove these samples from the dataset. The criteria for this process are explained below.

Filtering Input Data:

1. **Data quality check:** Because this method cannot accurately predict pressures of off-cotectic crystallization, it is important that the data used for geobarometric study are within the assumptions made for the method. First, it is imperative to ensure that the data used in pressure calculations are basaltic glass and complete with respect to major oxides. Glass analyses must be used, as whole-rock data do not unambiguously represent melt compositions (Kelley & Barton; 2008). Additionally, samples that have incomplete analyses for major oxides, with the exception of P_2O_5, should be removed from the dataset. Incomplete major oxide data will result in erroneous pressure results.

   Although P_2O_5 is of low abundance in basalts and is often not included as part of major element analyses, we find that wt.% P_2O_5 can be modeled. P_2O_5 contents are included in the Yang et al. (1996) equations to account for CaO present in apatite [$Ca_5(PO_4)_3(OH, F, Cl)$]. If P_2O_5 is taken to be 0 wt.%, apatite crystallization will not be accounted for. This will increase the wt.% CaO assigned to *cpx*, and underestimate pressures. Unknown wt.% P_2O_5 can be modeled by a power curve through observed P_2O_5 values for the same location.

An example of this is given for samples from the Juan de Fuca Ridge, where the following equation is used to model wt.% P_2O_5:

$$Model\ P_2O_5\ = 16.10 \pm 0.21\ \times\ MgO^{-2.37\pm0.11}$$

The fit of this curve to the dataset is shown in Figure 3.23. This model provides an acceptable fit for samples with MgO > 4 wt.%. Therefore, the wt.% P_2O_5 of samples with MgO < 4 wt.% should not be modeled using this method. With low MgO samples excluded, the effect on calculated pressures is minor. The average change in calculated pressure is minor (1 ± 23 MPa), with a maximum change of +174 MPa, which is just outside the 1σ error of the method.

2. **Conversion to FeO_T:** Fe_2O_3 should be converted to FeO_{Total} before pressure calculation. This is done to maintain consistency with the experimental dataset used to calibrate the method, as Fe from microprobe data is reported as FeO_{Total}.

Correction of Results:

3. **Split dataset into small groups or sub-segments:** In some cases, it may appropriate to subdivide the dataset into smaller parts in order to study individual magmatic systems. In the case of studies of single eruptions from individual volcanoes, there may be no need to subdivide data, as the eruption can be assumed to be sourced from a single magmatic system. For studies of multiple eruptions, however, it is appropriate to divide data by eruption in order to unravel possible changes in the plumbing system with time or explore evidence for multiple reservoirs at different depths.

For studies of entire mid-ocean ridges, the subdivision of data can provide better insight into changes in magma storage depths along the ridge. The extent of submarine lava flows can provide one estimate for the area fed by individual magma plumbing systems. Near the Axial Volcano on the Juan de Fuca Ridge, for example, recent lava flows erupted over a length of 0.17° (20 km), 0.29° (35 km), and 0.10° (13 km) in 2015, 2011, and 1998, respectively (Clague et al., 2018). Clague et al. (2018) propose that these lavas were sourced from a recharged resident magma body, and so it can be assumed that they were derived from a single melt lens and transported along the strike of the ridge by dikes. Therefore, 0.10°–0.30° latitude (10–40 km), may be an appropriate length over which lavas are sourced from a single magma plumbing system.

4. **Correction for weight of water column:** If samples are submarine, correction of pressures to account for the overburden of the overlying water column provides the actual depth of the magma beneath the earth's surface, and facilitates comparison with seismic methods. The pressure at the base of the water column should be calculated using the reported elevation of the ridge at the sample collection site, and this quantity should be subtracted from the calculated pressure.
5. **Removal of samples with high error:** Samples that have a 1σ error in calculated pressure greater than the error of the method (126 MPa) show poor agreement between the sample and the position of the *liq-ol-cpx-plag* cotectic calculated in two projections. This indicates that these samples likely do not lie on this cotectic and that these pressures are unreliable.

6. **Removal or correction of samples with negative pressures:** This method may return negative pressures results, which are clearly impossible. If pressures are less negative than -126 MPa, they should be corrected to the pressure at the seafloor (0.1 MPa), as they are within error of the seafloor surface. Pressures more negative than -126 MPa are erroneous and should be removed from the dataset.
7. **Cotectic Filtration:** The final step of correcting the results is removal of samples that do not have compositions consistent with the crystallization of *ol*, *plag*, and *cpx*, termed *filtration*. This is established using variation diagrams on which selected major oxides are plotted as a function of wt.% MgO. Both plagioclase and clinopyroxene remove CaO and Al_2O_3 from evolving basaltic magma. Therefore, it is necessary to use plots of CaO/Al_2O_3 versus MgO to determine if one or both of these phases are crystallizing (Figure 2.2). Glasses with compositions that do not plot along and within well-defined data arrays with trends consistent with simultaneous crystallization of *ol*, *plag* and *cpx* (see Herzberg, 2004; Kelley & Barton, 2008) are outside the assumptions made for *ol-plag-cpx-liq* cotectic crystallization, and thus the significance of their pressure results is unclear. Therefore, in order to obtain the best estimate of pressures of crystallization, these samples should be removed from the dataset. This process is described in the section below.

Cotectic Filtration Examples

Liq-ol-cpx-plag cotectic filtration is done through the identification of inflections on MgO vs. CaO, CaO/Al_2O_3, and Al_2O_3 plots. These inflections indicate the onset of crystallization of a new phase, which pulls the composition of the melt away from that phases' control line along a predictable liquid line of descent (LLD). This process is shown in Figure 2.2, where an idealized LLD is shown for the major oxides that are most affected by *ol*, *plag*, and *cpx* crystallization. A LLD represents the average crystallization path of a coherent array of samples and changes slope according to phase relationships. Therefore, the slope of the LLD can be used to determine which minerals are crystallizing at a given wt.% MgO. A negative slope indicates that only *ol* is crystallizing, whereas a positive slope indicates that *ol*, *plag*, and *cpx* are crystalizing.

The crystallization trends for a single magma reservoir should from a tight array. Scatter may indicate the presence of multiple magma reservoirs, or that processes other than *ol-plag-cpx-liq* cotectic crystallization are occurring. Therefore, samples that lie far from the LLD are also removed during cotectic filtration, as these samples are not consistent with the evolution of the other samples, or they may be poor-quality analyses. Therefore, these samples give pressure results that are outside the assumptions made for *ol-plag-cpx-liq* cotectic crystallization for which the meaning is not clear. In order to obtain the most reliable estimate of depths of crystallization, it is important to remove all potentially ambiguous samples. For the purposes of this study, the removal of these samples is done through visual analysis. However, a mathematical approach involving linear regression may also be employed, where samples outside an error envelope are excluded from the final dataset.

To illustrate the filtration process, an example is presented in Figure 2.3 and 2.4 from a small subset of data between 47.54 and 47.73 °N (sub-segment 25, n=33) on the Endeavor segment of the Juan de Fuca Ridge:

- There is a clear inflection near 8 wt.% MgO in the MgO vs. Al_2O_3 and MgO vs. CaO plots. There is a positive correlation between MgO and Al_2O_3, which is consistent with the crystallization of only *ol*, so these three samples can be removed.
- Five additional samples form a negative MgO vs. CaO trend showing an inflection near 7 wt.% MgO and 11.5 wt.% CaO. This inflection likely indicates that these samples are also not on the *liq-ol-cpx-plag* cotectic and should be removed.
- The above five samples are part of a conspicuous low CaO/Al_2O_3 trend, along with three additional samples. Because these samples lie far from the LLD defined by the majority of the samples, it is not clear if these samples are part of the LLD array. These samples are also above the LLD for wt.% Al_2O_3, which is difficult to explain by fractional crystallization. It has been demonstrated that interactions between crystal mushes and melts are relatively common along mid-ocean ridges (e.g. Dick et al., 2002; Lissenberg & Dick, 2008; Lissenberg & MacLeod, 2016; Yang et al., 2019). Experimental work shows that these interactions result in high wt.% MgO and Al_2O_3 (Yang et al., 2019). Therefore, these three samples should also be removed from the dataset, as they likely represent the effects of assimilation rather than *liq-ol-cpx-plag* cotectic crystallization along a LLD.

Before filtration, the average pressure of these samples was 75.5 MPa, with a maximum of 665.2 MPa (23 km below the seafloor, b.s.f.), and a minimum of 0.1 MPa (0 km b.s.f.). After the removal of the eleven samples as described above, the average pressure is reduced to 14.9 MPa, with a range of 0.1 to 86.7 MPa (3 km b.s.f.). This demonstrates that cotectic filtration significantly changes the interpretation of the pressure results for this location.

An additional example of cotectic filtration is presented for glass data from the 2014–2015 Holuhraun eruption in the Bárðarbunga volcanic complex in Iceland (from Hartley et al., 2018). This dataset consists of groundmasses (n=9), embayments (n=3), and melt inclusions (MIs) (n=106). The MI glasses are hosted in plagioclase (n=91), olivine (n=10), and clinopyroxene (n=5). Because the major element compositions of MIs are subject to alteration by post-entrapment crystallization (PEC), they must be corrected for PEC and care must be taken in the interpretation of their pressure results. These MI data were corrected for PEC by Hartley et al. (2018).

The variation diagrams used for filtration are shown in Figures 2.5, 2.6, 2.7 and 2.8. Details on the filtration procedure are described below:

MI Filtration (Figures 2.5 & 2.6)

- Eight samples lie before an inflection in the LLD near MgO 9 wt.% on the MgO Vs. Al_2O_3 and MgO Vs. CaO plots. These samples are crystallizing only *ol* and should be removed.
- There is considerable scatter on the MgO vs. CaO plot, which may not be due to *liq-ol-cpx-plag* cotectic crystallization along a LLD. The nine samples below the main LLD near 8 wt.% MgO appear to define different LLDs. Due to the negative slope

of this array, these samples are likely not on the *liq-ol-cpx-plag* cotectic and should be removed. The nine samples above the main LLD show considerable scatter in P_2O_5, K_2O, and Na_2O, which may indicate crustal interaction. Therefore, these samples are also removed from further consideration.

- Seven samples with 7.8–8.8 wt.% MgO lie below the LLD defined by the majority of the data on the MgO vs. Al_2O_3 plot. These samples lie before an inflection on the LLD and therefore do not have compositions consistent with *liq-ol-cpx-plag* cotectic crystallization. Thus, these samples are also removed.
- Four samples near 6.5 wt.% MgO have high FeO_{Total} relative to the main trend. These samples also have high K_2O and Na_2O. While FeO_{Total} and TiO_2 can be expected to increase during *liq-ol-cpx-plag* cotectic crystallization until the onset of Fe and Ti oxide crystallization, these samples are at a greater distance from the LLD than would be expected from scatter in the data. The high K_2O and Na_2O further support that these samples do not have compositions consistent with *liq-ol-cpx-plag* cotectic crystallization. Therefore, these four samples are also removed.
- Seven samples were removed for Na_2O and K_2O lying off of the LLD defined by the vast majority of the data (MgO 6.12–6.94 wt.%). Scatter in these oxides can indicate crustal interaction, and therefore these samples may not lie on the *liq-ol-cpx-plag* cotectic.

Groundmass and Embayment Filtration (Figures 2.7 & 2.8)

- One sample with MgO near 6 wt.% has high Al_2O_3, low FeO_T, TiO_2, and Na_2O, which are at a greater distance from the LLDs than would be expected from scatter in the data. Thus, this sample is also removed from the dataset.

The calculated pressures for the unfiltered and filtered datasets are shown in Table 2.1. These average estimated pressures of partial crystallization are within error of the preferred pressure of 177±62 MPa for Bárðarbunga reported by Kelley and Barton (2008).

Cotectic filtration removes 40% of the MI samples (n=63 remaining). The majority of the *ol* MIs are removed in this process. To assess if these samples were corrected for a sufficient % PEC, or to assess if PEC correction may have pushed these MI compositions off of the *liq-ol-cpx-plag* cotectic, these samples are compared to an additional 65 samples of erupted groundmass glasses from older eruptions of Bárðarbunga volcanic complex (Figure 2.9; Data Sources: Mørk, 1984; Meyer et al., 1985; Hansen & Grönvold, 2000; Halldórsson et al., 2008).

In Figure 2.9, LLDs for the groundmass glasses are shown for MgO vs. FeO_T and MgO vs. CaO, for *ol* and *cpx* MIs, and *plag* MIs, respectively. The majority of the *ol* MIs lie above the groundmass LLD, with higher FeO_{Total} than the groundmass glasses. This may indicate that these MIs were corrected for an anomalously high % PEC, pulling them off the *liq-ol-cpx-plag* cotectic. The *plag* MIs, however, show agreement with the groundmass LLD, suggesting that the *plag* MIs were corrected appropriately.

2.3 Other Approaches for Calculation of Pressures of Partial Crystallization Based on the Yang et al. (1996) Method

Other workers have used different approaches in the application of the Yang et al. (1996) method for calculation of pressures of partial crystallization. Michael and Cornell (1998) use equations 1–3 from Yang et al. (1996) without calculation of projection parameters. They find that that the first and third equations (describing the Al and Mg molar fractions) are particularly sensitive to analytical error, and that small changes in the wt.% of the major oxides can have large effects on the pressure results. Michael and Cornell (1998) therefore use only the second equation, describing the Ca molar fraction.

Similar to Michael and Cornell (1998), Hartley et al. (2018) use the Yang et al. (1996) equations without the calculation of projection parameters. The Hartley et al. (2018) approach, however, uses a statistical method for the calculation and filtration of pressures, called the H18 method hereafter. For this technique, equations 1–3 from Yang et al. (1996) are used to find the model pressure that minimizes the χ^2 value for measured and observed glass compositions:

$$\chi^2 = \sum_{i=1}^{3} \left[\frac{X_i^o - X_i^Y}{\sigma_{X_i}} \right]^2 \qquad (1)$$

In equation [1], X_i^o and X_i^Y are the observed and predicted cation mole fractions, respectively, and σ represents the analytical uncertainty for EPMA analyses of major element oxides in glasses. Hartley et al. (2018) use ±5% for this value after the precision of major oxide analyses found by Neave et al. (2015). The H18 method uses a χ^2 vs. pressure curve, to determine if the pressure values from each equation are in agreement, where samples with

poor fit are deemed to lie off of the *liq-ol-cpx-plag* cotectic and are excluded from the results. Details on this process can be found in Hartley et al. (2018).

Because this approach does not calculate projection parameters onto pseudoternary diagrams to verify that samples are on the *liq-ol-cpx-plag* cotectic, these results may be subject to error, as discussed by Michael and Cornell (1998). In addition, Hartley et al. (2018) do not account for errors for all of the oxides and focus solely on those for Al_2O_3, CaO, and MgO, which may be an additional source of error.

It is also important to note that the 5% precision for major element analyses used for σ in equation [1] is a conservative estimate, and changes in this value affect pressure results significantly. Most microprobe data have a precision near ±1% for abundant oxides (e.g. Michael & Cornell, 1998; CAMECA 2015; University of Michigan Electron Microbeam Analysis Lab, personal communication). Modification of the value of σ significantly changes the pressure results using the H18 method. This is demonstrated using the total dataset (n=219) from the Bárðarbunga volcanic complex (i.e. all samples from Mørk, 1984; Meyer et al., 1985; Hansen & Grönvold, 2000; Halldórsson et al., 2008; Hartley et al., 2018). If σ is modified to 1% for Ca and Al, and 0.7% for Mg, the H18 method removes 95% of the samples (n=209). However, the calculated pressures change only by 0 to +4 MPa. A summary of these data and results can be found in Appendix B. This modification uses a more accurate value for σ; however, it removes a significant portion of the data such that the results are no longer useful for petrologic study. While further discussion of the cause of this is outside the scope of this study, this should draw into question the validity of the H18 method.

A Python script modified from that provided by Hartley et al. (2018) is listed in Appendix A and used for calculation of H18 pressures for the 2014–2015 Holuhraun eruption dataset described above. This is done using 5% for σ, as published. The H18 method removes 66% of the corrected MI samples (n=36 remaining), and 50% of the glass and embayment samples (n=6 remaining) (Table 2.2). Pressure results from the H18 method are within error of the KB results presented here. These results are also within error of the preferred pressure of partial crystallization for Bárðarbunga (177±62 MPa) reported by Kelley and Barton (2008), and within error of the pressure results for this dataset using the KB method (Table 2.1).

Despite the differences in filtration procedures between the KB and H18 methods, the average pressures from both methods are within error of each other, and the pressure ranges from both methods are reduced upon filtration (Tables 2.1 and 2.2). However, the pressure results of the KB method indicate slightly shallower depths of partial crystallization than do the H18 results. This is contrary to the discussion by Hartley et al. (2018) in their comparison of these methods, as they compare the filtered H18 pressures to the raw KB pressures. In addition, in this study, the H18 method removes 27% more samples than does the KB method. From variation diagrams, however, many of the samples removed by the H18 method appear to lie on the *liq-ol-cpx-plag* cotectic. Hartley et al. (2018) call these samples *false negatives*, and determine that it is more important to exclude false positives than to avoid eliminating a larger number of samples than necessary. However, exclusion of large numbers of samples that lie on the *liq-ol-cpx-plag* cotectic can be problematic, as information about the depths of magma storage is lost and the number of samples removed may not allow strong conclusions to be made from small datasets.

2.4 Conclusions

The Yang et al. (1996) method has been widely used for studies of the depths of storage of mafic magmas. The H18 and KB methods represent different approaches to *liq-ol-cpx-plag* geobarometry based on the work of Yang et al. (1996). The KB method more closely follows the Yang et al. (1996) procedure through its use of pseudoternary projections.

Because the Yang et al. (1996) method assumes that samples lie on the *liq-ol-cpx-plag* cotectic, the significance of pressure results calculated for off-cotectic samples is unclear. Therefore, in order to find the best pressure estimate, it is necessary to remove these samples from the dataset. We describe a procedure for filtration of input data prior to pressure calculation using the KB method, and a procedure for correction of pressure results. This process removes samples that are outside the assumptions made for *liq-ol-cpx-plag* cotectic crystallization, for which the meaning for their pressure results is not clear. This filtration procedure significantly changes the interpretation of the pressure results, and allows for the best estimate of pressures of partial crystallization.

Melt Inclusion Results							
	n	Avg P (MPa)	Std Dev	Max (MPa)	Min (MPa)	Max (km)	Min (km)
KB: Raw	106	210	120	450±80	-10±10	16.±3.0	-3.4±0.5
KB: Filtered	63	240	80	360±50	50±20	12.7±1.8	1.6±0.7

Groundmass and Embayment Glass Results							
	n	Avg P (MPa)	Std Dev	Max (MPa)	Min (MPa)	Max (km)	Min (km)
KB: Raw	12	270	120	430±70	20±40	15.1±2.5	0.7±1.4
KB: Filtered	11	260	120	430±70	20±40	15.1±2.5	0.7±1.4

Table 2.1: KB results for the Hartley et al. (2018) PEC corrected melt inclusions. The depth, in km below sea floor (b.s.f.), is calculated assuming a crustal density of 2900 kg/m^3.

Melt Inclusion Results							
Method	n	Avg P (MPa)	Std Dev	Max (MPa)	Min (MPa)	Max (km)	Min (km)
H18: Raw	106	300	160	670±130	-250±130	23.6±4.6	-8.9±4.6
H18: Filtered	36	350	170	530±130	150±130	18.6±4.6	5.4±4.6
Groundmass and Embayment Glass Results							
Method	n	Avg P (MPa)	Std Dev	Max (MPa)	Min (MPa)	Max (km)	Min (km)
H18: Raw	12	210	80	310±130	60±130	10.9±4.6	2.1±4.6
H18: Filtered	6	230	80	310±130	120±130	10.9±4.6	4.2±4.6

Table 2.2: H18 results for the Hartley et al. (2018) glasses. The depth, in km below sea floor (b.s.f.), is calculated assuming a crustal density of 2900 kg/m^3.

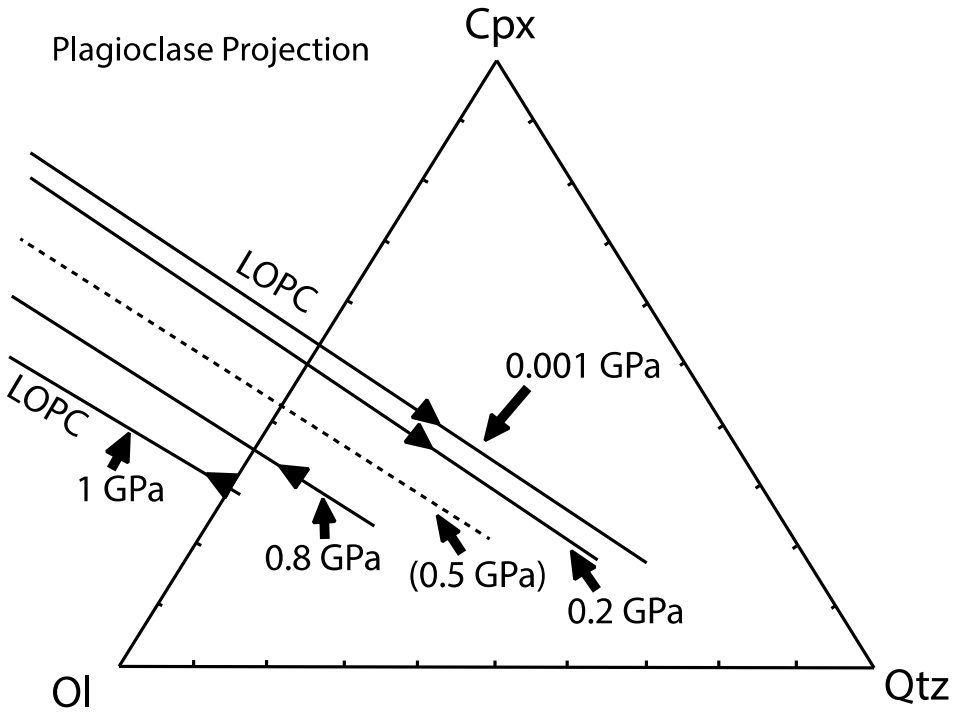

Figure 2.1: Position of the olivine, plagioclase, clinopyroxene cotectic at different pressures (in GPa). Projected from plagioclase onto the *ol-cpx-qtz* pseudoternary plane. Cotectic locations determined by experimental data. From Kelley & Barton (2008).

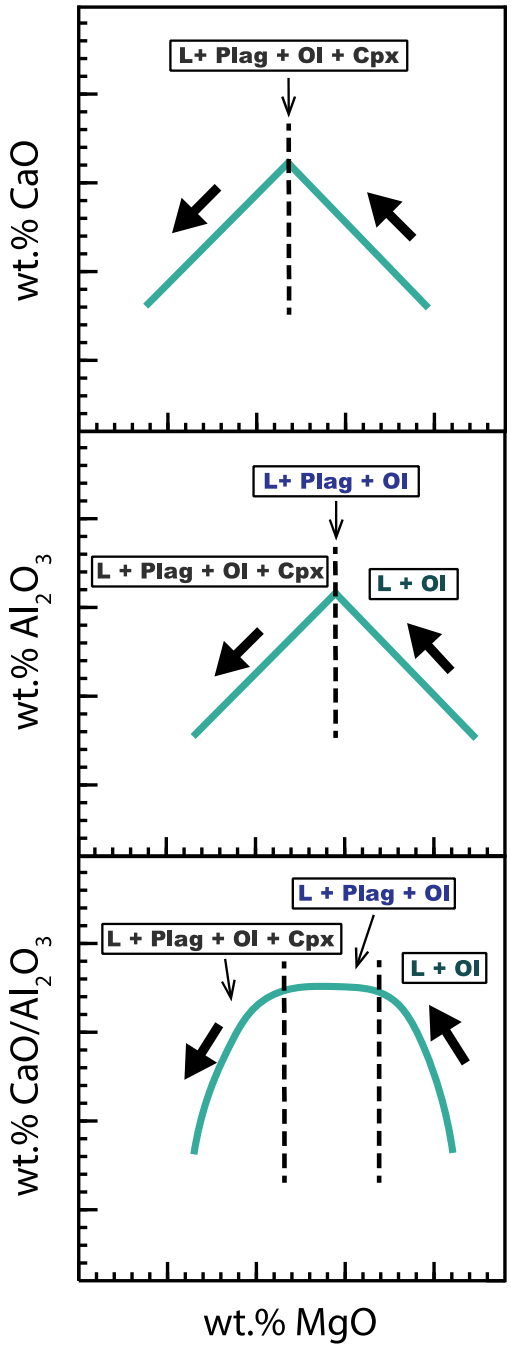

Figure 2.2: Schematic example of variation diagram filtration. Green curves indicate expected liquid line of descent (LLD) during crystallization, proceeding in the direction of large arrows from high wt.% MgO to low wt.% MgO. Labels indicate mineral phases crystallizing along the curve: L = liquid, Ol = olivine, Plag = plagioclase, and Cpx = clinopyroxene.

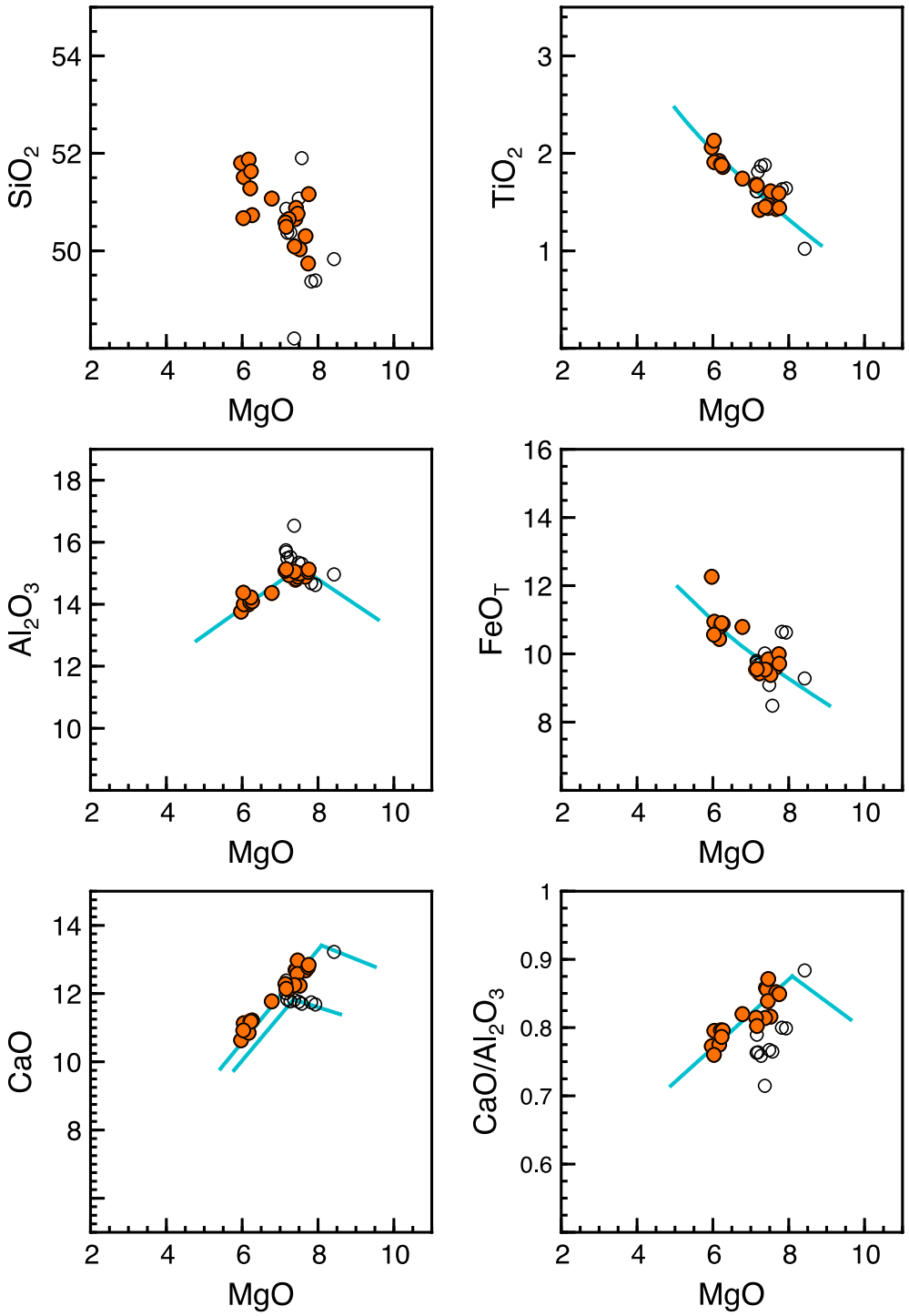

Figure 2.3: Major oxide variation diagrams for Juan de Fuca Ridge, Endeavor segment (sub-segment 25), showing filtration. Open circles are raw data. Orange filled circles are samples remaining after filtration. All axes are in wt.%. Blue lines are possible liquid lines of descent, which describe the approximate crystallization trend of these samples.

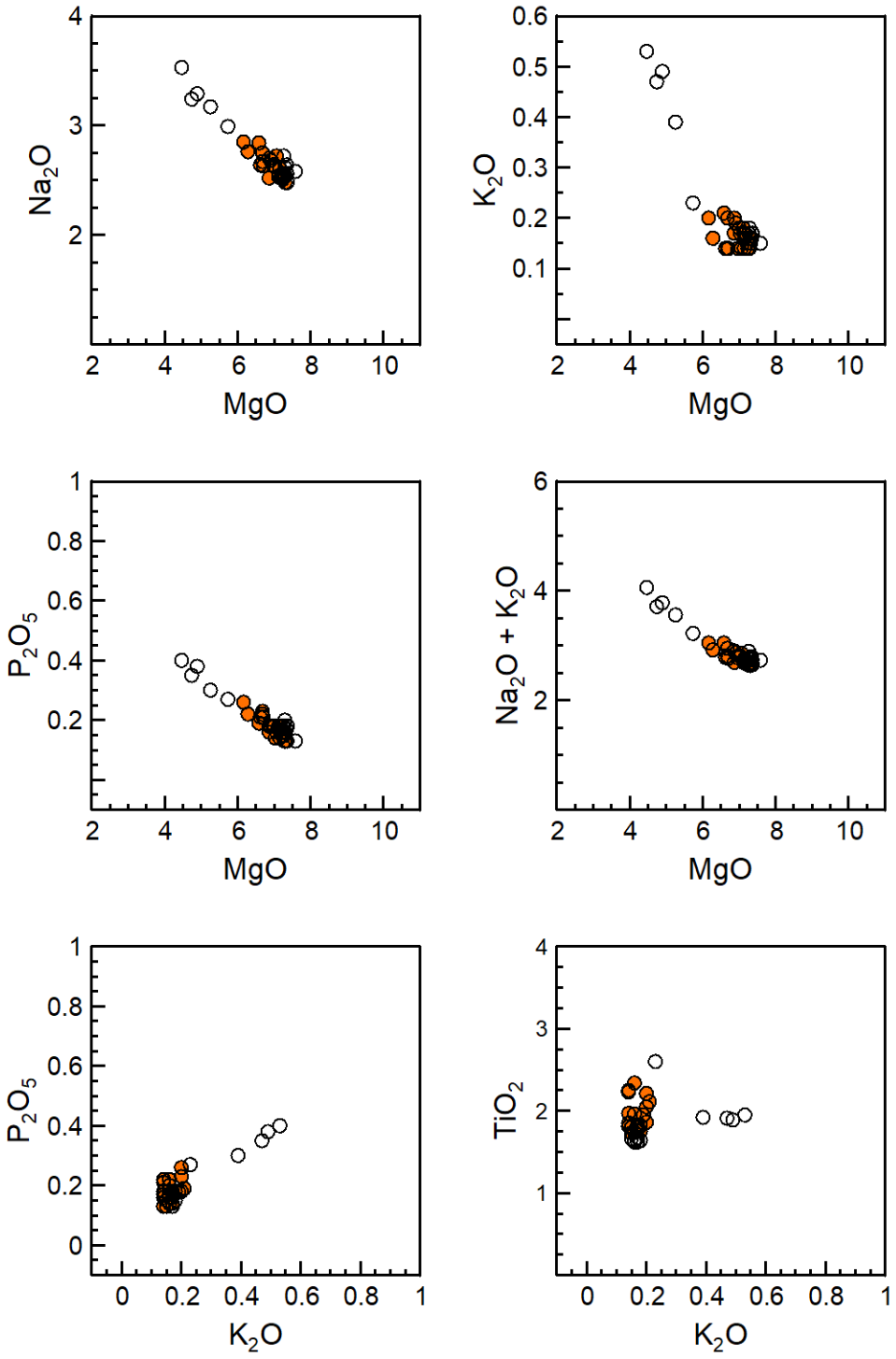

Figure 2.4: Incompatible and alkali oxide variation diagrams for the Juan de Fuca Ridge, Endeavor segment (sub-segment 25), showing filtration. Open circles are raw data. Orange filled circles are samples remaining after filtration. All axes are in wt.%.

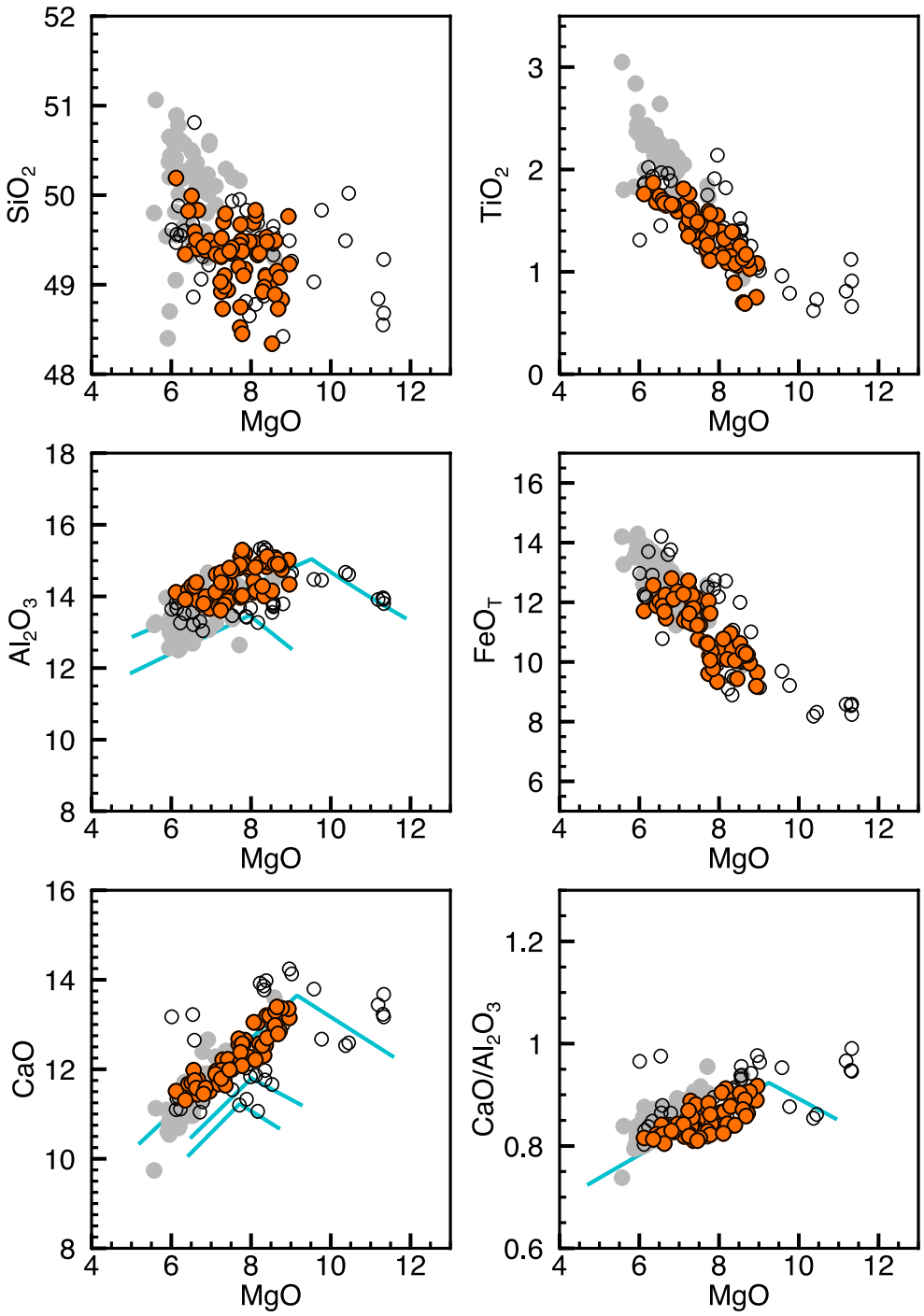

Figure 2.5: Major oxide variation diagrams for the Hartley et al. (2018) Holuhraun MI data, showing filtration by the KB method. Open circles are raw data. Orange filled circles are samples remaining after filtration. All axes are in wt.%. Blue lines are possible liquid lines of descent, which describe the approximate crystallization trend of these samples.

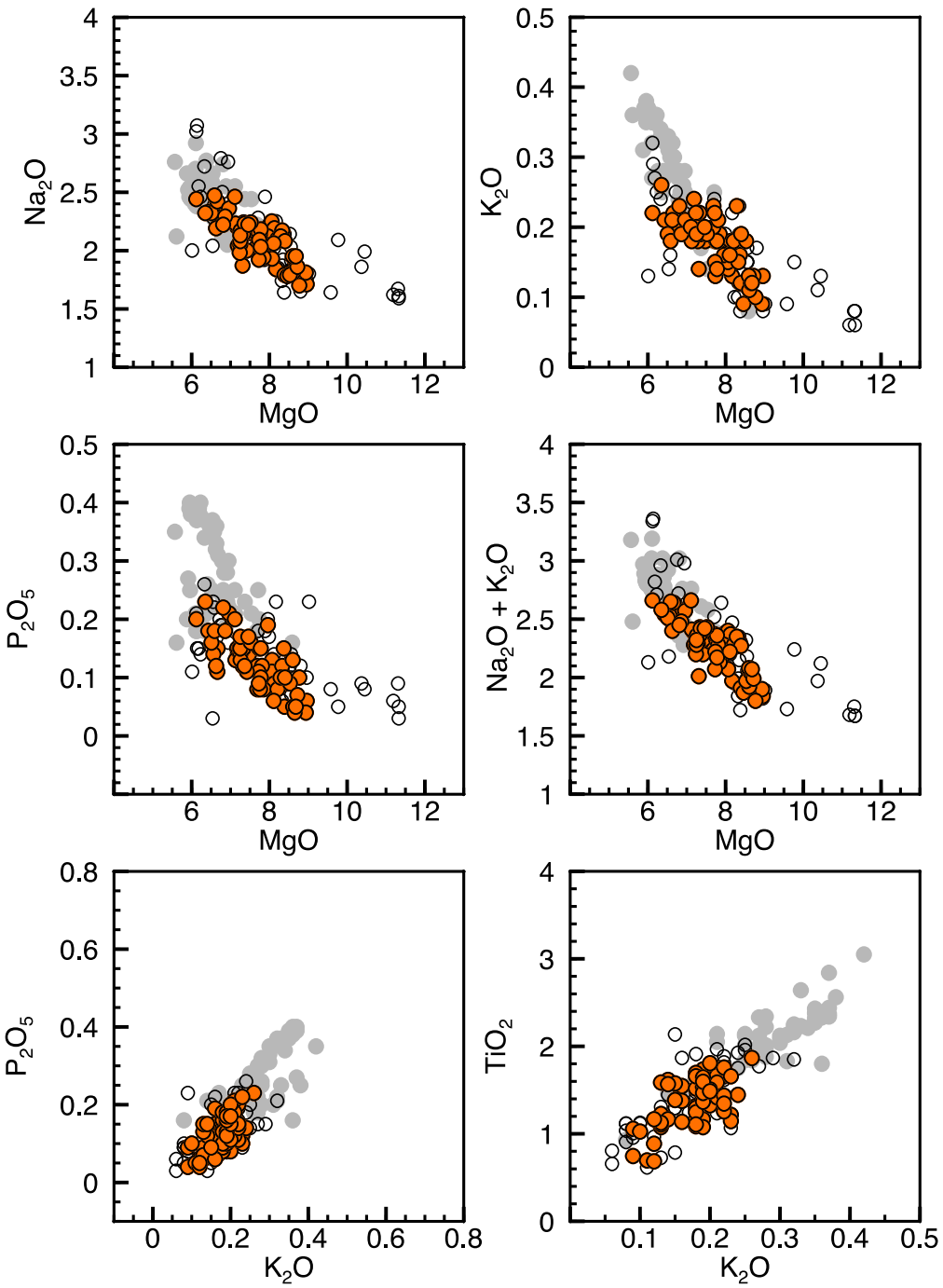

Figure 2.6: Incompatible and alkali oxide variation diagrams for the Hartley et al. (2018) Holuhraun MI data, showing filtration by the KB method. Open circles are raw data. Orange filled circles are samples remaining after filtration. All axes are in wt.%.

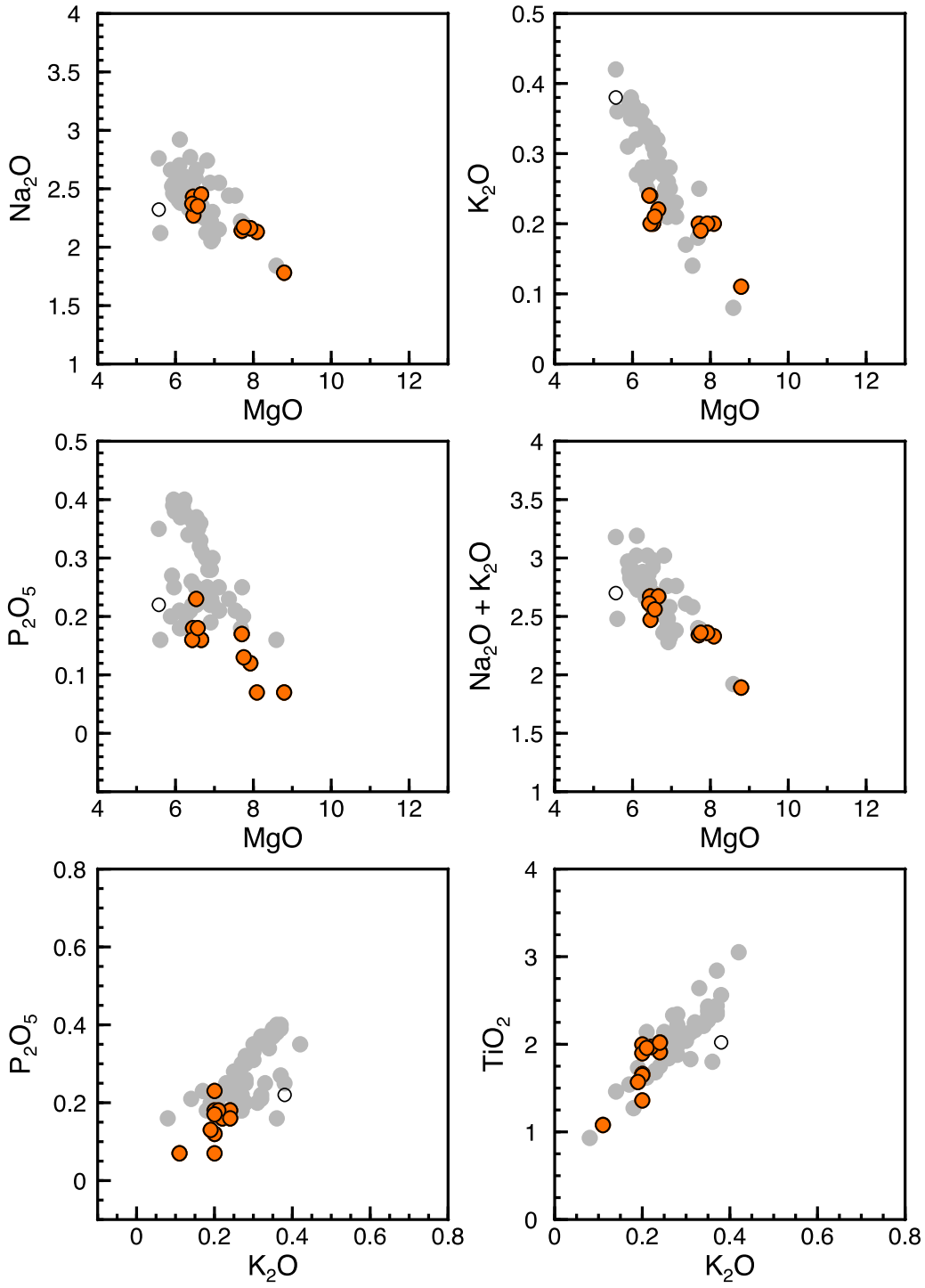

Figure 2.7: Major oxide variation diagrams for the Hartley et al. (2018) Holuhraun groundmass and embayment glass data, showing filtration by the KB method. Open circles are raw data. Orange filled circles are samples remaining after KB filtration. All axes are in wt.%.

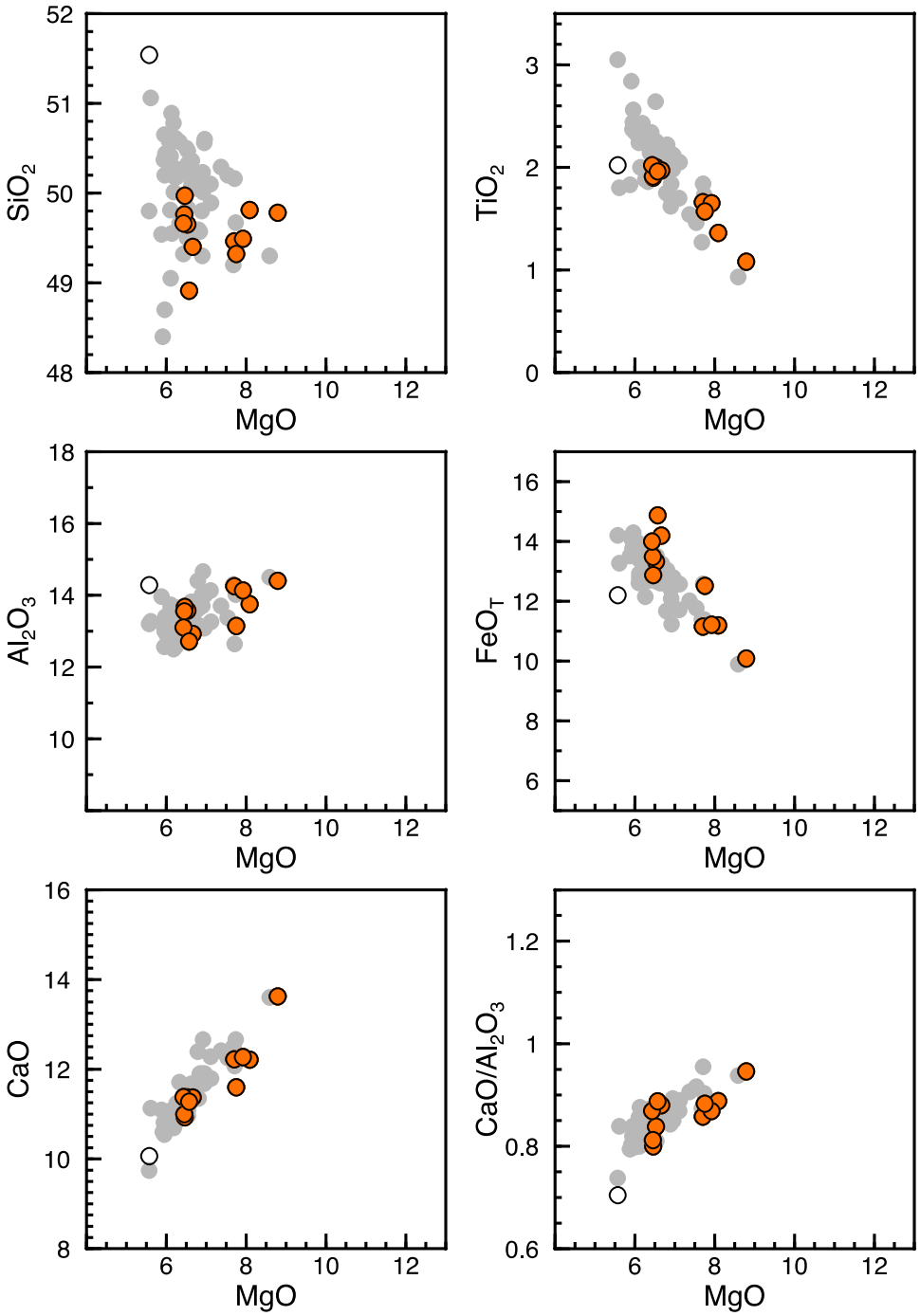

Figure 2.8: Incompatible and alkali oxide variation diagrams for the Hartley et al. (2018) Holuhraun groundmass and embayment glass data, showing filtration by the KB method. Open circles are raw data. Orange filled circles are samples remaining after KB filtration. All axes are in wt.%.

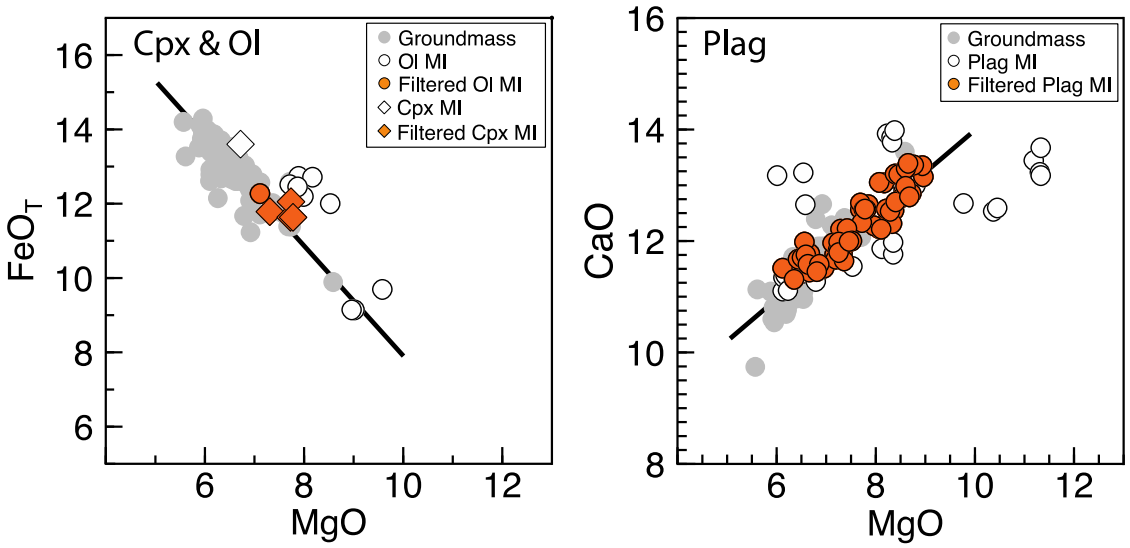

Figure 2.9: Key variation diagrams for olivine and clinopyroxene (left), and plagioclase (right) hosted melt inclusions compared to compiled groundmass glasses. Black line indicates the liquid-line of descent. Open shapes are the unfiltered samples; orange fill indicates samples remaining after filtration. All axes are in wt.%.

Chapter 3. Magma Storage along the Juan de Fuca Ridge

3.1 Geologic Background

The Juan de Fuca Ridge (JdFR) is a mid-ocean ridge (MOR) located in the NE Pacific and separates the Pacific Plate from the Juan de Fuca Plate. It is a remnant of the Pacific-Farallon Ridge following the breakup of the Farallon plate ~30 Ma (Wilson, 1988). The ridge is terminated to the south at 44.5 °N by the Blanco Fracture Zone and extends north for 490 km to a triple junction with the Sovance Fracture Zone and the Nootka fault off the coast of Vancouver Island at 48.78 °N (Wanless et al., 2010).

Previous studies have divided the ridge into seven segments based on first-order segmentation features or large offsets on the ridge (Figure 3.1). These are, from south to north, the Cleft, Vance, Axial, Coaxial, Northern Symmetric (or Cobb), Endeavor, and West Valley segments (Hooft & Detrick, 1995; Arnulf et al., 2018). The northwest-southwest trending Cobb-Eickelberg and Heckle seamount chains intersect the ridge on the Axial and the Endeavour segments, respectively. The Axial Seamount is the youngest seamount of the Cobb-Eickelberg seamount chain and represents a bathymetric high of ~1500 m depth on the JdFR (Arnulf et al., 2018).

The JdFR represents an intermediate spreading center, with a half spreading rate of ~30 mm/yr (calculated using NUVE-1 Plate Parameters described by Argus and Gordon, 1991). The spreading direction is asymmetrical along the Cleft, Coaxial, Endeavor, and West Valley segments, and symmetrical along the Vance and Cobb segments.

The elevation of the seafloor along the ridge is constant, varying from 2344 m below sea level (b.s.l) in the south to approximately 2500 m b.s.l. in the north. However, there is a topographic high at the Axial Volcano (or Axial Seamount), which lies about 1700 m b.s.l..

In addition, the morphology of the ridge axis varies between segments (Figure 3.1a). The ridge axis at the Cleft segment is a broad axial high with 2–3 km wide axial rift. The Vance segment has an 8 km wide axial valley with an axial volcanic ridge within the valley. The Cobb segment is similar to the Cleft segment, but with an axial rift that is deeper and narrower (1–2 km wide). In contrast, the Endeavour segment has a heavily faulted 2-3 km wide axial trough. The most recent volcanic activity on the JdFR occurred in the Cleft segment, whereas the oldest activity occurred in the Endeavor and West Valley segments (Clague et al., 2014).

Seismic studies (e.g. West et al., 2003; Canales et al., 2006; Carbotte et al., 2008; Soule et al., 2016) indicate that the crustal thickness along the JdFR varies from 7.65 km to 7.0 km from the Blanco Fracture Zone to the Axial Volcano. The crust thickens below the Axial Volcano to 11 km and thins to 6.5 km beneath the Coaxial segment. It returns to a thickness of ~7 km in the Endeavour and West Valley segments.

Evidence of Magma Plumbing Systems

A number of seismic studies have imaged magma lenses 1.5 to 3.5 km below the seafloor (b.s.f) along the JdFR (Figure 3.2; Nedimovic et al., 2005; Canales et al., 2005; Baker, 2009; Carbotte et al., 2008; Carbotte et al., 2012) and these shallow magma lenses appear to provide the heat source for the numerous high-flux hydrothermal vents found

along the ridge (Baker, 2009). In addition, Canales et al. (2009) have reported the presence of a sill in the lower crust (5–6 km b.s.f) 1.4–3.2 km from the Cleft Segment spreading axis.

Previous studies using major element geobarometry have found evidence for both shallow and deep partial crystallization at the JdFR (e.g. Herzberg 2004; Wanless & Shaw, 2012; Wanless & Behn, 2017). The shallow depths of partial crystallization agree with seismically imaged melt lenses, whereas the greatest depths do not.

Wanless and Behn (2017), using the Herzberg (2004) geobarometer, find an average pressure of 197 MPa (~7 km b.s.f) for the entire ridge prior to removal of samples that have not crystallized pyroxene (the parameters for which are determined by a linear equation defining excess CaO), and 264 MPa (~9 km b.s.f) after removal of these samples. These pressures have a range of 0–800 MPa (0–28 km b.s.f) in the filtered dataset, with much of the data having pressures less than 500 MPa (~18 km b.s.f). Petrologic modeling also gives similar pressures results (Wanless & Behn, 2017).

In addition, Wanless and Behn (2017) and Wanless and Shaw (2012) use vapor saturation pressures (VSPs) to further constrain depths of crystallization. Results from melt inclusion VSPs have a range of 70 to 100 MPa (~2.5–3.5 km b.s.f), and basaltic glass VSPs show a similar range (50–80 MPa, ~2–3 km b.s.f) for a compilation data from fast and intermediate spreading ridges that includes the JdFR. Wanless and Shaw (2012) find that 51% of the samples from the Cleft and Vance segments of the JdFR agree within 1 km of seismic data, but they suggest extensive deep crystallization due to 25% of samples indicating crystallization at 4.0–5.5 km depth b.s.f, which seismic evidence does not support.

Hotspot Influence

Previous workers have suggested that the Juan de Fuca Ridge is influenced by one or more hotspots to explain the increased crustal thickness and seamount chains along the ridge (e.g. West et al., 2003, Chadwick et al., 2005). These seamount chains are thought to originate from thermally buoyant, but chemically indistinct, mantle plumes. The strongest lines of evidence for the plume hypothesis are an apparent decrease in the age of the lava erupted on the seamounts as the ridge is approached, and seismic evidence of a "whole" mantle plume interacting with the ridge (Desonie & Duncan, 1990; Rhodes et al., 1990; Zhao, 2007). However, geochemical data from the Axial Volcano do not support the presence of a mantle plume along the JdFR. In particular, seamount lavas do not show anomalous isotopic ratios or enrichment in highly incompatible elements, as would be expected in a region influenced by a mantle plume (Rhodes, 1990; Hooft & Detrick, 1995). Therefore, for the purposes of this study, the Juan de Fuca Ridge can be considered a ridge without the influence of a mantle plume.

3.2 Methods

The method described by Kelley and Barton (2008) (KB method) is used to calculate pressures of partial crystallization for the magmas for the JdFR. This method relies on the change in the position of the olivine (*ol*), plagioclase (*plag*), and clinopyroxene (*cpx*) cotectic with changes in pressure, as discussed by Yang et al. (1996). The steps of secondary data processing are outlined here in the order described in Chapter 2.

Data

Samples of fresh basaltic glasses from the Juan de Fuca Ridge (n=1246) were downloaded from the PetDb.org database on the 29th of September 2009. The descriptive parameters and sources of analyses are reported in Appendix C. Data from additional studies were then combined with this download (Stakes et al., 2006; Gale et al., 2013; Clague et al., 2018; Scott et al., 2018).

Data Processing

The steps of secondary data processing for these data are outlined below:

Prior to Pressure Calculation:

1. Samples were removed due to being whole-rock analyses (n=143), and for being incomplete (n=194) with the exception of analyses lacking P_2O_5. The effects of P_2O_5 on calculated pressures are addressed in the discussion section. An additional 66 samples were removed for being duplicate analyses. The data were then plotted by latitude and longitude, and samples off the ridge axis were removed (n=203). This resulted in 640 remaining samples.

   Data were then complied from additional sources not included in the PetDb.org download. The sources of these data are: Stakes et al. (2006) (n=200, after removal of n=14 for lying off the ridge axis), Gale et al. (2013) (n=409), Clague et al. (2018) (n=316), and Scott et al. (2018) (n=36). The final dataset consists of 1601 glass samples.
2. All Fe_2O_3 was then converted to FeO_{Total} to maintain consistency with experimental glass composition data.

3. The data were subdivided into 41 sub-segments based on proximity along the strike of the ridge (Figure 3.1b). This allows for analysis of chemical trends at the scale of individual magma plumbing systems, which is important to understand chemical variations, and thus differences in calculated pressures, along the ridge. As discussed in Chapter 2, because the extent of the 2015 Axial Volcano lava flows described by Clague et al. (2014) was approximately 1° latitude, or ~100 km, this length may be an appropriate as a maximum sub-segment length. Therefore, we have chosen segment lengths of ~0.25° to 0.5° latitude.

After Pressure Calculation:

4. Pressure results were then corrected to account for the weight of the overlying water column. This was done using the reported elevation of the sample, or through extrapolation when data were not available.
5. Samples showing pressures with high error (n=1) were removed.
6. Samples with negative pressures that are not within error of the crust (n=17) were removed. Negative pressures between -0.1 and -126 MPa (n=68) were then normalized to 0.1 MPa to reflect crystallization at the seafloor.
7. Finally, variation diagrams are used for final filtration of the results. In this process, n=826 samples are removed for not being multiply saturated with respect to *ol*, *plag*, and *cpx*. This is described in detail in the discussion section.

3.3 KB Method Unfiltered Results

The average pressure of the unfiltered dataset is 203.8 ± 163.9 MPa with a minimum of -254.5 ± 35.2 MPa and a maximum of 1599.8 ± 55.7 MPa (Table 3.1). The calculated pressures show a general decrease with increasing latitude, with the highest average pressures near the southern tip of the JdFR and the lowest average pressures in in the northern section of the ridge (Figure 3.3). The sub-segment with the highest average pressure (Sub-segment 14, 607.2 MPa) is located at 45.44 °N in the Vance segment, whereas the sub-segment with the lowest average pressure (Sub-segment 26, -83.8 MPa) is near 47.87 °N in the Endeavor segment.

3.4 Discussion

Filtration

Filtration resulted in the complete removal of 11 sub-segments. The average pressure of the filtered dataset is 153.5 ± 85.2 MPa. The filtered dataset consists of 776 samples in 26 sub-segments (Table 3.2). Sub-segment 5b, located in the Cleft segment, has the largest range of pressures (395.9 ± 59.8 to 0.1 ± 28.8 MPa), and sub-segment 3b, also located in the Cleft segment, has the highest average pressure (247.5 ± 73.5 MPa). Sub-segment 15, located in the Axial segment, has the second highest average pressure (205.3 ± 30.7 MPa).

Cotectic filtration is demonstrated in the following examples:

Ex 1: The first example of filtration is from sub-segment 3a (Cleft segment) (Figures 3.4 & 3.5). The highest MgO sample is before an inflection for FeO_T, Al_2O_3, and CaO, and therefore does not lie on the *liq-ol-cpx-plag* cotectic. The four samples

with MgO < 5.5 wt.% clearly lie after an inflection in FeO_T and TiO_2, and have high SiO_2, and anomalous Al_2O_3 and incompatible elements (Figure 3.5). An additional sample (MgO = 5.73 wt.%) also has high FeO_T and TiO_2, and should also be excluded from the final dataset. The elevated incompatible elements in these samples may be an indication of crustal interaction.

This process removes a total of six samples, many of these having low pressures. Therefore, the effect of filtration for this sub-segment is an increase in average pressure from 185.6 ± 68.9 MPa to 198.3 ± 58.5 MPa. The maximum pressure (334.2 ± 41.8 MPa) remains unchanged, whereas the minimum pressure increases from 29.5 ± 61.6 MPa to 82.3 ± 8.0 MPa.

This example demonstrates that filtration does not always substantially change the interpretation of the pressure results. However, filtration is important for optimizing geobarometric results, as the pressures of partial crystallization for off-cotectic samples are outside of the calibration of the method and therefore cannot be interpreted with confidence. In addition, because of the large differences between the unfiltered and filtered dataset for the entire ridge, it is clear that filtration can have a large effect on the interpretation of pressure results. The next example illustrates this.

Ex 2: The second example of filtration is shown for sub-segment 14 (Figure 3.6). This sub-segment contains 4 samples with calculated pressures >1200 MPa (or ~44 km), which are indicated by hatched circles, and 6 samples with pressures <250 MPa, which are indicated by grey circles. The four high-pressure samples are

located before inflections in Al_2O_3, FeO_T, and CaO plots, indicating that they are not crystallizing *cpx*, and should be removed.

Justification for removing the remaining six samples from sub-segment 14 is more subtle. The remaining 6 samples appear to be on the *liq-ol-cpx-plag* based on the MgO vs. Al_2O_3, FeO_T, and CaO trends. However, their trend on the MgO vs. CaO/Al_2O_3 plot is suspect. To examine this, a one-degree polynomial can be fit to this plot (Figure 3.6). The fit has a negative slope, indicating that the CaO/Al_2O_3 of this sub-segment is increasing with decreasing MgO. This shows that Al_2O_3 is being removed from the melt at a faster rate than CaO, which is consistent with the crystallization of *plag*, but not *cpx*. Therefore, none of the ten samples from sub-segment 14 lie on the *liq-ol-cpx-plag* cotectic and the entire sub-segment can be removed from the dataset.

The removal of these samples has the effect of reducing the maximum pressure for the entire dataset to 986.5 ± 0.2 MPa prior to any additional filtration.

This example illustrates two important points. First, it shows that the most useful interpretation of our results is on a local scale, and that detail is lost when looking at only whole-ridge trends. If these data had instead been filtered based on the apparent inflection of the entire dataset (near MgO = 7.5), the six additional samples would not have been filtered out. Second, it demonstrates that secondary processing of results can substantially change their interpretation, as

proper filtration of this segment significantly reduces the maximum pressure along the entire ridge.

Comparison of Filtered and Unfiltered Results

The unfiltered results using the KB method show large pressure ranges along the JdFR. The minimum pressure of -254.5 ± 35.2 MPa is not within 1σ error of the KB method (126 MPa), and so this sample is giving an erroneous pressure above the surface of the seafloor. The maximum pressure (1599.8 ± 55.7 MPa) corresponds to a depth of ~56 km, assuming a crustal density of 2.9 g/cm^3. This depth is unrealistic given the expected crustal thickness of 6.5–11 km along the JdFR, as determined by seismic data (West et al., 2003; Canales et al., 2006; Carbotte et al., 2008; Soule et al., 2016). The filtered data have a smaller range (Max: 466.2 ± 22.8 MPa, Min: 0.1 ± 22.3 MPa, Average: 153.5 ± 85.2 MPa), which corresponds to depths of 0–16 km. Thus, the filtered data better agree with seismic data.

The trend of decreasing pressures from the south to north along the ridge is still apparent in the filtered dataset (Figure 3.7), but the average and maximum pressures of the filtered dataset are lower than those of the unfiltered dataset.

Mantle vs. Crustal Crystallization

The range of pressures calculated in this study is generally within error of the crust and Moho after filtration (Figure 3.8), with the depth of the Moho from Hooft and Detrick (1995) and Carbotte et al. (2008). This suggests that the majority of *liq-ol-cpx-plag* cotectic

crystallization is occurring within the crust beneath the JdFR and not in the mantle, as previous studies have suggested (e.g. Herzberg, 2004; Villiger et al., 2007; Wanless & Shaw, 2012; Wanless & Behn, 2017).

Interpretation of Calculated Pressures

For the interpretation of the pressure results, we present histograms for the Cleft, Axial, and Endeavor segments. Figure 3.9 shows that the pressures for the Cleft and Axial segments are approximately normally distributed, with averages of ~200 MPa (corresponding to a depth of 7 km), whereas the pressures for the Endeavor segment are densely clustered at low pressures.

It is important to note that average pressures may not always indicate a true clustering of pressure values and may rather describe the pressure at which the range of pressures for sub-segment is centered. If the average pressure corresponds to the most frequent pressure value for a given location, it may indicate the depth where magma tends to pond. In contrast, where a uniform distribution of pressure is observed, crystallization may occur within multiple lenses at various depths, in a crystal mush, or mixing may be a factor.

This can be seen in Figure 3.10, where histograms for three selected sub-segments in the Cleft segment are shown. While the histogram for the entire Cleft segment shows an approximately normal distribution, Figure 3.10, indicates that sub-segments 3a and 5a are roughly uniformly distributed such that the average represents where the pressure range of the sub-segment is centered, and not the pressure that is observed most frequently. Conversely, for sub-segment 5b, the average pressure indicates a clustering of pressure

values. However, sub-segment 5b has a larger sample size, which may contribute to its approximate normal distribution.

For the Axial segment, histograms for three selected sub-segments (Figure 3.11) show that the pressures are clustered around the means at each location. Because sub-segments 15 and 19a have relatively small sample sizes, the approximate normal distribution of the results is not due to a statistical artifact. This indicates that *liq-ol-cpx-plag* cotectic crystallization occurs around 200 MPa (~7 km) along the Axial segment.

For the Endeavor segment (Figure 3.12), the sub-segments have a dense clustering of pressure values at low pressures. Sub-segment 27 exhibits the largest range, with some high-pressure values (maximum 196 MPa, 6.9 km). However, the majority of *liq-ol-cpx-plag* cotectic crystallization in the Endeavor segment is at shallow depths.

Agreement with Seismic Data

The pressure ranges found in this study generally agree with the depths at which melt lenses have been imaged by seismic data. However, the average pressures found in this study correspond to greater depths than seismically imaged melt lenses for the Cleft and Axial segments, and to shallower depths for the Endeavor segment.

The pressure results indicate that the bulk of *liq-ol-cpx-plag* cotectic crystallization is occurring near ~6 km beneath much of the Cleft segment, whereas published seismic studies have found melt lenses near 2 km depth (Canales et al., 2005; Carbotte et al., 2006). Our results support only minor *liq-ol-cpx-plag* cotectic crystallization near 2 km depth (Figure 3.10). It is notable that an off-axis sill has been imaged in the lower crust 5–6 km below the seafloor, which does agree with our average pressures (Canales et al., 2009). Despite this sill

being found off the spreading axis, it can be assumed it originated under the axis. Therefore, this segment may have at least two regions of melt ponding, with seismic studies only locating the shallowest lenses.

The average pressure for the Axial segment also corresponds to greater depths than seismically imaged melt lenses at ~1.5 km depth (Arnulf et al., 2018), and there are few calculated pressures <75 MPa (2.6 km depth). However, the pressures in this study are generally within error of the low-velocity zone from 2.25 to 6 km depth described by West et al. (2001).

The average pressures for the Endeavor segment correspond to shallower depths (38.8 MPa, <1.5 km) than melt lenses imaged at ~2.8–3.3 km depth (Van Ark et al., 2007; Carbotte et al., 2012; Clague et al., 2014). However, the seismically imaged melt lenses are within range of the calculated pressures (maximum: 195.9 MPa, 6.9 km; minimum: 0.1 MPa, 0 km). The low pressures calculated for the Endeavor segment may be explained by crustal interaction, as shown in Figure 3.13. The Endeavor segment data lack defined trends in K_2O, P_2O_5, and Na_2O, which may suggest widespread crustal interaction. In addition, the trend of K_2O vs. P_2O_5 deviates from a 1:1 relationship. A 1:1 relationship between these two oxides would be expected, as both K_2O and P_2O_5 are similarly incompatible. Thus, this evidence of crustal interaction makes these pressures suspect, and thus strong conclusions cannot be drawn from these data.

Seismically imaged melt lenses along the JdFR tend to be located in the shallow crust, whereas KB pressures suggest that *liq-ol-cpx-plag* cotectic crystallization may be polybaric. Disagreement between pressures calculated in this study and published seismically imaged melt lenses suggests that the bulk of cotectic *liq-ol-cpx-plag* crystallization does not

occur in discrete lenses, but rather in a dispersed crystal mush or in dikes. This also suggests that many melt lenses are short-lived. Other researchers have proposed the existence of short-lived melt lenses (e.g. Pan & Batiza, 2002, who calculated short residence times of 30–90 days for magma in lenses along the East Pacific Rise). Evidence for short melt lenses is discussed below in the *Locating Melt Lenses* section. This highlights an important point: seismic methods are able to constrain the depth of melt lenses at the time of study, whereas petrologic geobarometers give insight into past melt lens depths. Therefore, the depths of magma storage as determined by seismic and geobarometric methods may differ.

Agreement with Previous Geobarometric Studies

The average pressure from this study for the filtered dataset of the entire ridge (153.5 ± 85.2 MPa) is lower than the average pressure (264 MPa) reported by Wanless and Behn (2017) using the Herzberg (2004) method. The range of pressures from this study (0.1–466 MPa, 0–16 km b.s.f.) also disagrees with the range of pressures (0–800 MPa, 0–28 km b.s.f.) from Wanless and Behn (2017). However, Wanless and Behn (2017) report that the Herzberg (2004) filtration method does not effectively remove all samples that do not lie on the *liq-ol-cpx-plag* cotectic, and therefore their pressure results may not be reliable.

The VSPs reported by Wanless and Shaw (2012) and Wanless and Behn (2017), in contrast, are in better agreement with the pressure results from this study. These workers report MI VSPs of 70–100 MPa (2.5–3.5 km b.s.f) and basaltic glass VSPs for 50–80 MPa (2–3 km b.s.f.) for a compilation of multiple intermediate spreading ridges. They cite that 25% of these samples indicate crystallization at 4.0–5.5 km depth. The KB method results for the JdFR generally agree with these findings.

Crustal Thickness

The high pressures near the Blanco Fracture Zone may indicate that the crust is thicker in this region. Previous workers have observed that the crust near transform boundaries is thinner and colder than the crust along the ridge axis (Cormier et al., 1984, Ghose et al., 1996; Langmuir & Forsyth, 2007). However, Gregg et al. (2007) find gravity anomaly evidence for possible crustal thickening at transform faults, and Herzberg (2004) also note higher pressures of partial crystallization near transform faults along the Mid-Atlantic Ridge and the East Pacific Rise. The data from the Blanco Fracture Zone of the JdFR agree with these findings, which suggests that crustal thickness at MOR transform faults is complex and dependent on many factors.

The high pressures near the Axial Seamount also suggest thickened crust, which agrees with seismic studies performed on this region (Arnulf et al., 2018; West et al., 2003). Sub-segment 17 in the Axial segment shows a large range in pressures, with the minimum and maximum corresponding depths of ~0.0 km to 10.5 km, respectively. Similarly, sub-segment 19a, at the northern end of the Axial segment, has minimum and maximum pressures corresponding depths of ~3.8 km to 10.6 km. This agrees with the 11 km thick crustal root beneath the Axial Volcano imaged seismically by West et al. (2003).

Locating Melt Lenses

After filtration, multiple sub-segments have pressure ranges within 1σ error of the method (126 MPa). These narrow pressure ranges indicate the depths at which melts typically pond in the crust due to density and buoyancy effects. Sub-segments 15 (Axial

segment), 20 (Coaxial segment), and 25 and 26 (Endeavor segment) have the largest number of samples with a restricted range and are plotted in Figure 3.14.

Sub-segment 15 shows a narrow range of wt. % MgO (0.98 wt. %), indicating that these melts have undergone only a small degree of fractionation. This suggests the presence of a short-lived melt lens in the lower crust (4.9–8.5 km b.s.f) at the Axial segment. The location of the sub-segment 15 melt lens is within error of the seismically imaged ~11 km thick crustal root (West et al., 2003) at the Axial Volcano, but at greater depths than melt lenses found at ~1.5 km depth in seismic surveys (Arnulf et al., 2018).

The large range of wt. % MgO (~2 wt. %) for sub-segments 20, 25, and 26 may indicate that melts with varying degrees of fractionation commonly pond at middle to upper-crustal depths (0.8–5.2 km b.s.f.), or may indicate the presence of long-lived melt lenses.

Gale Correction vs. Non-correction

Because this geobarometer is sensitive to minor changes in major element compositions, another important consideration for the interpretation of the results is the effect of interlaboratory biases for analyses. Gale et al. (2013) have published correction factors for interlaboratory biases for global MOR data. These biases affect a considerable number of samples (n=750). We have chosen to use the original, uncorrected data for this study, and we address the effects of this on the calculated pressures here.

The average change in pressure for the uncorrected and corrected data is 47 ± 26 MPa, with a maximum change of +75 MPa and a minimum change -8 MPa. The largest differences in calculated pressures arise from data from the EMP at the Smithsonian Institution of Washington (Gale Correction Method 3). The correction for the EMP at the

University of British Columbia (Gale Correction Method 22) resulted in a minor change in pressures (±8 MPa), and the correction for the EMP at the Lamont-Doherty Earth Observatory of Columbia University (Gale Correction Method 4) resulted in no pressure change. Pressure changes these correction methods are within the error of the KB geobarometer (126 MPa) and therefore are not significant for the purposes of this study.

Modeling of LLDs and Water Variation Along the Ridge

Modeling of LLDs can be used to check the veracity of the calculated pressures of partial crystallization and constrain the water content of samples.

For the Cleft segment and the Blanco Fracture Zone, modeled LLDs generally corroborate the range of calculated pressures for the unfiltered data. The modeled LLDs for this segment constrain the average pressure of partial crystallization to ~180 MPa under anhydrous conditions and ~100 MPa with up to 0.1 wt.% of water (Figures 3.15 and 3.16). The hydrous LLDs fit the crystallization trends observed for this section of the ridge, however, the anhydrous model most closely reflects the average pressure of ~190 MPa calculated for the filtered dataset in this region.

For the Axial segment, the modeled anhydrous LLDs do not provide a good fit for the unfiltered data (Figure 3.17). This indicates that these magmas are likely hydrous. The models with at least 0.1 wt. % water are the best fit for this segment (Figure 3.18). This constrains the average pressure of partial crystallization to 100–200 MPa, which agrees with the average pressure of ~170 MPa for the filtered dataset for this segment.

The Endeavor segment data also do not agree with the anhydrous LLDs (Figure 3.19). The scatter in the variation diagrams can be correlated with water between 0.1 and 0.3

wt. % (Figures 3.20 and 3.21). The modeled LLDs using 0.1 wt. % water best fit the average calculated pressure for the filtered dataset for this segment (~200 MPa).

To further investigate the water content of these melts, wt.% water data for JdFR basalts was compiled from PetDb.org (download parameters are given in Appendix E), and normalized to $water_{8.0}$ using a method similar to that described by Klein & Langmuir (1987) and Langmuir et al. (1992) for Na and Fe (details in Appendix D). This allows for a meaningful comparison of water content at different degrees of fractionation.

Prior to $water_{8.0}$ normalization, the highest wt.% water is south of 45°N latitude (Cleft segment) and at 48°N latitude (Endeavor segment) (Figure 3.22). There is an apparent increase in wt.% water between 46°N and 48°N (from the Axial segment to the Endeavor segment).

$Water_{8.0}$ reduces the water content of most samples, however, the data include incomplete analyses, and thus $water_{8.0}$ cannot be calculated for all samples. Therefore, the high wt.% water samples at 48°N latitude cannot be normalized. The available results suggest that melts at the Cleft segment may be more hydrous than the rest of the ridge and that there may be an increase in magma water content (0.15 to 0.4 wt. %) from south to north between the Axial and Endeavor segments. This disagrees with modeling results for the Cleft segment, which indicate that the Cleft segment is anhydrous. This could be due to an error in the modeling, however more water data is necessary to assess this. The $water_{8.0}$ normalization agrees with modeling in the Axial segment (suggesting >0.1 wt. % water), and data is insufficient to make strong conclusions for the Endeavor segment.

Effects of P_2O_5 on Calculated Pressures

The KB method is also sensitive to wt.% P_2O_5 due to the crystallization of apatite in pressure calculations, where apatite reduces Ca in the melt. This can be problematic as P_2O_5 is in low abundance in MOR basalts, and is often not included as part of major element analyses. If wt.% P_2O_5 is null during the calculation of normative mineral compositions, crystallization of apatite will not be accounted for. This results in a higher wt. % CaO and erroneously low pressures. We address this by modeling P_2O_5 values along the ridge.

In the unfiltered dataset, 89 samples lack P_2O_5 measurements. The expected P_2O_5 can be modeled by fitting a power curve to the observed P_2O_5 for the unfiltered dataset. The equation for this fit is:

$$Model\ P_2O_5 = 16.10 \pm 0.21 \times MgO^{-2.37 \pm 0.11}$$

This model has $R^2 = 0.552$. Figure 3.23 shows that this model provides a good fit for most samples with MgO > 4 wt.%.

This model has been applied to the entire unfiltered dataset in order to quantify its effect on calculated pressures (Figure 3.24). For this comparison, samples with MgO < 4 wt.% (n=10) are excluded due to poor model performance. The average pressure of the unfiltered dataset using modeled P_2O_5 is identical to that using observed P_2O_5 (202.3 ± 165.4 MPa and 203.8 ± 163.9 MPa, respectively), with maximums and minimums also within error. The average change in calculated pressure is small (0.8 ± 22.7 MPa). The maximum change is by +174.6 MPa, which is slightly outside the error of the method. Therefore, the effect of missing P_2O_5 analyses is not of large concern in the interpretation of these results. This is especially true as only 52 of the 89 samples for which P_2O_5 has not been analyzed persist in the filtered dataset.

Temperature and Depth of Melt Segregation from the Mantle Source

Similar to incompatible elements, eruption temperatures are strongly controlled by the degree of melt fractionation. Therefore, in order to make a meaningful comparison of eruption temperatures of melts at different degrees of fractionation, calculated temperatures were also normalized to 8.0 wt.% MgO after Klein and Langmuir (1987) and Langmuir et al. (1992). The normalized temperatures are reported as $Temp_{8.0}$. Additional information, including the equations used for this normalization, can be found in Appendix D.

Both before and after normalization, there is no apparent change in temperature along the length of the ridge (Figure 3.25). Figure 3.25 shows a slight decrease in temperature from south the north along the ridge post-normalization, however, this change is within the error of the average normalized 1σ error (5±13 °C).

It is widely accepted that Axial Volcano is the result of a positive thermal anomaly in and beneath the crust (e.g. Rhodes et al., 1990; Hooft & Detrick, 1995; West et al., 2003; Carbotte et al., 2008), so it is important to determine whether there are variations in pre-eruptive temperatures along the JdFR. If there were a temperature anomaly under the Axial Volcano, a $Temp_{8.0}$ increase near the Axial Seamount would be expected. The lack of this temperature increase likely indicates that there is no such anomaly.

To confirm the lack of a thermal anomaly near Axial Volcano, $Na_{8.0}$ and $Fe_{8.0}$ were also calculated according to the method described by Klein and Langmuir (1987), Langmuir et al. (1992), and Langmuir and Forsyth (2007), with the equations given in Appendix D. $Na_{8.0}$ and $Fe_{8.0}$ can be used to investigate possible variations in the extent of partial melting and the depth of melt segregation from the mantle source beneath the ridge.

$Na_{8.0}$ provides information about the extent of melting in the mantle beneath the ridge, which serves as a proxy for variations in the thermal state of the mantle and the thickness of the crust, since crustal thickness is directly correlated with the extent of melting (Langmuir et al. 1992; Langmuir & Forsyth, 2007). Therefore, a decrease in $Na_{8.0}$ indicates an increase in the amount of melting in the sub-ridge mantle and an increase in the thickness of oceanic crust.

The interpretation of $Fe_{8.0}$ is more complex and is dependent on the correlation between $Na_{8.0}$ and $Fe_{8.0}$. A positive correlation indicates that the degree of partial melt is responsible for any change in $Fe_{8.0}$, and a negative correlation indicates that a change in the depth of segregation of the melt from the mantle is responsible for changes in $Fe_{8.0}$, with higher $Fe_{8.0}$ values indicating greater depths of segregation. No correlation indicates that the degree of partial melting beneath the ridge is variable, with the melts segregating at similar depths (Klein and Langmuir, 1987).

If a positive thermal anomaly does exist at Axial Volcano, a higher degree of melting, as indicated by a low $Na_{8.0}$ would be expected. However, Figure 3.26 shows that $Na_{8.0}$ remains constant along the strike of the ridge, indicating that the average degree of melting at the Axial Volcano is not higher than that at other segments of the JdFR. $Fe_{8.0}$, however, does decrease from south to north along the ridge, with the lowest values in the Endeavor segment. The correlation between $Na_{8.0}$ and $Fe_{8.0}$ is slightly negative. The negative correlation may indicate that the depth of melt segregation is highest in the southern portion of the ridge and shallower in the northern part of the ridge. Interestingly, the highest pressures of partial crystallization also occur in the southern portion of the ridge, indicating that both melt segregation and partial crystallization occur at depth in the southern portion of the

JdFR. However, the one-degree regression has a poor fit (R^2=0.16), and thus a strong conclusion cannot be drawn.

3.6 Conclusions

The JdFR has been the subject of seismic and geobarometric studies to constrain the crustal structure and melt storage at intermediate spreading ridges. Seismic studies have shown that the average crustal thickness along the JdFR is ~7 km, with an increase to 11 km beneath the Axial Volcano. However, most seismically imaged melt lenses are at relatively shallow depths (1.3 to 3.5 km) (e.g. Nedimovic et al., 2005; Canales et al., 2006; Baker, 2009; Carbotte et al., 2008; Carbotte et al., 2012).

In contrast, previous major element geobarometric studies have suggested that partial crystallization occurs at much greater depths along the JdFR, corresponding to the upper mantle (e.g. Herzberg, 2004; Villiger et al., 2007; Wanless & Shaw, 2012; Wanless & Behn, 2017). If crystallization were occurring at these depths, associated crustal thickening would be expected, which seismic evidence does not support.

This study reevaluates the depths of partial crystallization for the JdFR by filtration of results output by the KB method. In the filtration process, samples that are not consistent with *liq-ol-cpx-plag* cotectic crystallization, as defined by tight arrays on variation diagrams, are removed from the dataset, as these samples give pressure results that are outside the assumptions made for *liq-ol-cpx-plag* cotectic crystallization for which the meaning is not clear. This process significantly changes the interpretation of depths of *liq-ol-cpx-plag* cotectic crystallization along the JdFR.

After using this filtration procedure, pressures of partial crystallization along the JdFR are mostly within error of the Moho, with these pressures generally reflecting the trends of crustal thickening and thinning observed by seismic data. However, these results indicate that a significant amount of *liq-ol-cpx-plag* cotectic crystallization occurs at greater depths than seismically imaged melt lenses for the Cleft and Axial segments. This may support multi-depth (i.e. polybaric) magma storage for much of the JdFR, with only the shallowest magma reservoirs being imaged by seismic studies. For the Endeavor segment, in contrast, pressure results indicate that the majority of *liq-ol-cpx-plag* cotectic crystallization occurs at shallower depths than seismically imaged melt lenses. However, there is evidence of crustal interaction for many samples along this segment, which may affect these pressure results.

This study demonstrates the need for careful filtration of samples in major element geobarometric studies in order to obtain the most reliable estimate of depths of crystallization. After filtration, these results provide the first high-resolution insights into *liq-ol-cpx-plag* cotectic crystallization and magma storage depths along the JdFR.

Juan de Fuca Unfiltered Summary

Sub-segment	#	Lat	Long	P Mpa*	Stdev	Max	Min	Depth km**	Stdev	Max	Min	Elevation km ***	Stdev
1	8	44.44	-130.44	135.52	63.75	200.16	28.31	4.77	2.24	7.04	1.00	2.19	-0.0462
2	13	44.53	-130.44	111.35	136.58	368.08	-190.95	3.92	4.81	12.95	-6.72	2.25	-0.0479
3a	36	44.57	-130.39	185.60	68.86	334.19	29.50	6.53	2.42	11.76	1.04	2.24	-0.034
3b	66	44.60	-130.41	272.39	72.18	467.06	119.89	9.58	2.54	16.43	4.22	1.81	-1.3006
4	11	44.62	-130.40	172.34	64.57	312.26	44.68	6.06	2.27	10.99	1.57	2.23	-0.0311
5a	49	44.64	-130.36	277.11	104.45	493.17	77.20	9.75	3.68	17.35	2.72	2.20	-0.058
5b	246	44.66	-130.34	196.42	71.50	575.70	-19.62	6.91	2.52	20.26	-0.69	2.20	-0.0333
6	19	44.73	-130.35	160.70	57.20	298.21	76.19	5.65	2.01	10.49	2.68	2.36	-0.293
7	50	44.77	-130.32	266.82	224.86	802.10	27.69	9.39	7.91	28.22	0.97	2.21	-0.075
8	6	44.82	-130.31	166.91	43.57	214.81	106.79	5.87	1.53	7.56	3.76	2.29	-0.1407
9	7	44.91	-130.25	152.96	51.67	214.60	97.98	5.38	1.82	7.55	3.45	2.26	-0.0144
10	37	44.98	-130.22	171.23	85.69	460.71	7.89	6.03	3.02	16.21	0.28	2.24	-0.1181
11	6	45.02	-130.19	172.33	158.69	414.06	25.85	6.06	5.58	14.57	0.91	2.27	-0.0162
12	52	45.15	-130.14	198.31	110.99	526.08	43.29	6.98	3.91	18.51	1.52	2.29	-0.2902
13	17	45.25	-130.14	156.45	155.62	607.67	-210.22	5.51	5.48	21.38	-7.40	2.39	-0.0109
14	10	45.44	-130.08	607.22	647.10	1599.78	23.34	21.37	22.77	56.29	0.82	1.80	-0.5874
15	142	45.60	-130.03	298.14	128.15	928.36	-49.87	10.49	4.51	32.67	-1.75	2.21	-0.1987
16	7	45.77	-130.02	53.22	58.11	147.20	-19.47	1.87	2.04	5.18	-0.68	2.17	0
17	314	45.91	-130.00	191.57	86.18	552.31	-211.22	6.74	3.03	19.43	-7.43	1.60	-0.094
18	86	45.99	-130.03	339.22	193.68	929.10	74.60	11.94	6.82	32.69	2.62	1.52	-0.0294
19a	58	46.07	-129.99	215.76	52.98	405.37	106.69	7.59	1.86	14.26	3.75	1.75	-0.2617
19b	4	46.16	-129.81	98.14	17.24	113.32	75.71	3.45	0.61	3.99	2.66	2.07	-0.0271
20	24	46.32	-129.71	198.63	292.96	991.57	28.28	6.99	10.31	34.89	0.99	2.30	-0.1023
21	3	46.48	-129.61	37.75	30.30	72.73	19.58	1.33	1.07	2.56	0.69	2.38	-0.0044
22	42	46.53	-129.57	384.90	244.05	772.37	17.96	13.54	8.59	27.18	0.63	2.44	-0.0456
23	14	46.90	-129.29	210.07	109.28	380.27	40.53	7.39	3.85	13.38	1.43	2.42	-0.0887
24	4	47.22	-129.09	57.68	36.48	99.81	21.52	2.03	1.28	3.51	0.76	2.60	-0.0204
25	33	47.66	-129.24	60.22	145.94	665.20	-97.16	2.12	5.14	23.41	-3.42	2.52	-0.1479
26	18	47.87	-129.18	-83.78	72.87	35.86	-227.62	-2.95	2.56	1.26	-8.01	2.33	-0.1285
27	121	47.96	-129.11	34.24	132.20	530.58	-207.67	1.20	4.65	18.67	-7.31	2.14	-0.1003
28	21	48.02	-129.05	2.18	115.39	214.50	-188.48	0.08	4.06	7.55	-6.63	2.25	-0.1135
29	26	48.17	-129.06	183.14	234.61	668.08	-183.45	6.44	8.26	23.51	-6.45	2.55	-0.1841
30	11	48.29	-129.10	-17.14	185.26	391.40	-254.48	-0.60	6.52	13.77	-8.95	1.72	-0.3024
31	11	48.39	-129.09	278.03	161.30	521.64	71.76	9.78	5.68	18.35	2.53	2.46	-0.2817
32	21	48.50	-128.95	205.41	137.70	353.44	-60.16	7.23	4.85	12.44	-2.12	2.53	-0.2533
33	8	48.88	-128.86	120.72	118.20	212.42	-113.22	4.25	4.16	7.47	-3.98	2.38	0

* Pressure corrected for water column overburden
** Depth below seafloor
*** Elevation of seafloor below sealevel

Table 3.1: Summary table of the unfiltered JdFR dataset.

Juan de Fuca Filtered Summary

Sub-segment	#	Lat	Long	**P Mpa***	Stdev	Max	Min	**Depth km****	Stdev	Max	Min
1	6	44.44	-130.44	**123.82**	69.71	200.16	28.31	**4.36**	2.45	7.04	1.00
2	12	44.53	-130.44	**139.79**	98.52	368.08	0.10	**4.92**	3.47	12.95	0.00
3a	22	44.57	-130.38	**198.34**	58.50	334.19	82.32	**6.98**	2.06	11.76	2.90
3b	23	44.59	-130.40	**247.26**	67.77	466.83	119.89	**8.70**	2.38	16.43	4.22
4	9	44.62	-130.40	**172.58**	71.81	312.26	44.68	**6.07**	2.53	10.99	1.57
5a	21	44.64	-130.37	**183.02**	69.77	311.29	77.20	**6.44**	2.45	10.95	2.72
5b	231	44.66	-130.35	**193.47**	66.42	395.89	0.10	**6.81**	2.34	13.93	0.00
6	19	44.73	-130.35	**160.68**	58.98	298.21	64.87	**5.65**	2.08	10.49	2.28
7	17	44.77	-130.30	**155.33**	89.42	343.00	27.69	**5.47**	3.15	12.07	0.97
9	2	44.89	-130.26	**98.46**	0.67	98.94	97.98	**3.46**	0.02	3.48	3.45
12	4	45.13	-130.12	**106.57**	54.61	185.77	64.87	**3.75**	1.92	6.54	2.28
15	32	45.67	-130.02	**205.30**	30.74	250.16	140.14	**7.22**	1.08	8.80	4.93
16	6	45.77	-130.02	**59.34**	58.20	147.20	0.10	**2.09**	2.05	5.18	0.00
17	150	45.89	-130.00	**161.14**	51.15	298.08	0.10	**5.67**	1.80	10.49	0.00
19a	47	46.08	-129.99	**197.50**	32.04	300.63	106.69	**6.95**	1.13	10.58	3.75
19b	4	46.16	-129.81	**98.14**	17.24	113.32	75.71	**3.45**	0.61	3.99	2.66
20	20	46.31	-129.67	**87.69**	30.44	139.63	28.28	**3.09**	1.07	4.91	0.99
22	16	46.53	-129.58	**127.65**	33.65	159.83	17.96	**4.49**	1.18	5.62	0.63
23	9	46.90	-129.28	**196.71**	102.54	299.17	40.53	**6.92**	3.61	10.53	1.43
25	21	47.67	-129.27	**14.89**	23.58	86.73	0.10	**0.52**	0.83	3.05	0.00
26	14	47.87	-129.19	**4.01**	10.47	35.86	0.10	**0.14**	0.37	1.26	0.00
27	60	47.96	-129.13	**22.82**	44.17	195.92	0.10	**0.80**	1.55	6.89	0.00
28	3	48.02	-129.02	**0.10**	0.00	0.10	0.10	**0.00**	0.00	0.00	0.00
29	10	48.17	-129.00	**38.78**	38.66	105.75	0.10	**1.36**	1.36	3.72	0.00
30	4	48.27	-129.05	**6.22**	12.24	24.59	0.10	**0.22**	0.43	0.87	0.00
32	5	48.47	-129.04	**26.46**	43.01	99.08	0.10	**0.93**	1.51	3.49	0.00

*** the pressure without the pressure due to the water column**
**** Depth below seafloor**
***** Elevation of seafloor below sealevel**

Table 3.2: Summary table of the filtered JdFR dataset.

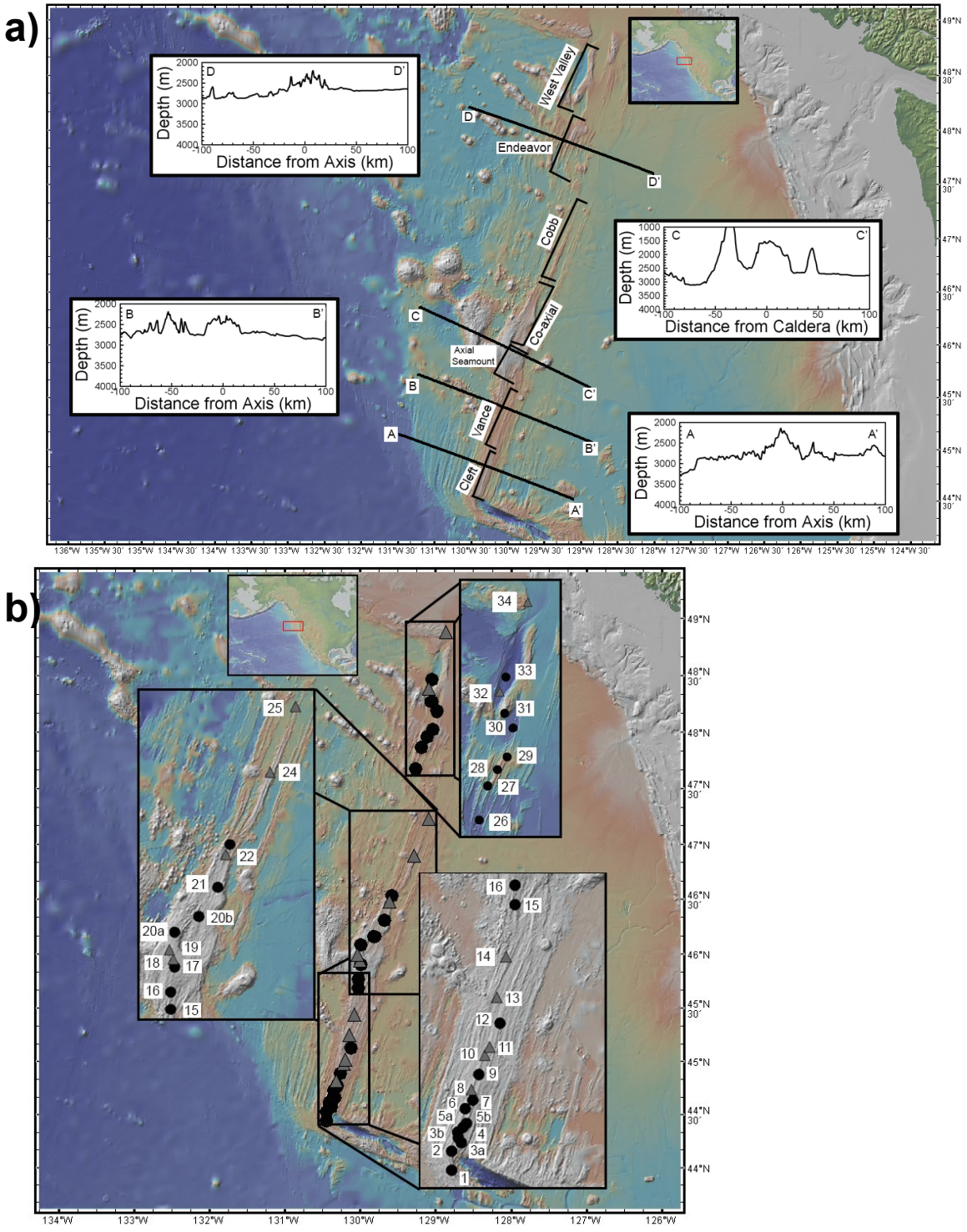

Figure 3.1: JdFR segments and selected transects showing segment morphology (a), and location of sub-segments (b). Imagery and data from GeoMapApp.

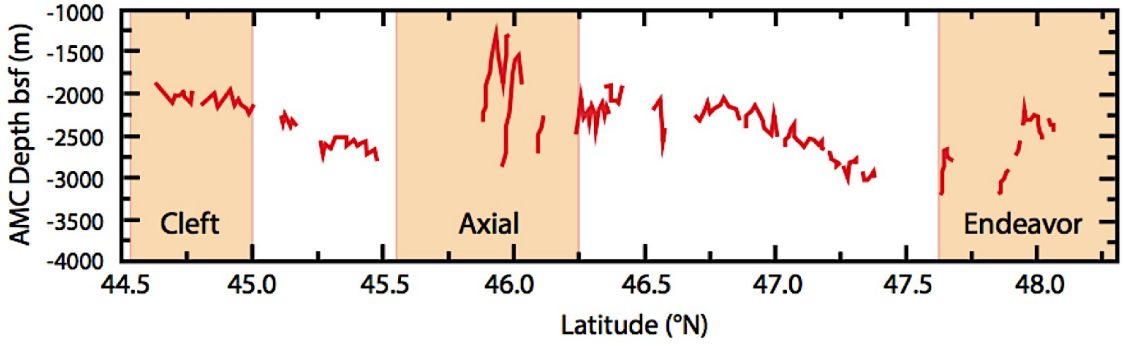

Figure 3.2: Depths of axial magma chamber depths below the seafloor along the JdFR. Modified from Carbotte et al. (2008).

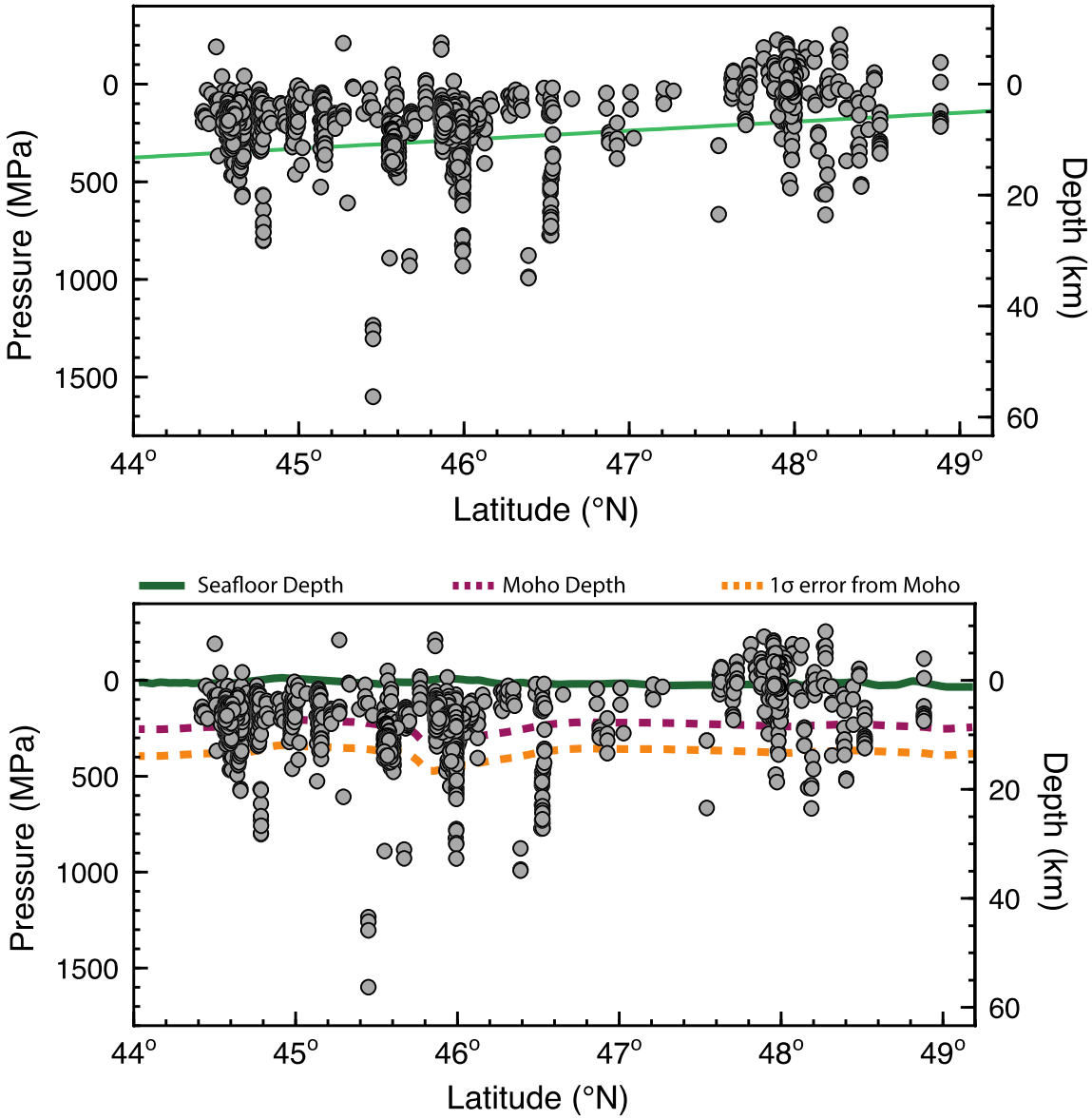

Figure 3.3: **Top**: Unfiltered pressure results along the strike of the JdFR. Pressures are corrected for the overburden of the water column. Green line is a 1-degree polynomial regression, showing a decrease in pressures of partial crystallization from south to north along the ridge. **Bottom**: Unfiltered pressure results along the strike of the JdFR. Green solid line indicates depth of the seafloor. Purple dashed line indicates depth of the Moho. Yellow dashed line indicates 1σ error of the Moho. Depth of the Moho from Hooft and Detrick (1995), Carbotte et al. (2008), after Scott (2017). Depth is calculated assuming a crustal density of 2900 kg/m^3.

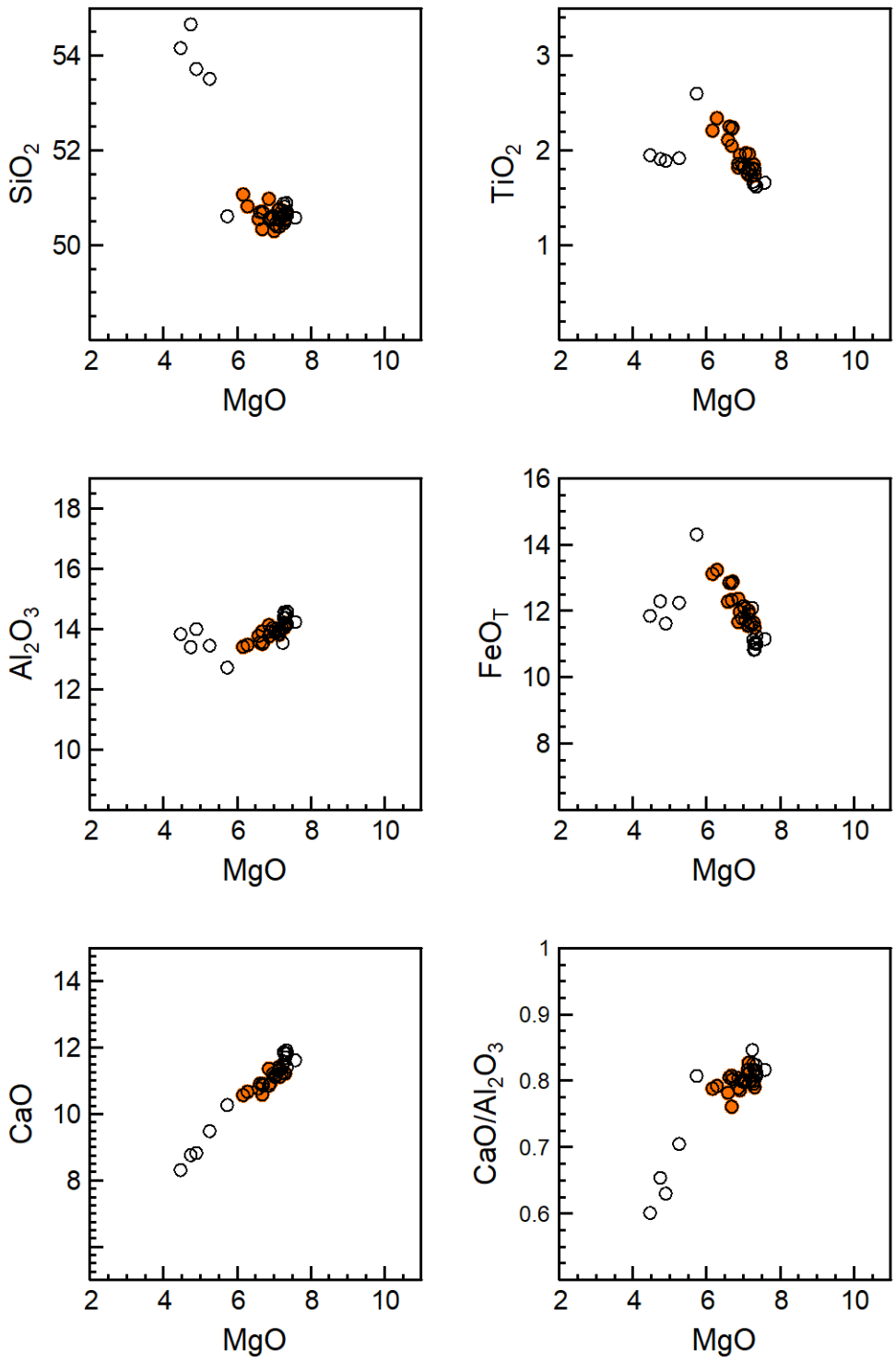

Figure 3.4: Sub-segment 3a filtration example showing major oxides. Open circles are sub-segment 3a prior to filtration. Orange circles are sub-segment 3a after filtration.

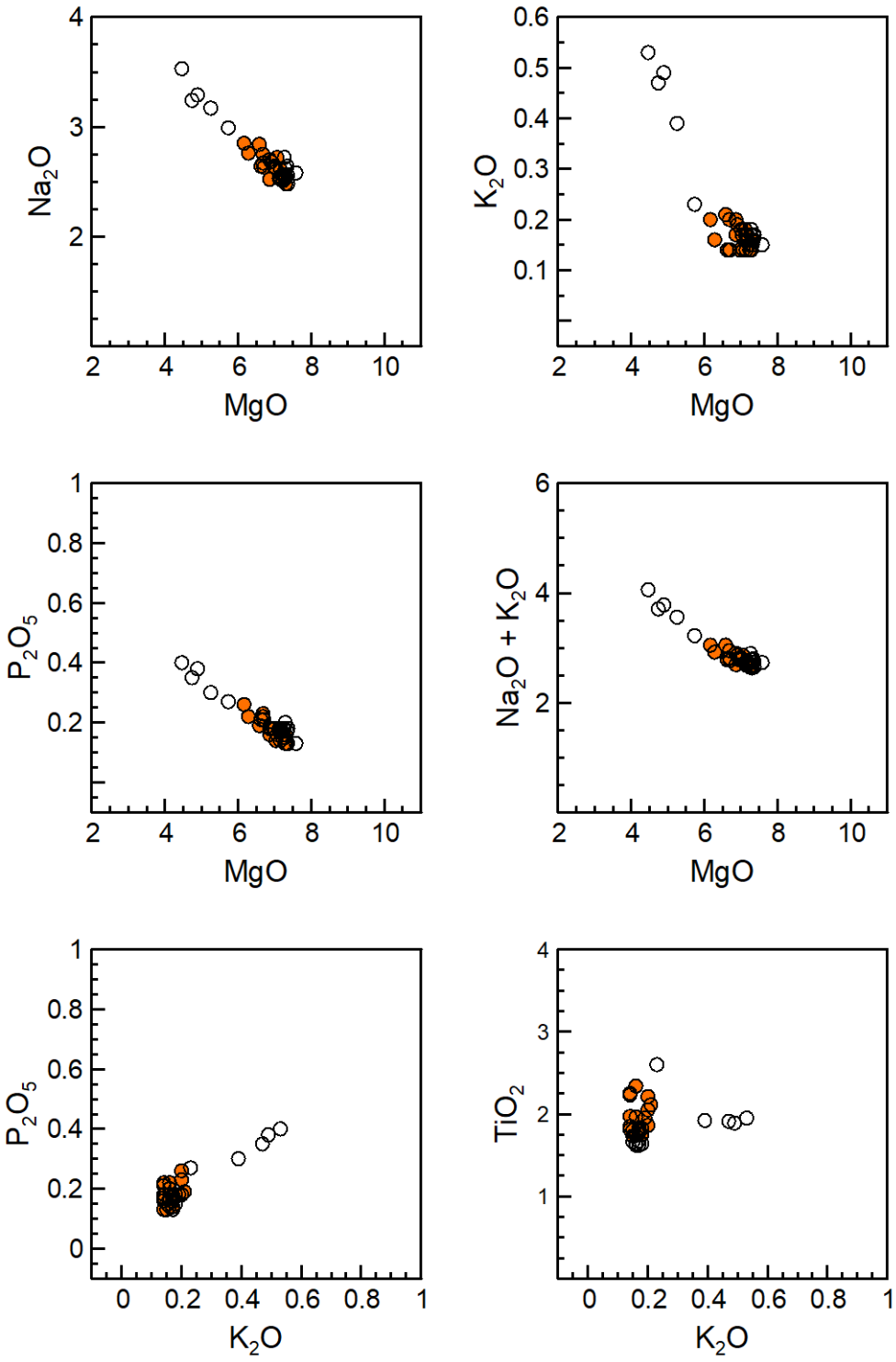

Figure 3.5: Sub-segment 3a filtration example showing incompatible oxides. Open circles are sub-segment 3a prior to filtration. Orange circles are sub-segment 3a after filtration.

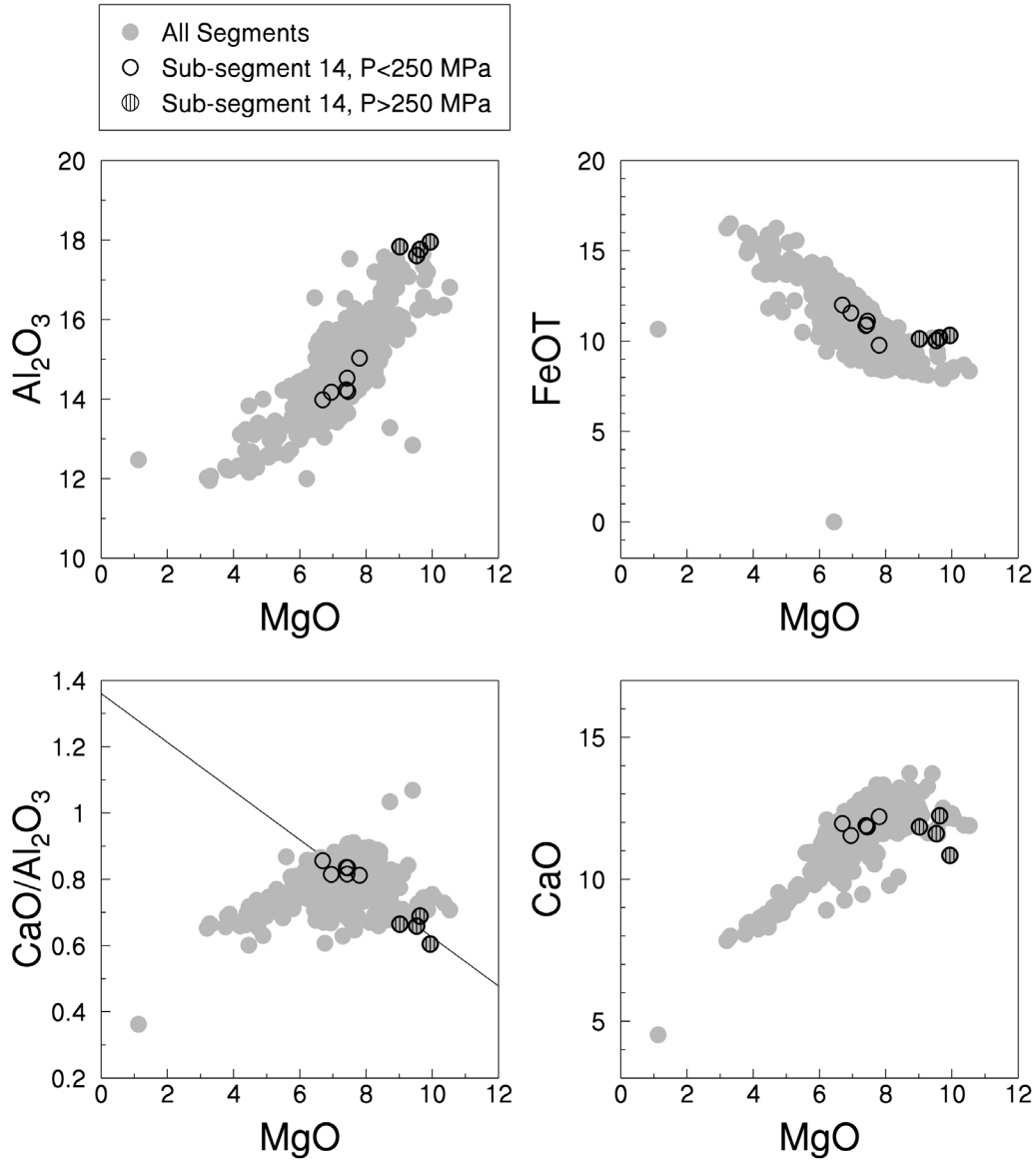

Figure 3.6: Sub-segment 14 filtration example. Grey circles are the entire JdFR dataset. Open circles are samples from sub-segment 14 with pressures <250 MPa, and hatched circles are sub-segment 14 samples with pressures >250 MPa.

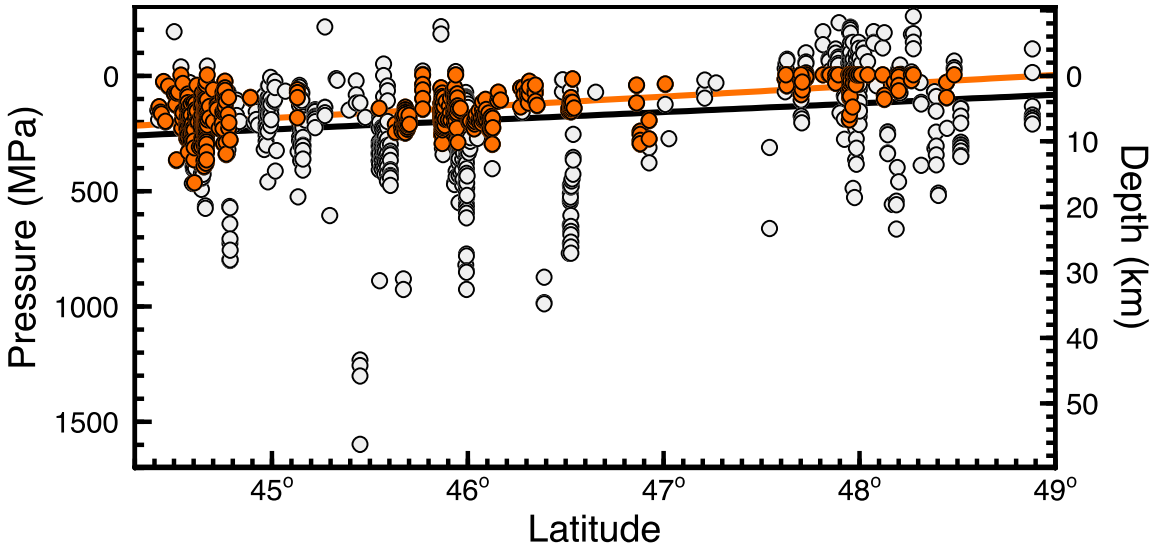

Figure 3.7: Pressure vs. Latitude along the strike of the JdFR. Open circles indicate raw pressure results, and orange fill indicates filtered pressure results. Lines are a one-degree polynomial regression on the filtered (orange) and unfiltered (black) data. Depth is calculated assuming a crustal density of 2900 kg/m^3.

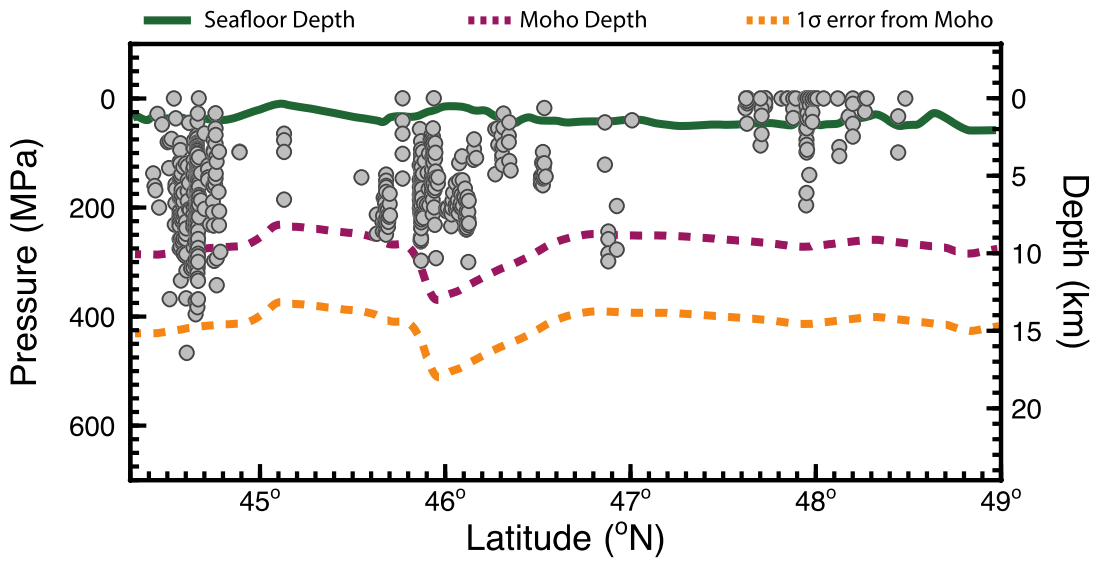

Figure 3.8: Filtered dataset pressure and depth vs. latitude along the JdFR. Grey markers indicate filtered pressures. Green solid line indicates depth of the seafloor. Purple dashed line indicates depth of the Moho. Yellow dashed line indicates 1σ error of the Moho. Depth of the Moho from Hooft and Detrick (1995), Carbotte et al. (2008), after Scott (2017). Depth is calculated assuming a crustal density of 2900 kg/m^3.

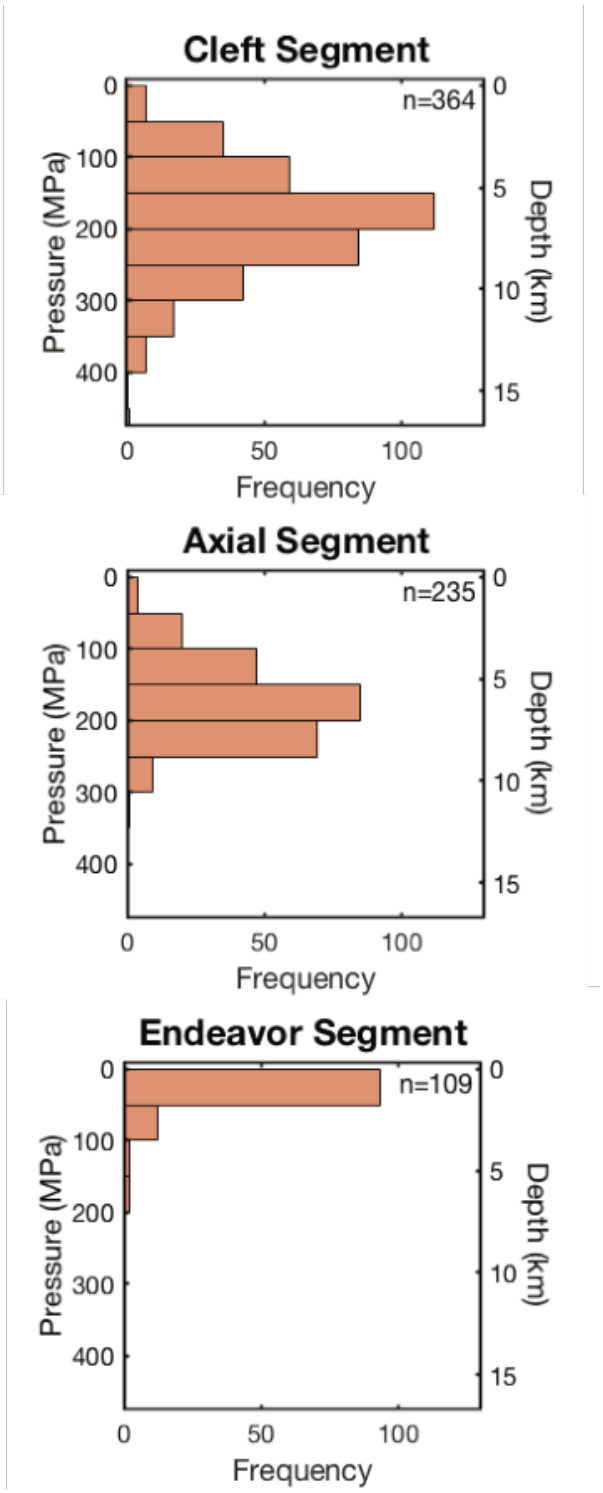

Figure 3.9: Filtered pressure histograms for the Cleft, Axial, and Endeavor Segments. Depth is calculated assuming a crustal density of 2900 kg/m^3.

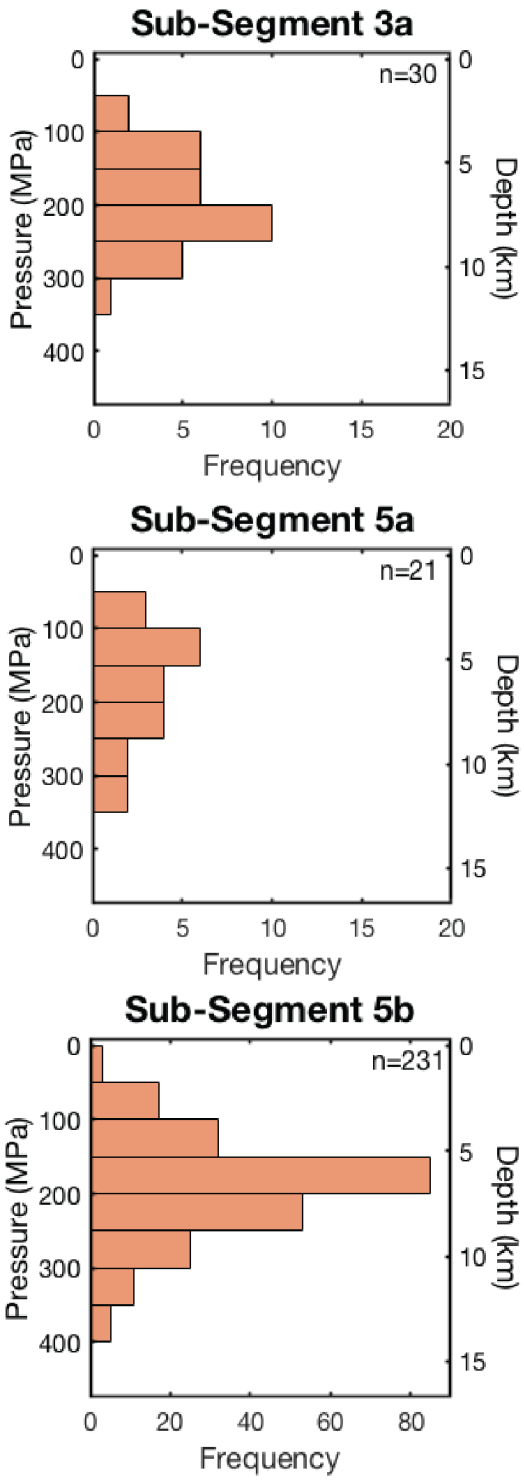

Figure 3.10: Filtered pressure histograms for three sub-segments from the Cleft segment. Depth is calculated assuming a crustal density of 2900 kg/m^3.

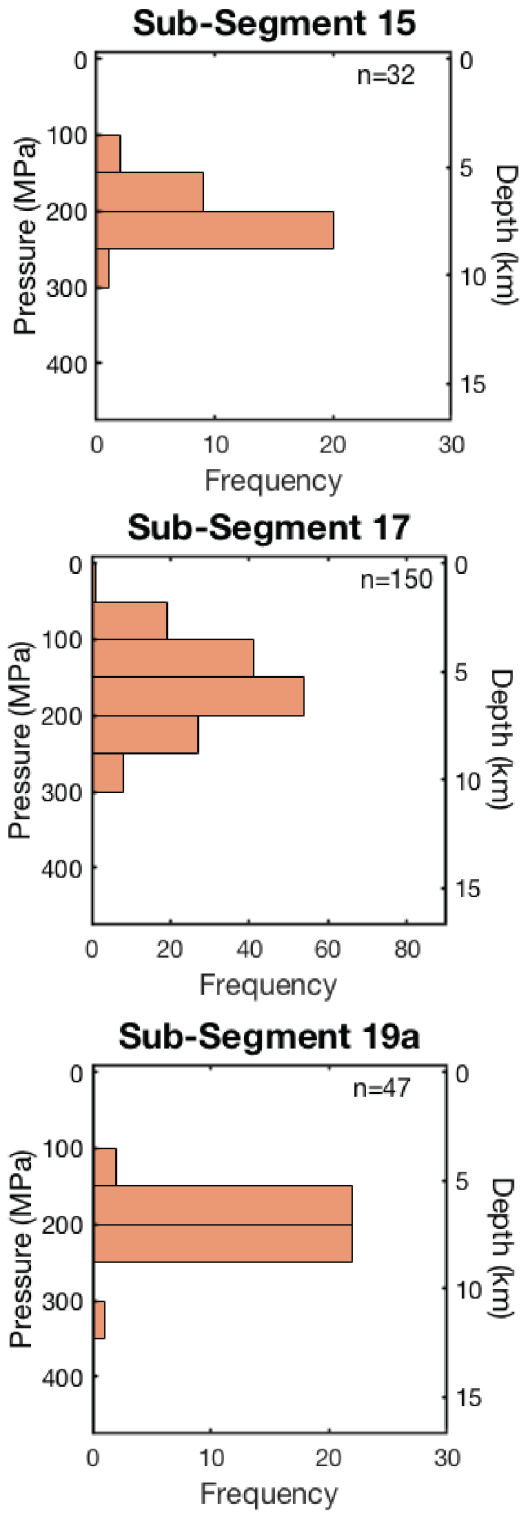

Figure 3.11: Filtered pressure histograms for three sub-segments from the Axial segment. Depth is calculated assuming a crustal density of 2900 kg/m^3.

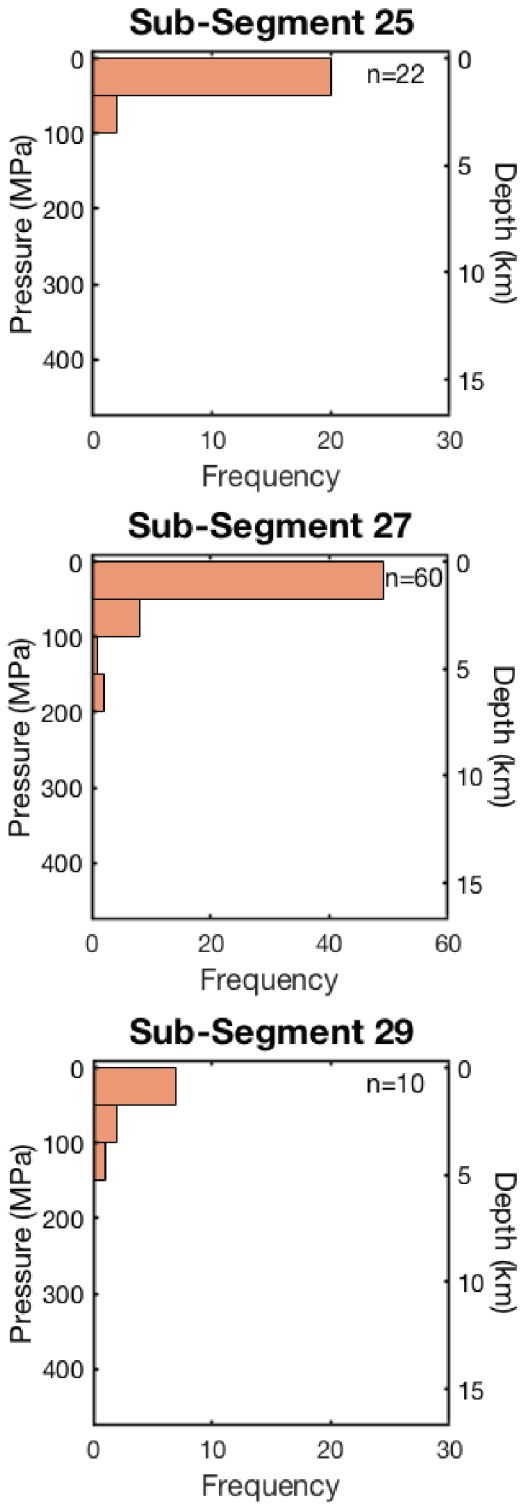

Figure 3.12: Filtered pressure histograms for three sub-segments from the Endeavor segment. Depth is calculated assuming a crustal density of 2900 kg/m^3.

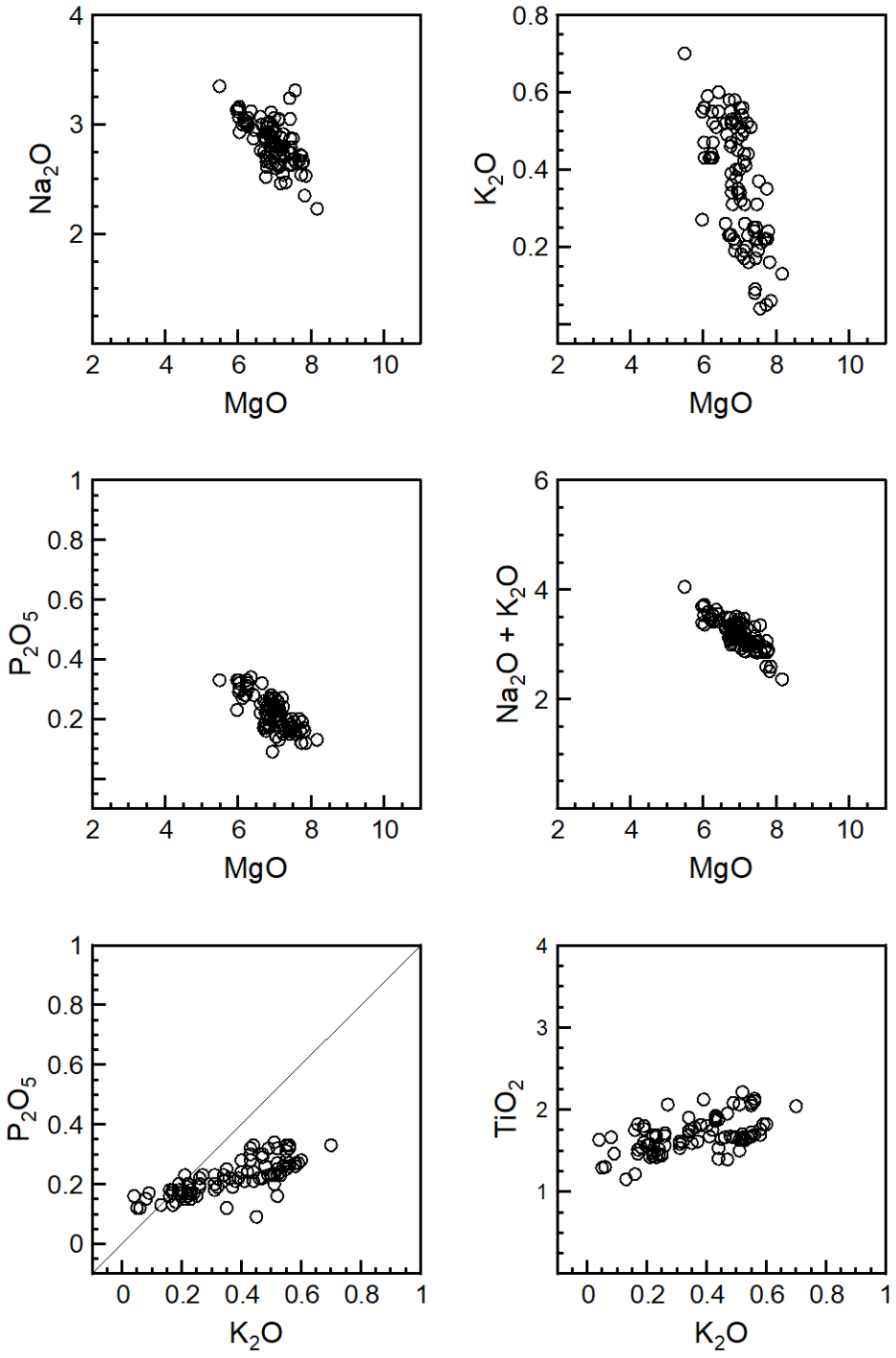

Figure 3.13: Incompatible elements and Alkalis from the Endeavor segment filtered dataset. A 1:1 line is plotted for K_2O vs. P_2O_5, illustrating anomalously high K_2O relative to P_2O_5.

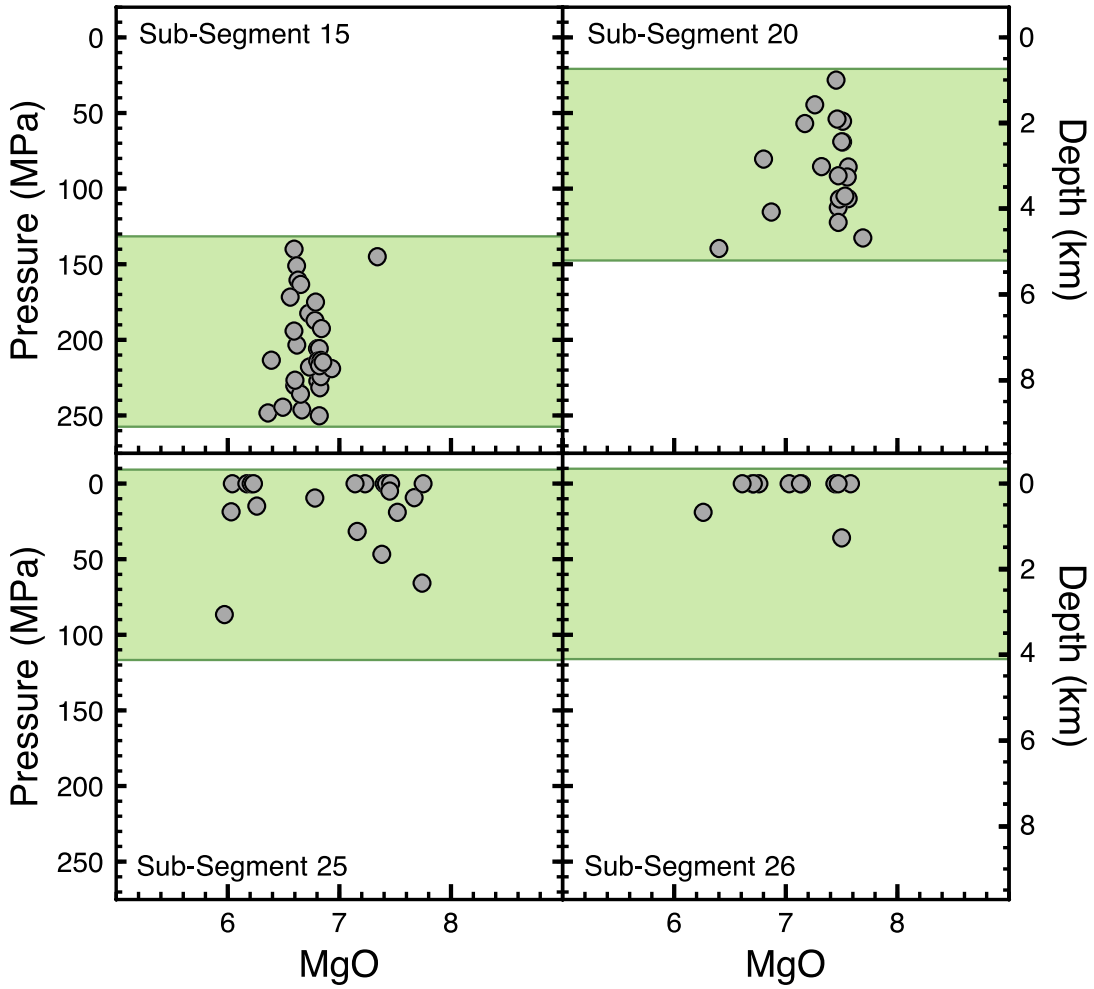

Figure 3.14: Sub-segments with potential melt lenses. Green boxes indicate range of 126 MPa, which is the 1σ error on the KB method. Depth is calculated assuming a crustal density of 2900 kg/m^3. Sub-segments 15, 20, 25, and 26 have a small range of pressures, which suggests the presence of melt lenses or melt ponding at these locations.

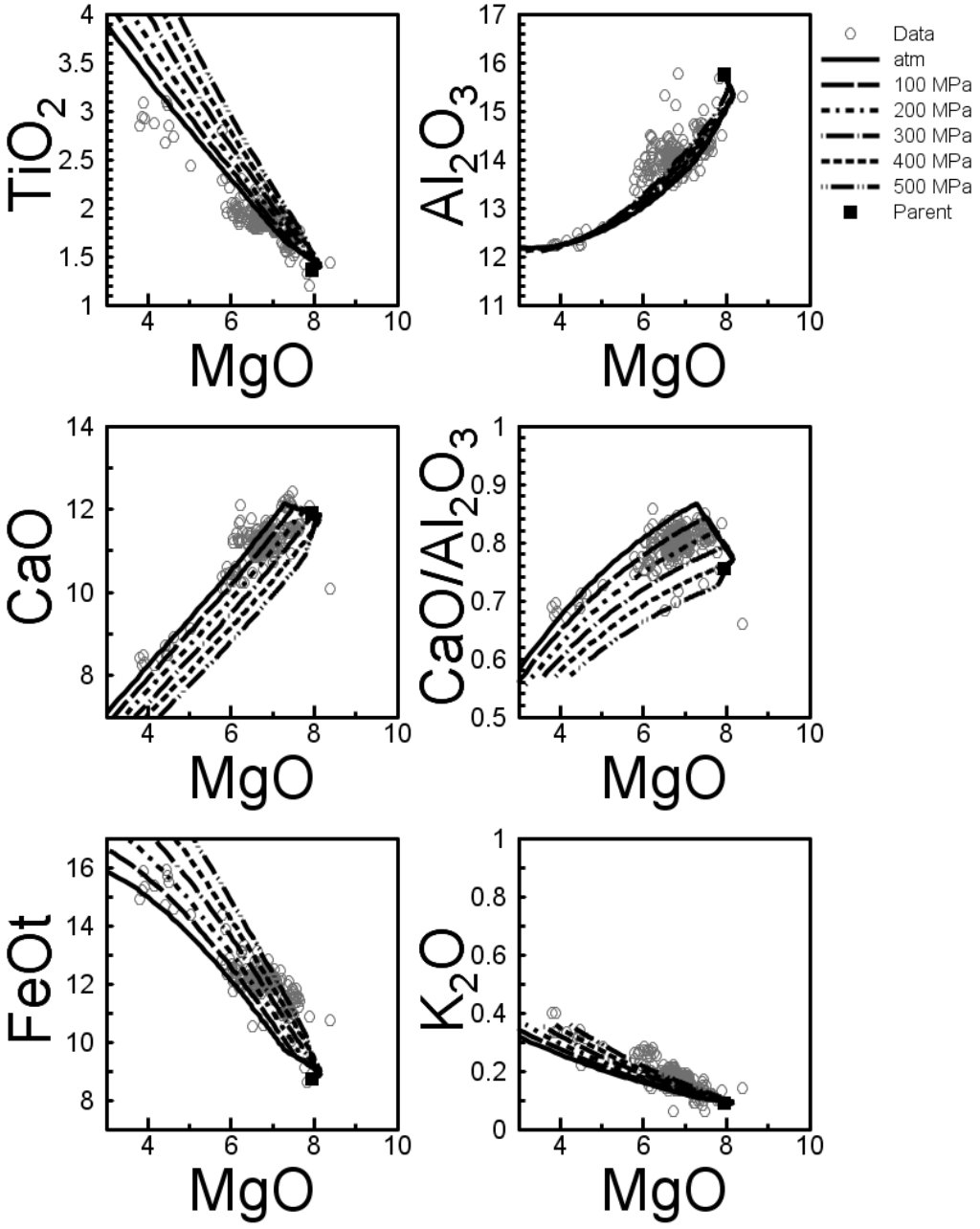

Figure 3.15: Modeled LLDs for the southern portion of the JdFR (Blanco Fracture Zone and Cleft segment). Model is anhydrous. Grey circles are the unfiltered JdFR data.

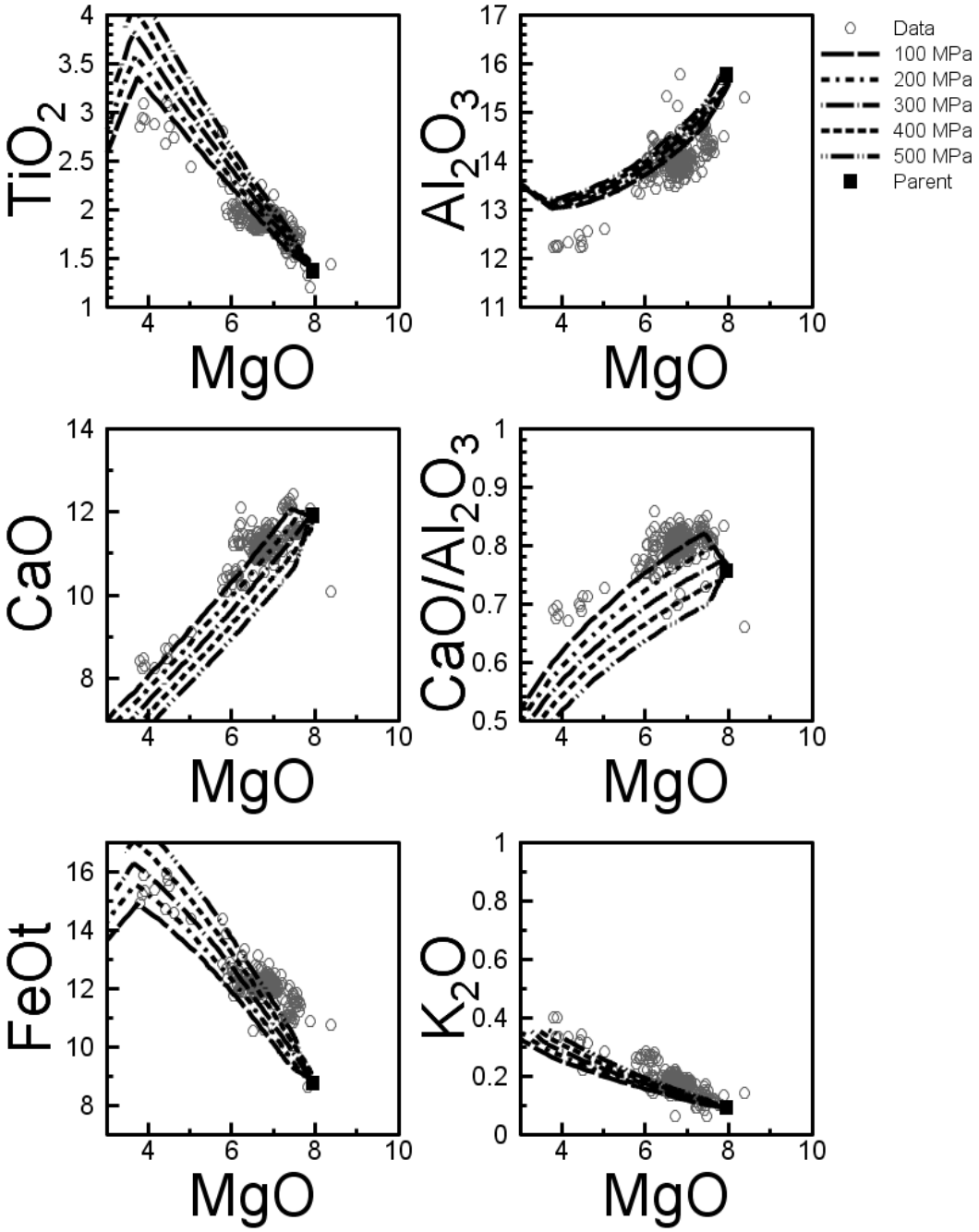

Figure 3.16: Modeled LLDs for the southern portion of the JdFR (Blanco Fracture Zone and Cleft segment). Model assumes presence of 0.1 wt. % water. Grey circles are the unfiltered JdFR data.

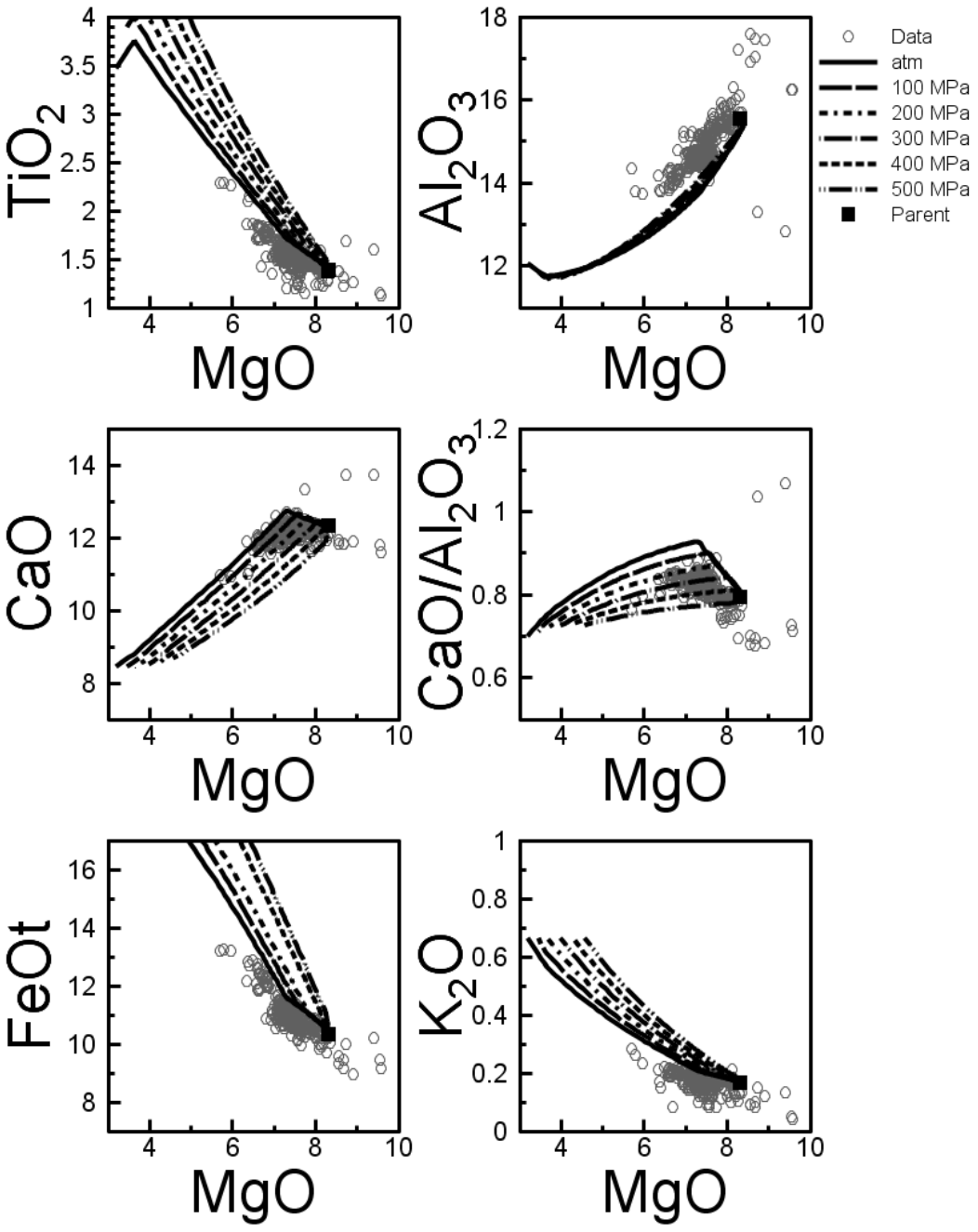

Figure 3.17: Modeled LLDs for the Axial segment. Model is anhydrous. Grey circles are the unfiltered JdFR data.

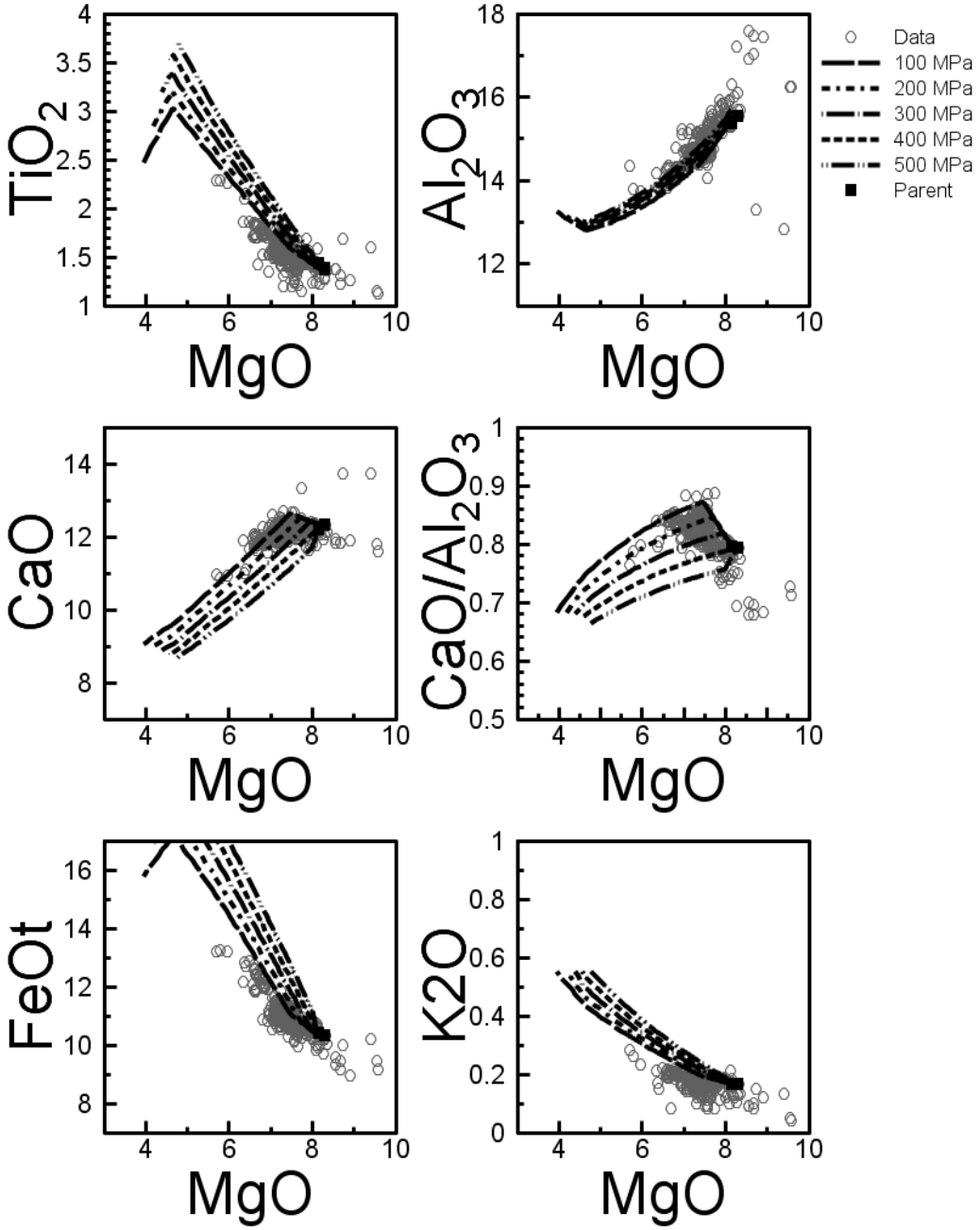

Figure 3.18: Modeled LLDs for the Axial segment. Model assumes presence of 0.1 wt. % water. Grey circles are the unfiltered JdFR data.

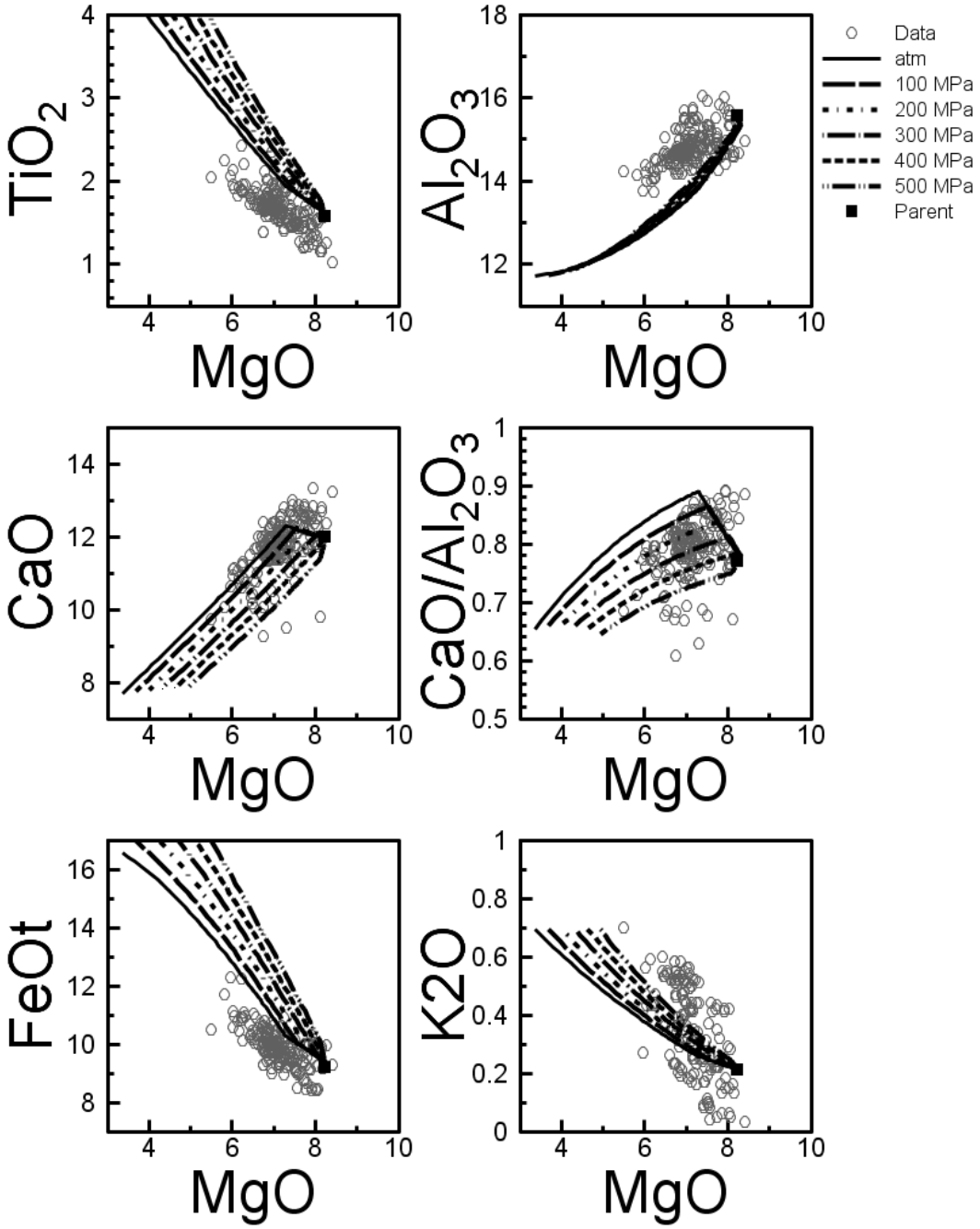

Figure 3.19: Modeled LLDs for the Endeavor segment. Model is anhydrous. Grey circles are the unfiltered JdFR data.

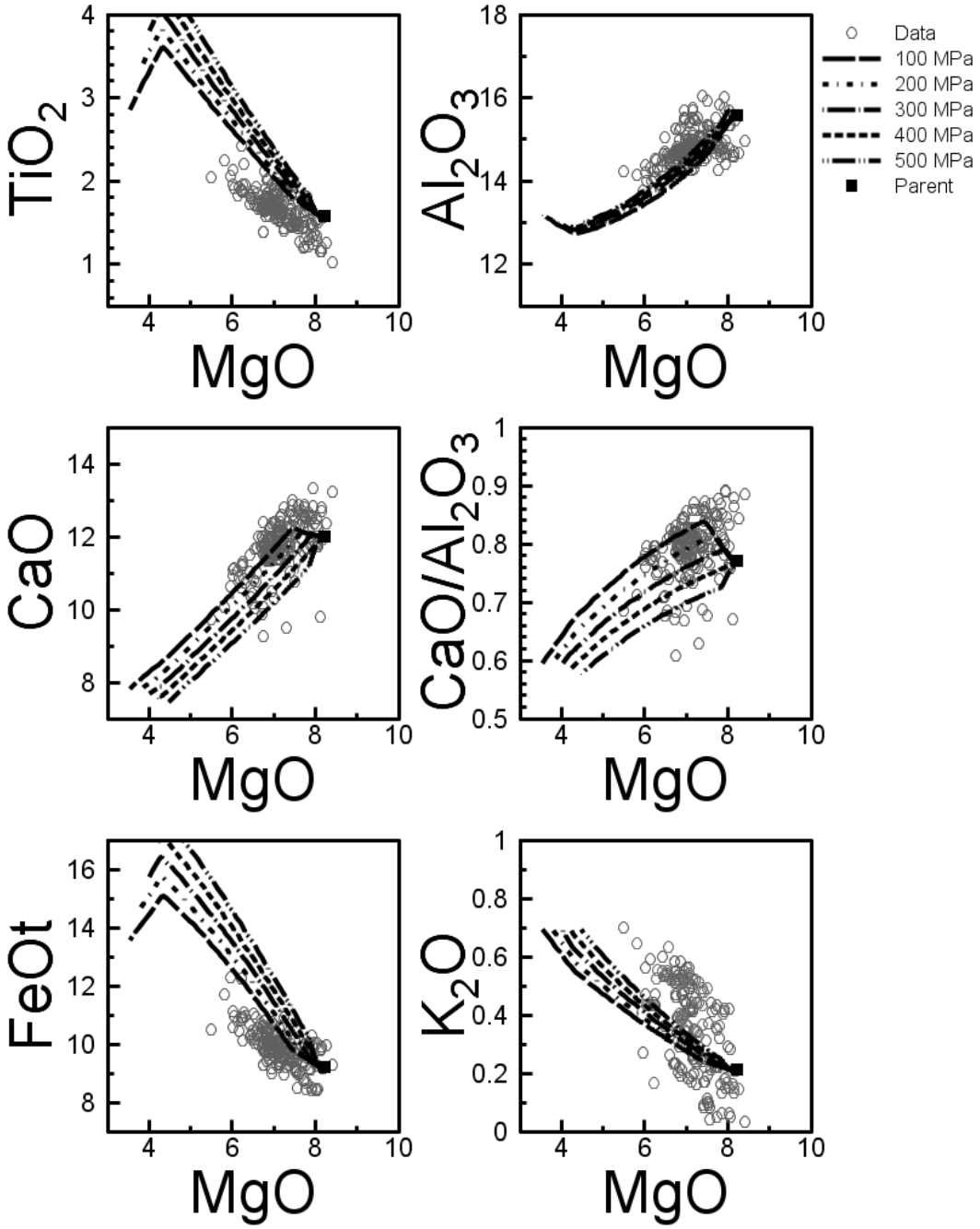

Figure 3.20: Modeled LLDs for the Endeavor segment. Model assumes presence of 0.1 wt. % water. Grey circles are the unfiltered JdFR data.

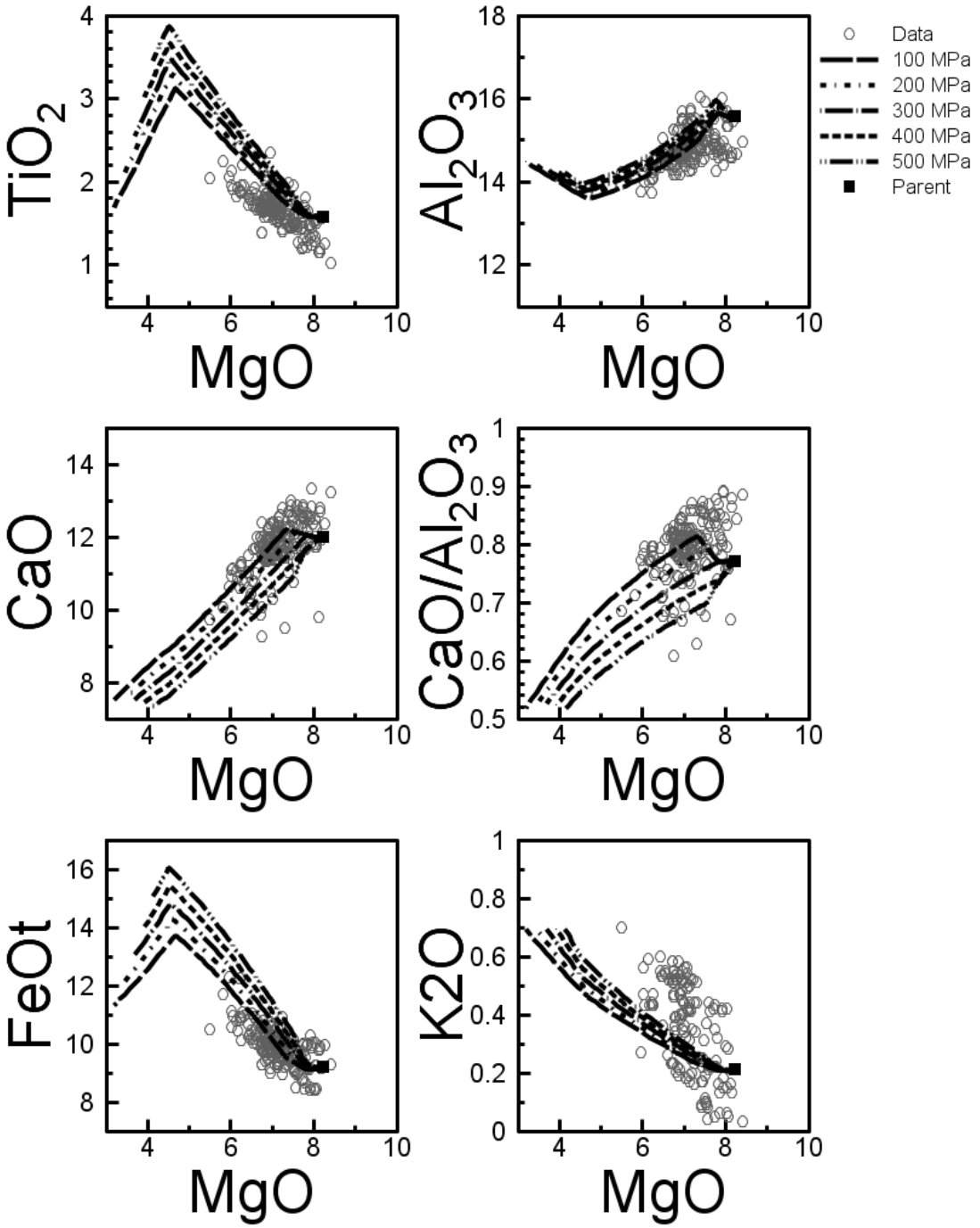

Figure 3.21: Modeled LLDs for the Endeavor segment. Model assumes presence of 0.3 wt. % water. Grey circles are the unfiltered JdFR data.

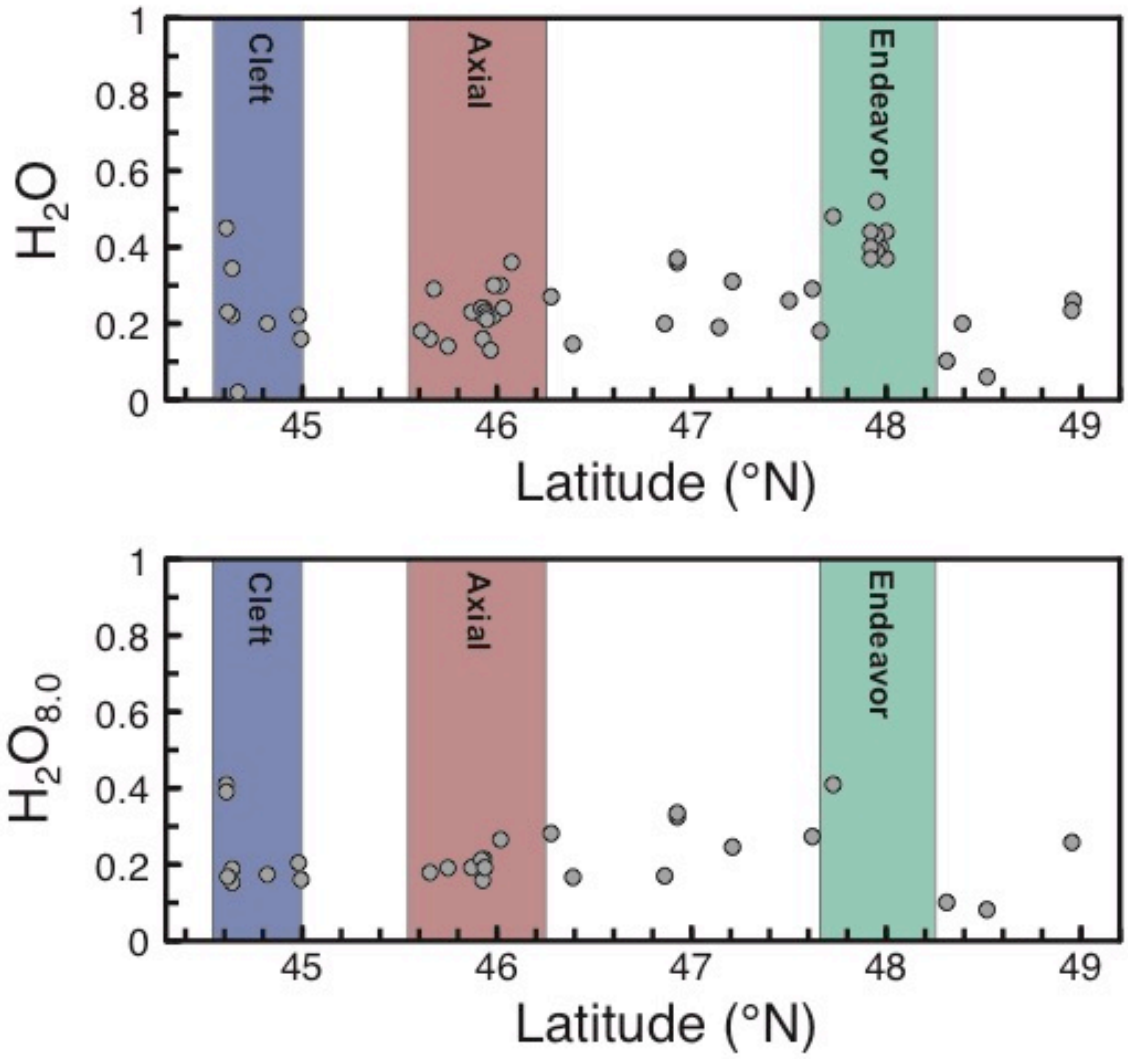

Figure 3.22: Water variation along the strike of the JdFR. The top graph shows water variation prior to normalization. The bottom graph shows water normalized to $water_{8.0}$. Missing data points in the normalized data are due to incomplete analyses, which do not allow for calculation of $water_{8.0}$. Locations of the Cleft, Axial, and Endeavor segments are indicated.

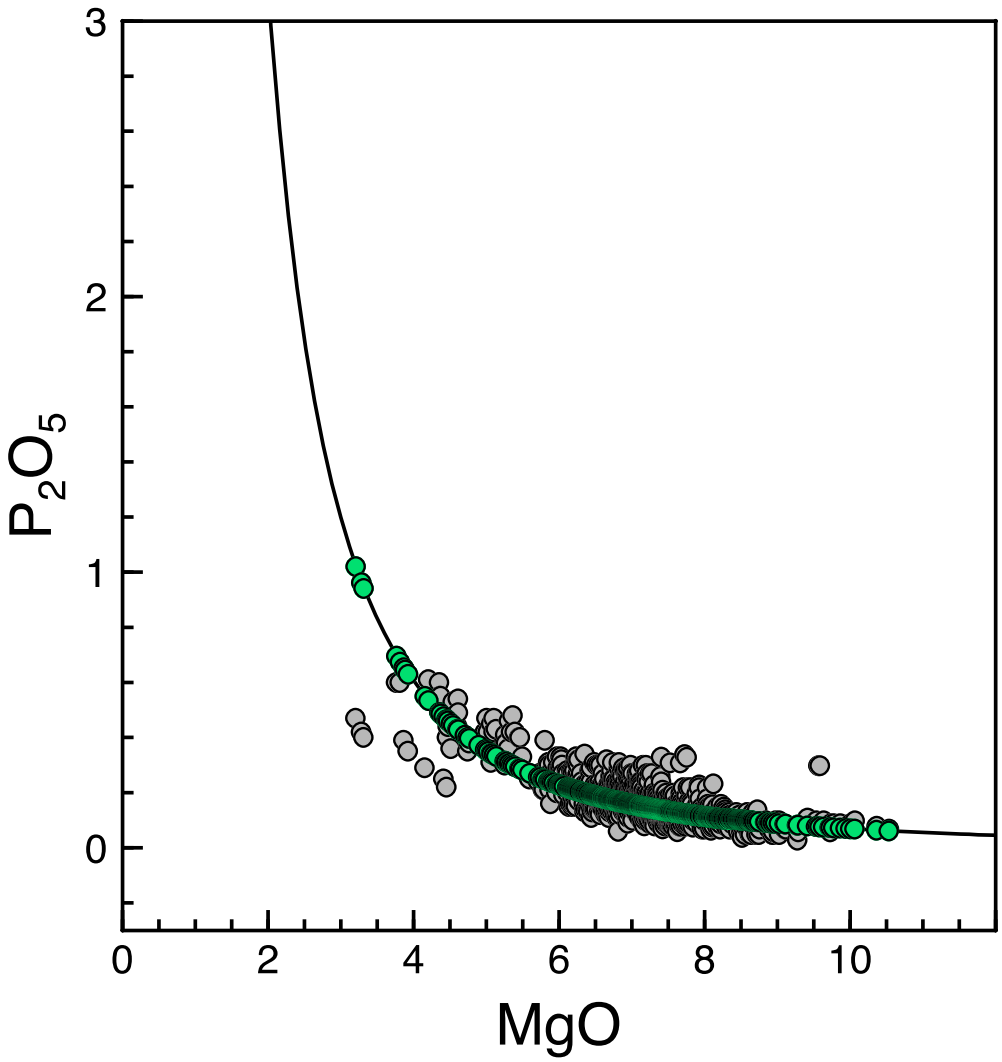

Figure 3.23: Modeled P_2O_5 for the unfiltered JdFR dataset. Grey circles are observed wt. % P_2O_5, whereas green circles are modeled P_2O_5. Regression line (black curve) is fit to the observed data excluding the samples for which P_2O_5 has not been measured. MgO and P_2O_5 are given as wt. %.

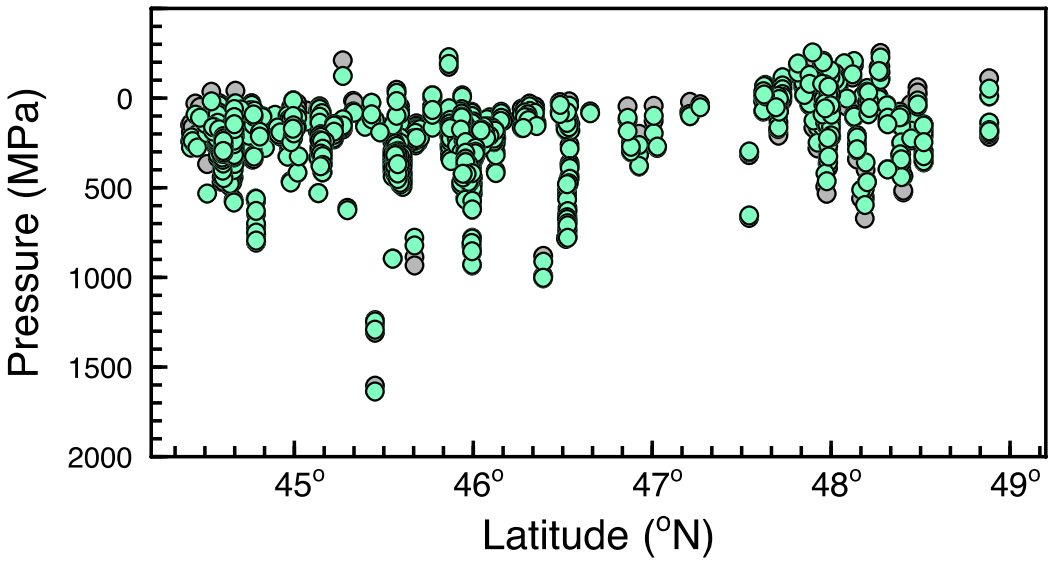

Figure 3.24: Modeled P_2O_5 (green circles) and observed P_2O_5 (grey circles) pressures vs. latitude (°N) for the unfiltered JdFR dataset.

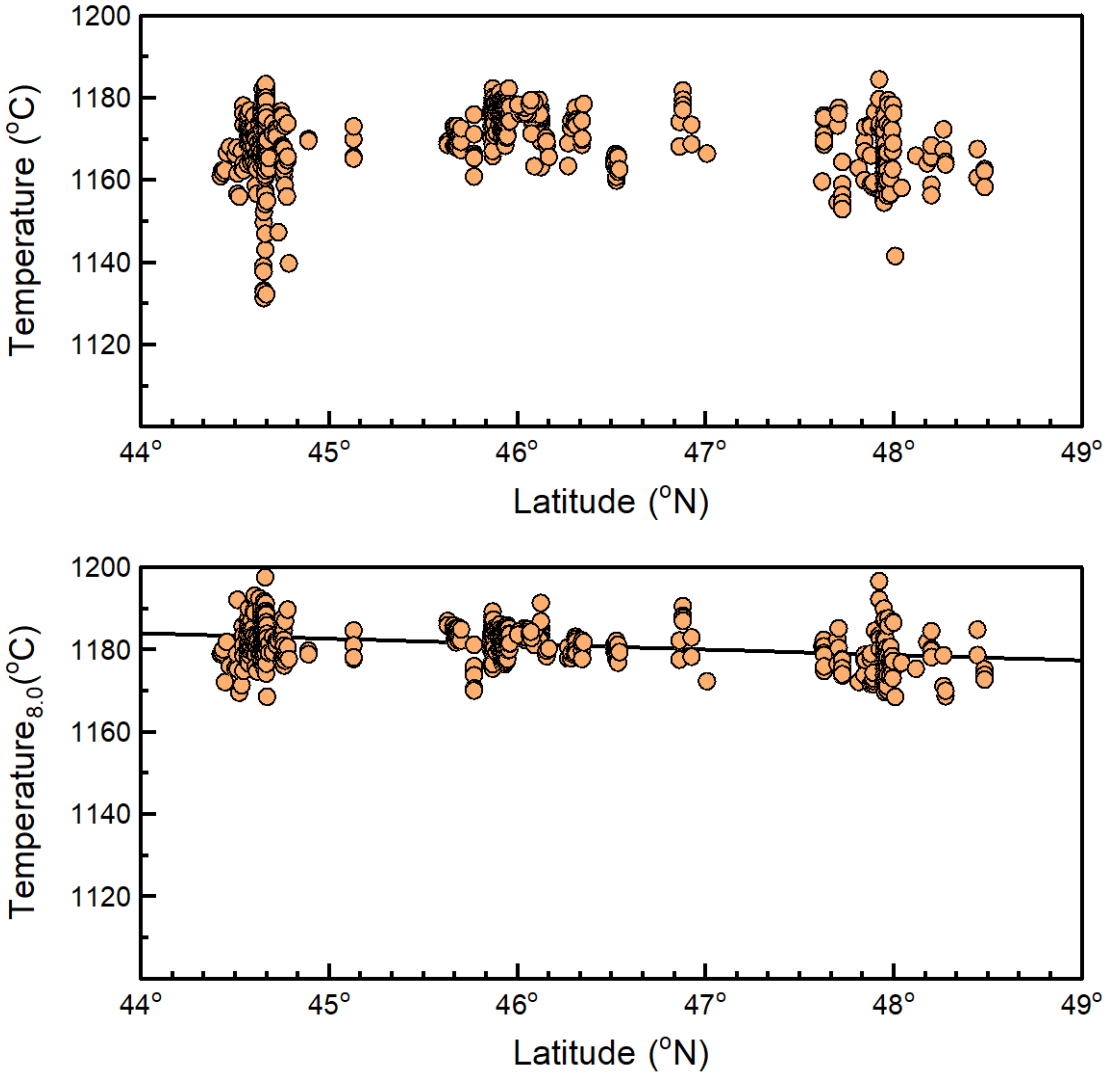

Figure 3.25: Temperature along the strike of the JdFR. Prior to $Temp_{8.0}$ normalization, the highest temperatures occur in the southern portion of the ridge, and the lowest temperatures in the center of the ridge. After normalization, there is slight decrease in average temperatures from south to north, but this decrease is within error of the temperature calculation.

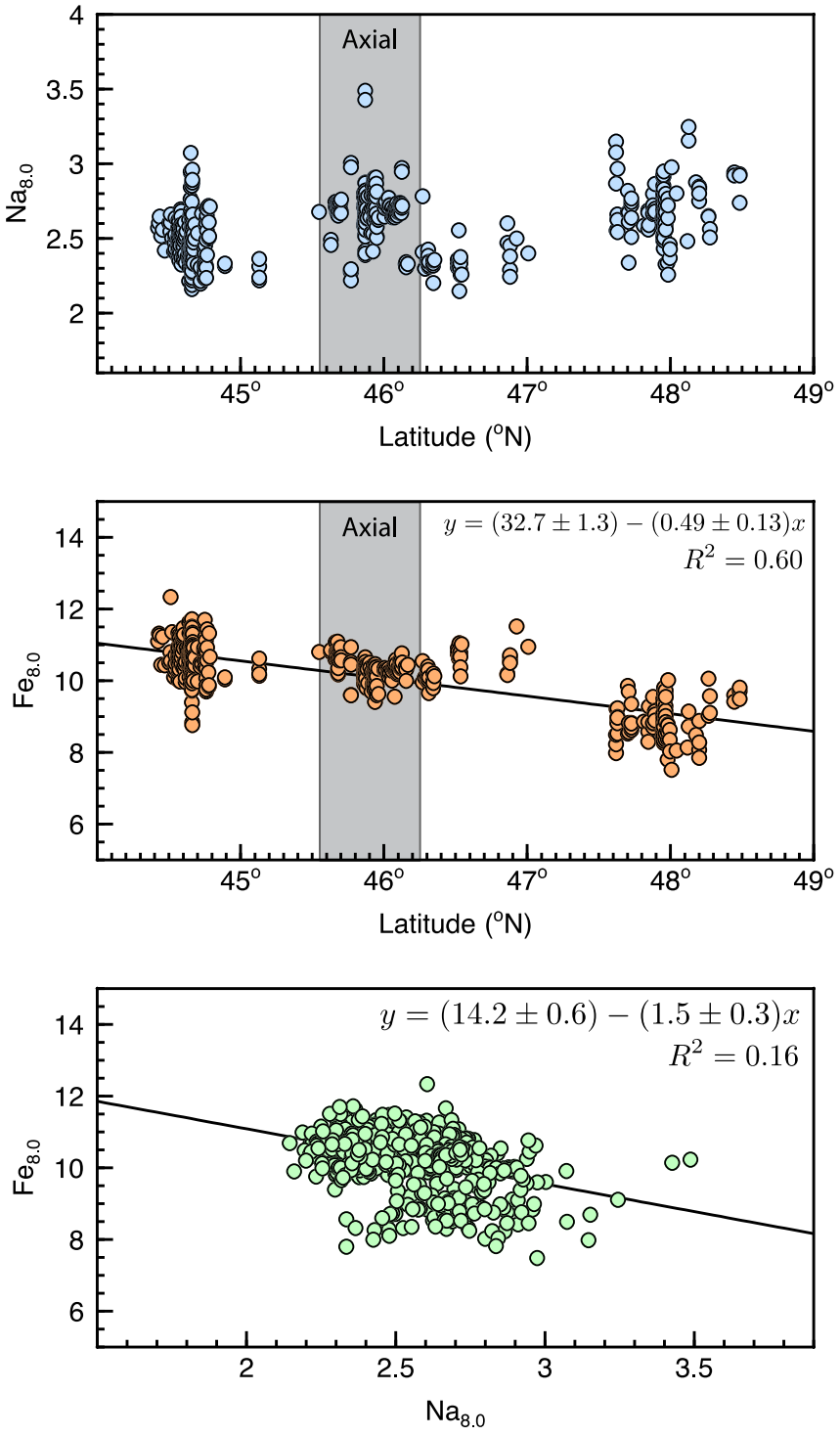

Figure 3.26: Variations in $Fe_{8.0}$ and $Na_{8.0}$ along the JdFR. $Na_{8.0}$ remains constant (top), whereas $Fe_{8.0}$ decreases from south to north (middle). The location of the Axial segment is indicated by the grey box. $Fe_{8.0}$ and $Na_{8.0}$ have a weak negative correlation (bottom).

Chapter 4. Conclusions

This study uses *liq-ol-cpx-plag* cotectic major-element geobarometry to constrain the depths of *liq-ol-cpx-plag* cotectic crystallization in mafic igneous systems and provide insight into crystallization depths and processes along an intermediate-rate spreading ridge. The conclusions of this study are presented here:

1. The removal of samples that do not lie on the *liq-ol-cpx-plag* cotectic significantly alters the interpretation of pressure results. The samples removed give pressure results that are outside the assumptions made for *liq-ol-cpx-plag* cotectic crystallization, for which the meaning is not clear. Therefore, the removal of all potentially ambiguous samples allows for the most reliable estimate of depths of crystallization.
2. The optimization of *liq-ol-cpx-plag* cotectic geobarometry results provides high-resolution insight into the pressures of partial crystallization in mafic igneous systems.
3. Pressure results using the KB geobarometer suggest that *liq-ol-cpx-plag* cotectic crystallization occurs within the crust along the JdFR, with greater depths of *liq-ol-cpx-plag* cotectic crystallization in regions of thickened crust.
4. These results indicate that a significant amount of *liq-ol-cpx-plag* cotectic crystallization occurs at greater depths than seismically imaged melt lenses in the

southern portion of the JdFR, but at shallower depths in the northern section of the ridge. This may be explained by (1) seismically imaged melt lenses being short-lived, or (2) the bulk of crystallization occurring in low melt-percent crystal mushes or small dikes, which are not as easily imaged in seismic studies.

Bibliography

Argus, D. F. & Gordon, R. G. (1991). No-net-rotation model of current plate velocities incorporating plate motion model NUVEL-1. *Geophysical Research Letters* **18**, 2039–2042.

Ariskin, A. A. (1999). Phase equilibria modeling in igneous petrology: use of COMAGMAT model for simulating fractionation of ferro-basaltic magmas and the genesis of high-alumina basalt. Journal of Volcanology and Geothermal Research 90, 115–162.

Arnulf, A. F., Harding, A. J., Kent, G. M. & Wilcock, W. S. D. (2018). Structure, Seismicity, and Accretionary Processes at the Hot Spot-Influenced Axial Seamount on the Juan de Fuca Ridge. *Journal of Geophysical Research: Solid Earth* **123**, 4618–4646.

Baker, E. T. (2009). Relationships between hydrothermal activity and axial magma chamber distribution, depth, and melt content. *Geochemistry, Geophysics, Geosystems* **10**.

Baker, E. T., Chen, Y. J. & Phipps Morgan, J. (1996). The relationship between near-axis hydrothermal cooling and the spreading rate of mid-ocean ridges. *Earth and Planetary Science Letters* **142**, 137–145.

Barr, S. M. & Chase, R. L. (1974). Geology of the Northern End of Juan de Fuca Ridge and Sea-Floor Spreading. *Canadian Journal of Earth Sciences*. NRC Research Press **11**, 1384–1406.

Battaglia, M., Gottsmann, J., Carbone, D. & Fernández, J. (2008). 4D volcano gravimetry. *Geophysics* **73**, WA3–WA18.

CAMECA (2015). Electron Probe Microanalysis. John Wiley & Sons, Ltd.

Canales, J. P., Detrick, R. S., Carbotte, S. M., Kent, G. M., Diebold, J. B., Harding, A., Babcock, J., Nedimović, M. R. & van Ark, E. (2005). Upper crustal structure and axial topography at intermediate spreading ridges: Seismic constraints from the southern Juan de Fuca Ridge. *Journal of Geophysical Research* **110**, B12104.

Canales, J. P., Nedimović, M. R., Kent, G. M., Carbotte, S. M. & Detrick, R. S. (2009). Seismic reflection images of a near-axis melt sill within the lower crust at the Juan de Fuca ridge. *Nature*. Nature Publishing Group **460**, 89–93.

Canales, J. P., Singh, S. C., Detrick, R. S., Carbotte, S. M., Harding, A., Kent, G. M., Diebold, J. B., Babcock, J. & Nedimović, M. R. (2006). Seismic evidence for variations in axial magma chamber properties along the southern Juan de Fuca Ridge. *Earth and Planetary Science Letters* **246**, 353–366.

Carbotte, S. M., Canales, J. P., Nedimovic, M. R., Carton, H. & Mutter, J. C. (2012). Recent Seismic Studies at the East Pacific Rise 8 degrees 20 '-10 degrees 10 ' N and Endeavour Segment Insights into Mid-Ocean Ridge Hydrothermal and Magmatic Processes. .

Carbotte, S. M., Detrick, R. S., Harding, A., Canales, J. P., Babcock, J., Kent, G., Ark, E. V., Nedimovic, M. & Diebold, J. (2006). Rift topography linked to magmatism at the intermediate spreading Juan de Fuca Ridge. *Geology*. GeoScienceWorld **34**, 209–212.

Carbotte, S. M., Nedimović, M. R., Canales, J. P., Kent, G. M., Harding, A. J. & Marjanović, M. (2008). Variable crustal structure along the Juan de Fuca Ridge: Influence of on-axis hot spots and absolute plate motions. Geochemistry, Geophysics, Geosystems 9.

Cashman, K. V. & Sparks, R. S. J. (2013). How volcanoes work: A 25 year perspective. GSA Bulletin. GeoScienceWorld 125, 664–690.

Chadwick, J., Perfit, M., Ridley, I., Jonasson, I., Kamenov, G., Chadwick, W., Embley, R., Roux, P. le & Smith, M. (2005). Magmatic effects of the Cobb hot spot on the Juan de Fuca Ridge. *Journal of Geophysical Research: Solid Earth* **110**.

Chadwick, W. W. et al. (2016). Voluminous eruption from a zoned magma body after an increase in supply rate at Axial Seamount. Geophysical Research Letters 43.

Clague, D. A., Paduan, J. B., Dreyer, B. M., Chadwick, W. W., Rubin, K. R., Perfit, M. R. & Fundis, A. T. (2018). Chemical Variations in the 1998, 2011, and 2015 Lava Flows From Axial Seamount, Juan de Fuca Ridge: Cooling During Ascent, Lateral Transport, and Flow. *Geochemistry, Geophysics, Geosystems* **19**, 2915–2933.

Clague, David. A. et al. (2014). Eruptive and tectonic history of the Endeavour Segment, Juan de Fuca Ridge, based on AUV mapping data and lava flow ages. *Geochemistry, Geophysics, Geosystems* **15**, 3364–3391.

Cordier, C., Caroff, M., Juteau, T., Fleutelot, C., Hémond, C., Drouin, M., Cotten, J. & Bollinger, C. (2007). Bulk-rock geochemistry and plagioclase zoning in lavas exposed along the northern flank of the Western Blanco Depression (Northeast Pacific): Insight into open-system magma chamber processes. *Lithos* **99**, 289–311.

Cormier, M.-H., Detrick, R. S. & Purdy, G. M. (1984). Anomalously thin crust in oceanic fracture zones: New seismic constraints from the Kane Fracture Zone. *Journal of Geophysical Research: Solid Earth* **89**, 10249–10266.

Cottrell, E. & Kelley, K. A. (2011). The oxidation state of Fe in MORB glasses and the oxygen fugacity of the upper mantle. *Earth and Planetary Science Letters* **305**, 270–282.

Cousens, B. L., Allan, J. F., Leybourne, M. I., Chase, R. L. & Van Wagoner, N. (1995). Mixing of magmas from enriched and depleted mantle sources in the northeast Pacific: West Valley segment, Juan de Fuca Ridge. *Contributions to Mineralogy and Petrology* **120**, 337–357.

Crisp, J. A. (1984). Rates of magma emplacement and volcanic output. Journal of Volcanology and Geothermal Research 20, 177–211.

Danyushevsky, L. V., Eggins, S. M., Falloon, T. J. & Christie, D. M. (2000). H2O Abundance in Depleted to Moderately Enriched Mid-ocean Ridge Magmas; Part I: Incompatible Behaviour, Implications for Mantle Storage, and Origin of Regional Variations. *Journal of Petrology*. Oxford Academic **41**, 1329–1364.

Danyushevsky, L. V. & Plechov, P. (2011). Petrolog3: Integrated software for modeling crystallization processes. *Geochemistry, Geophysics, Geosystems* **12**.

Danyushevsky, L. V., Sobolevz, A. V. & Dmitrievz, L. V. (1996). Estimation of the pressure of crystallization and H2O content of MORB and BABB glasses: calibration of an empirical technique. *Mineralogy and Petrology* **57**, 185–204.

Delaney, J. R., Robigou, V., McDuff, R. E. & Tivey, M. K. (1992). Geology of a vigorous hydrothermal system on the Endeavour Segment, Juan de Fuca Ridge. *Journal of Geophysical Research: Solid Earth* **97**, 19663–19682.

Desonie, D. L. & Duncan, R. A. (1990a). The Cobb-Eickelberg Seamount Chain: Hotspot volcanism with mid-ocean ridge basalt affinity. *Journal of Geophysical Research: Solid Earth* **95**, 12697–12711.

Desonie, D. L. & Duncan, R. A. (Oregon S. U. (1990b). The Cobb-Eickelberg seamount chain: Hotspot volcanism with mid-ocean ridge basalt affinity. *Journal of Geophysical Research; (United States)* **95:B8**.

Dick, H. et al. (2002). Primary silicate mineral chemistry of a 1.5-km section of very slow spreading lower ocean crust: ODP Hole 735B, Southwest Indian Ridge. Proceedings of Ocean Drilling Program, Scientific Results. Ocean Drilling Program, 1–60.

Dixon, J. E., Stolper, E. & Delaney, J. R. (1988). Infrared spectroscopic measurements of CO2 and H2O in Juan de Fuca Ridge basaltic glasses. *Earth and Planetary Science Letters* **90**, 87–104.

Dzurisin, D. (2003). A comprehensive approach to monitoring volcano deformation as a window on the eruption cycle. *Reviews of Geophysics* **41**, 1001.

Eaby, J., Clague, D. A. & Delaney, J. R. (1984). Sr isotopic variations along the Juan de Fuca Ridge. *Journal of Geophysical Research* **89**, 8.

Elthon, D. (1993). The crystallization of mid-ocean ridge basalts at moderate and high pressures. *European Journal of Mineralogy*. GeoScienceWorld **5**, 1025–1037.

Elthon, D. & Scarfe, C. M. (1984). High-pressure phase equilibria of a high-magnesia basalt and the genesis of primary oceanic basalts. *American Mineralogist*. GeoScienceWorld **69**, 1–15.

Gaetani, G. A., DeLong, S. E. & Wark, D. A. (1995). Petrogenesis of basalts from the Blanco Trough, northeast Pacific: Inferences for off-axis melt generation. *Journal of Geophysical Research: Solid Earth* **100**, 4197–4214.

Gale, A., Dalton, C. A., Langmuir, C. H., Su, Y. & Schilling, J.-G. (2013). The mean composition of ocean ridge basalts. *Geochemistry, Geophysics, Geosystems* **14**, 489–518.

Ghose, I., Cannat, M. & Seyler, M. (1996). Transform fault effect on mantle melting in the MARK area (Mid-Atlantic Ridge south of the Kane transform). *Geology* **24**.

Gregg, P. M., Behn, M. D., Lin, J. & Grove, T. L. (2009). Melt generation, crystallization, and extraction beneath segmented oceanic transform faults. American Geophysical Union.

Gregg, P. M., Lin, J., Behn, M. D. & Montési, L. G. J. (2007). Spreading rate dependence of gravity anomalies along oceanic transform faults. *Nature*. Nature Publishing Group **448**, 183–187.

Grove, T. L., Kinzler, R. J. & Bryan, W. B. (1992). Fractionation of Mid-Ocean Ridge Basalt (MORB). *Mantle Flow and Melt Generation at Mid-Ocean Ridges*. American Geophysical Union (AGU), 281–310.

Gudmundsson, A. (1990). Emplacement of dikes, sills and crustal magma chambers at divergent plate boundaries. *Tectonophysics* **176**, 257–275.

Gudmundsson, A. (2000). Dynamics of Volcanic Systems in Iceland: Example of Tectonism and Volcanism at Juxtaposed Hot Spot and Mid-Ocean Ridge Systems. *Annual Review of Earth and Planetary Sciences* **28**, 107–140.

Halldorsson, S. A., Oskarsson, N., Gronvold, K., Sigurdsson, G., Sverrisdottir, G. & Steinthorsson, S. (2008). Isotopic-heterogeneity of the Thjorsa lava—Implications for mantle sources and crustal processes within the Eastern Rift Zone, Iceland. *Chemical Geology* **255**, 305–316.

Hansen, H. & Grönvold, K. (1999). Plagioclase ultraphyric basalts in Iceland: the mush of the rift. *Journal of Volcanology and Geothermal Research* **98**, 1–32.

Hartley, M. E., Bali, E., Maclennan, J., Neave, D. A. & Halldórsson, S. A. (2018). Melt inclusion constraints on petrogenesis of the 2014–2015 Holuhraun eruption, Iceland. *Contributions to Mineralogy and Petrology* **173**, 10.

Herzberg, C. (2004). Partial Crystallization of Mid-Ocean Ridge Basalts in the Crust and Mantle. *Journal of Petrology*. Oxford Academic **45**, 2389–2405.

Herzberg, C. & O'hara, M. J. (2002). Plume-Associated Ultramafic Magmas of Phanerozoic Age. *Journal of Petrology*. Oxford Academic **43**, 1857–1883.

Hooft, E. E. E. & Detrick, R. S. (1995). Relationship between axial morphology, crustal thickness, and mantle temperature along the Juan de Fuca and Gorda Ridges. *Journal of Geophysical Research: Solid Earth* **100**, 22499–22508.

Iyer H.M. (1992) Seismological Detection and Delineation of Magma Chambers: Present Status with Emphasis on the Western USA. In: Gasparini P., Scarpa R., Aki K. (eds) Volcanic Seismology. IAVCEI Proceedings in Volcanology, vol 3. Springer, Berlin, Heidelberg.

Karsten, J. L. & Delaney, J. R. (1989). Hot spot-ridge crest convergence in the northeast Pacific. *Journal of Geophysical Research: Solid Earth* **94**, 700–712.

Karsten, J. L., Delaney, J. R., Rhodes, J. M. & Liias, R. A. (1990a). Spatial and temporal evolution of magmatic systems beneath the endeavour segment, Juan de Fuca Ridge: Tectonic and petrologic constraints. *Journal of Geophysical Research: Solid Earth* **95**, 19235–19256.

Kelemen, P. B., Koga, K. & Shimizu, N. (1997). Geochemistry of gabbro sills in the crust-mantle transition zone of the Oman ophiolite: implications for the origin of the oceanic lower crust. *Earth and Planetary Science Letters* **146**, 475–488.

Kelley, D. F. & Barton, M. (2008). Pressures of Crystallization of Icelandic Magmas. *Journal of Petrology*. Oxford Academic **49**, 465–492.

Klein, E. M. & Langmuir, C. H. (1987). Global correlations of ocean ridge basalt chemistry with axial depth and crustal thickness. *Journal of Geophysical Research: Solid Earth* **92**, 8089–8115.

Kress, V. C. & Carmichael, I. S. E. (1991). The compressibility of silicate liquids containing Fe2O3 and the effect of composition, temperature, oxygen fugacity and pressure on their redox states. *Contributions to Mineralogy and Petrology* **108**, 82–92.

Langmuir, C. & Forsyth, D. (2007a). Mantle Melting Beneath Mid-Ocean Ridges. *Oceanography* **20**, 78–89.

Langmuir, C. H., Klein, E. M. & Plank, T. (1992). Petrological Systematics of Mid-Ocean Ridge Basalts: Constraints on Melt Generation Beneath Ocean Ridges. *Mantle Flow and Melt Generation at Mid-Ocean Ridges*. American Geophysical Union (AGU), 183–280.

Lissenberg, C. J. & Dick, H. J. B. (2008). Melt–rock reaction in the lower oceanic crust and its implications for the genesis of mid-ocean ridge basalt. Earth and Planetary Science Letters 271, 311–325.

Lissenberg, C. J. & MacLeod, C. J. (2016). A Reactive Porous Flow Control on Mid-ocean Ridge Magmatic Evolution. Journal of Petrology. Oxford Academic 57, 2195–2220.

Maclennan, J., Hulme, T. & Singh, S. C. (2004). Thermal models of oceanic crustal accretion: Linking geophysical, geological and petrological observations. *Geochemistry, Geophysics, Geosystems* **5**.

Menke, W., West, M. & Tolstoy, M. (2002). Shallow-crustal magma chamber beneath the axial high of the Coaxial segment of Juan de Fuca Ridge at the source site of the 1993 eruption. *Geology*. GeoScienceWorld **30**, 359–362.

Meyer, P. S., Sigurdsson, H. & Schilling, J. (1985). Petrological and geochemical variations along Iceland's Neovolcanic Zones. *Journal of Geophysical Research: Solid Earth* **90**, 10043–10072.

Michael, P. J. & Cornell, W. C. (1998a). Influence of spreading rate and magma supply on crystallization and assimilation beneath mid-ocean ridges: Evidence from chlorine and major element chemistry of mid-ocean ridge basalts. *Journal of Geophysical Research: Solid Earth* **103**, 18325–18356.

Michael, P. J. & Cornell, W. C. (1998b). Influence of spreading rate and magma supply on crystallization and assimilation beneath mid-ocean ridges: Evidence from chlorine and major element chemistry of mid-ocean ridge basalts. *Journal of Geophysical Research: Solid Earth* **103**, 18325–18356.

Mørk, M. B. E. (1984). Magma mixing in the post-glacial veidivötn fissure eruption, southeast Iceland: a microprobe study of mineral and glass variations. *Lithos* **17**, 55–75.

Nagaoka, Y., Nishida, K., Aoki, Y., Takeo, M. & Ohminato, T. (2012). Seismic imaging of magma chamber beneath an active volcano. *Earth and Planetary Science Letters* **333–334**, 1–8.

Neave, D. A., Bali, E., Guðfinnsson, G. H., Halldórsson, S. A., Kahl, M., Schmidt, A.-S. & Holtz, F. (2019). Clinopyroxene–Liquid Equilibria and Geothermobarometry in Natural and Experimental Tholeiites: the 2014–2015 Holuhraun Eruption, Iceland. *Journal of Petrology* **60**, 1653–1680.

Neave, D. A., Maclennan, J., Thordarson, T. & Hartley, M. E. (2015). The evolution and storage of primitive melts in the Eastern Volcanic Zone of Iceland: the 10 ka Grímsvötn tephra series (i.e. the Saksunarvatn ash). *Contributions to Mineralogy and Petrology* **170**, 21.

Neave, D. A. & Putirka, K. D. (2017). A new clinopyroxene-liquid barometer, and implications for magma storage pressures under Icelandic rift zones. *American Mineralogist* **102**, 777–794.

Nedimović, M. R., Carbotte, S. M., Harding, A. J., Detrick, R. S., Canales, J. P., Diebold, J. B., Kent, G. M., Tischer, M. & Babcock, J. M. (2005a). Frozen magma lenses below the oceanic crust. *Nature* **436**, 1149.

Nedimović, M. R., Carbotte, S. M., Harding, A. J., Detrick, R. S., Canales, J. P., Diebold, J. B., Kent, G. M., Tischer, M. & Babcock, J. M. (2005b). Frozen magma lenses below the oceanic crust. *Nature*. Nature Publishing Group **436**, 1149–1152.

Nooner, S. L. & Chadwick, W. W. (2016). Inflation-predictable behavior and co-eruption deformation at Axial Seamount. *Science*. American Association for the Advancement of Science **354**, 1399–1403.

O'Hara, M. J. (1968). The bearing of phase equilibria studies in synthetic and natural systems on the origin and evolution of basic and ultrabasic rocks. *Earth-Science Reviews* **4**, 69–133.

Pan, Y. & Batiza, R. (2002). Mid-ocean ridge magma chamber processes: Constraints from olivine zonation in lavas from the East Pacific Rise at 9°30′N and 10°30′N. *Journal of Geophysical Research: Solid Earth* **107**, ECV 9-1-ECV 9-13.

Pan, Y. & Batiza, R. (2003). Magmatic processes under mid-ocean ridges: A detailed mineralogic study of lavas from East Pacific Rise 9°30′N, 10°30′N, and 11°20′N. *Geochemistry, Geophysics, Geosystems* **4**.

Putirka, K. (1999). Clinopyroxene + liquid equilibria to 100 kbar and 2450 K. *Contributions to Mineralogy and Petrology* **135**, 151–163.

Putirka, K. D. (2005). Mantle potential temperatures at Hawaii, Iceland, and the mid-ocean ridge system, as inferred from olivine phenocrysts: Evidence for thermally driven mantle plumes. *Geochemistry, Geophysics, Geosystems* **6**.

Putirka, K. D. (2008). Thermometers and Barometers for Volcanic Systems. *Reviews in Mineralogy and Geochemistry*. GeoScienceWorld **69**, 61–120.

Putirka, K., Johnson, M., Kinzler, R., Longhi, J. & Walker, D. (1996). Thermobarometry of mafic igneous rocks based on clinopyroxene-liquid equilibria, 0–30 kbar. *Contributions to Mineralogy and Petrology* **123**, 92–108.

Rhodes, J. M., Morgan, C. & Liias, R. A. (1990). Geochemistry of axial seamount lavas: Magmatic relationship between the Cobb Hotspot and the Juan de Fuca Ridge. *Journal of Geophysical Research: Solid Earth* **95**, 12713–12733.

Rubin, K. H., Sinton, J. M., Maclennan, J. & Hellebrand, E. (2009). Magmatic filtering of mantle compositions at mid-ocean-ridge volcanoes. *Nature Geoscience*. Nature Publishing Group **2**, 321–328.

Scott, J. L. (2017). Towards a petrologically constrained thermal model of mid-ocean ridges. Columbus, Ohio State University.

Scott, S. R., Ramos, F. C. & Gill, J. B. (2018). Spreading Dynamics of an Intermediate Ridge: Insights from U-series Disequilibria, Endeavour Segment, Juan de Fuca Ridge. Journal of Petrology 59, 1847–1868.

Shen, Y. & Forsyth, D. W. (1995). Geochemical constraints on initial and final depths of melting beneath mid-ocean ridges. *Journal of Geophysical Research: Solid Earth* **100**, 2211–2237.

Sinton, J. M. & Detrick, R. S. (1992). Mid-ocean ridge magma chambers. *Journal of Geophysical Research: Solid Earth* **97**, 197–216.

Smith, M. C., Perfit, M. R. & Jonasson, I. R. (1994). Petrology and geochemistry of basalts from the southern Juan de Fuca Ridge: Controls on the spatial and temporal evolution of mid-ocean ridge basalt. *Journal of Geophysical Research: Solid Earth* **99**, 4787–4812.

Soule, D., Wilcock, W. S. D., Toomey, D. R., Hooft, E. E. E. & Weekly, R. T. (2016). Near-axis crustal structure and thickness of the Endeavour Segment, Juan de Fuca Ridge: Crustal Structure at Endeavour Segment. *Geophysical Research Letters* **43**, 5688–5695.

Stakes, D. S., Perfit, M. R., Tivey, M. A., Caress, D. W., Ramirez, T. M. & Maher, N. (2006). The Cleft revealed: Geologic, magnetic, and morphologic evidence for construction of upper oceanic crust along the southern Juan de Fuca Ridge. *Geochemistry, Geophysics, Geosystems* **7**.

Turcotte, D. L. & Schubert, G. (2002). Plate Tectonics. *Geodynamics*. Cambridge University Press, 1–72.

Van Ark, E. M. et al. (2007). Seismic structure of the Endeavour Segment, Juan de Fuca Ridge: Correlations with seismicity and hydrothermal activity. *Journal of Geophysical Research* **112**.

Villiger, S., Müntener, O. & Ulmer, P. (2007). Crystallization pressures of mid-ocean ridge basalts derived from major element variations of glasses from equilibrium and fractional crystallization experiments. *Journal of Geophysical Research* **112**, B01202.

Wagoner, N. A. V. & Leybourne, M. I. (1991). Evidence for magma mixing and a heterogeneous mantle on the West Valley Segment of the Juan de Fuca Ridge. *Journal of Geophysical Research: Solid Earth* **96**, 16295–16318.

Wanless, V. D. & Behn, M. D. (2017). Spreading rate-dependent variations in crystallization along the global mid-ocean ridge system. *Geochemistry, Geophysics, Geosystems* **18**, 3016–3033.

Wanless, V. D., Perfit, M. R., Ridley, W. I. & Klein, E. (2010). Dacite Petrogenesis on Mid-Ocean Ridges: Evidence for Oceanic Crustal Melting and Assimilation. *Journal of Petrology*. Oxford Academic **51**, 2377–2410.

Wanless, V. D., Perfit, M. R., Ridley, W. I., Wallace, P. J., Grimes, C. B. & Klein, E. M. (2011). Volatile abundances and oxygen isotopes in basaltic to dacitic lavas on mid-ocean ridges: The role of assimilation at spreading centers. *Chemical Geology* **287**, 12.

Wanless, V. D. & Shaw, A. M. (2012). Lower crustal crystallization and melt evolution at mid-ocean ridges. *Nature Geoscience*. Nature Publishing Group **5**, 651–655.

Weaver, S. J. & Langmuir, C. H. (1990). Calculation of phase equilibrium in mineral-melt systems. *Computers & Geosciences* **16**, 1–19.

West, M., Menke, W. & Tolstoy, M. (2003). Focused magma supply at the intersection of the Cobb hotspot and the Juan de Fuca ridge. *Geophysical Research Letters* **30**.

West, M., Menke, W., Tolstoy, M., Webb, S. & Sohn, R. (2001). Magma storage beneath Axial volcano on the Juan de Fuca mid-ocean ridge. *Nature*. Nature Publishing Group **413**, 833–836.

Wilson, D. S. (1988). Tectonic history of the Juan de Fuca Ridge over the last 40 million years. *Journal of Geophysical Research: Solid Earth* **93**, 11863–11876.

Yang, A. Y., Wang, C., Liang, Y. & Lissenberg, C. J. (2019). Reaction Between Mid-Ocean Ridge Basalt and Lower Oceanic Crust: An Experimental Study. *Geochemistry, Geophysics, Geosystems* **20**, 4390–4407.

Yang, HJ., Kinzler, R. J. & Grove, T. L. (1996). Experiments and models of anhydrous, basaltic olivine-plagioclase-augite saturated melts from 0.001 to 10 kbar. *Contributions to Mineralogy and Petrology* **124**, 1–18.

Yoder, H. S. & Tilley, C. E. (1962). Origin of Basalt Magmas: An Experimental Study of Natural and Synthetic Rock Systems. *Journal of Petrology*. Oxford Academic **3**, 342–532.

Zhao, D. (2007). Seismic images under 60 hotspots: Search for mantle plumes. *Gondwana Research* **12**, 335–355.

Appendix A. Hartley et al. (2018) Modified Python Script

```
#!/usr/bin/env python3
# -*- coding: utf-8 -*-
"""
LH Anaconda Created on Wed Jan 29 11:03:22 2020

"""
# -*- coding: utf-8 -*-
"""
Created on Wed May 18 16:35:19 2016

@author: johnmaclennan, mhartley
This code is designed to read in table of observed compositional data
For each composition, it will estimate likelihood as function of pressure
by minimising misfit to observed XAl, XCa, XMg
using the parameterisation from Yang et al.

"""

import numpy as np
import matplotlib.pyplot as plt
from scipy.stats import chi2
global my_dtype,molwt,catnum,catwt

##################
#INPUT#
all_data = np.genfromtxt('MI_CORR_holu-
HartleyPublished.csv',delimiter=',',names=True,dtype=None)

sampleNames = all_data['Comment']
sampleNames = sampleNames.tolist()

##################


##################
# turn weight percent oxides into mole fractions
names=['SiO2', 'TiO2', 'Al2O3', 'FeO', 'Fe2O3', 'MgO', 'MnO', 'CaO', 'Na2O', 'K2
O', 'P2O5','Cr2O3']
formats=['<f8','<f8','<f8', '<f8', '<f8', '<f8', '<f8', '<f8', '<f8', '<f8', '<f
8', '<f8']
my_dtype = dict(names=names, formats=formats)
molwt = np.array([(60.08,79.866,101.96,71.844,159.69,40.3044,70.9374,56.0774,61.
9789,94.20,283.89,151.99)],dtype=my_dtype)
catnum = np.array([(1.,1.,2.,1.,2.,1.,1.,1.,2.,2.,2.,2.)],dtype=my_dtype)
catwt = np.zeros_like(molwt) # mol weight of oxide with single cation in formula
 unit
```

```
for n in my_dtype['names']:
    catwt[n] = molwt[n]/catnum[n] # Beattie style single cation molar fracs
##################


##################
def wt2cat (majwt):
    "Converts wt% oxides into atomic% of cation"
    tosum = np.zeros_like(molwt)
    molsum = 0.
    for n in my_dtype['names']:
        tosum[n] = majwt[n]/catwt[n]
        molsum = molsum + tosum[n]
    catfrac = np.zeros_like(molwt) # mol weight of oxide with single cation in f
ormula unit
    for n in my_dtype['names']:
        catfrac[n] = tosum[n]/molsum
    return (catfrac)
##################

##################
def xpred (p,xna,xk,xti,xfe,xsi):
    "calculate XAl,XCa,XMg for Yang model"

    xalp = 0.236 + 0.00218*p + 0.109*xna + 0.593*xk -0.350*xti -0.299*xfe -
 0.130*xsi
    xcap = 1.133 - 0.00339*p -0.569*xna -0.776*xk-0.672*xti-0.214*xfe-
3.355*xsi + 2.830*(xsi*xsi)
    xmgp = -0.277 + 0.00114*p -0.543*xna -0.947*xk -0.117*xti-
0.490*xfe+2.086*xsi -2.400*(xsi*xsi) # original from Yang

    return(xalp,xcap,xmgp)
#################


#################
pprob = np.array(0)
ppmin = np.array(0)


for nsam in range(0,len(all_data)):
    maj_data = np.array([all_data[nsam,]],dtype=all_data.dtype)
    xobs = wt2cat(maj_data)
    xalo,xcao,xmgo = xobs['Al2O3'],xobs['CaO'],xobs['MgO']
    # 5% precision on major elements in glasses - 1 sig -
 estimate from NEAVE et al., 2015
    xals,xcas,xmgs = 0.05*xalo,0.05*xcao,0.05*xmgo
    xna,xk,xti,xfe,xsi = xobs['Na2O'],xobs['K2O'],xobs['TiO2'],xobs['FeO'],xobs[
'SiO2']

    cp = np.array(0)
    pp = np.array(0)
    for npres in range(-500,1500):
        pkbar = npres/100.
        xalp,xcap,xmgp = xpred(pkbar,xna,xk,xti,xfe,xsi)
       #### chi2 ######
```

```
92.         chi2o =((xalo-xalp)/xals)**2. + ((xcao-xcap)/xcas)**2. + ((xmgo-
    xmgp)/xmgs)**2.
93.         cp = np.append(cp,chi2o)
94.         pp = np.append(pp,pkbar)
95.
96.     cp = cp[1:]
97.     pp = pp[1:]
98.
99.     cpmin = np.amin(cp)
100.            prob = 1- chi2.cdf(cpmin,2) # signifance value
101.            pmin = pp[np.argmin(cp)] # pressure at minimum
102.            pprob = np.append(pprob,prob)
103.            ppmin = np.append(ppmin,pmin)
104.
105.        pprob = pprob[1:]
106.        ppmin = ppmin[1:]
107.        ###################
108.
109.
110.        ### EXPORT ###
111.
112.        # export all output data
113.        np.savetxt('pf-all.out', pprob)
114.        np.savetxt('MICORR_pressure-all.out', ppmin)
115.
116.        ### filter for high probability fits
117.        np.savetxt('pf-good.out', pprob[np.where(pprob > 0.8)])
118.        np.savetxt('MICORR_pressure-good.out', ppmin[np.where(pprob > 0.8)])
119.
120.        ###Saving Sample Names with Good Pressures, inserting NULL for filtered
    
121.        finalNameList = [0] * len(sampleNames)
122.        finalPkbarList = [0] * len(sampleNames)
123.        for i in range(0,len(sampleNames)):
124.            if pprob[i] > 0.8:
125.                finalNameList[i] = sampleNames[i]
126.                finalPkbarList[i] = ppmin[i]
127.            else:
128.                finalNameList[i] = ['NULL']
129.                finalPkbarList[i] = 'NULL'
130.
131.        np.savetxt('name-good.out', finalPkbarList, fmt="%s")
132.
133.        #################
```

Appendix B: Effect of Changing Error for H18 Method

A link to the data file with the full data can be found in Appendix F.

H18 5% error Pressure Results			**H18 1%, 1%, 0.7% Error Pressure Results**		
NULL = pressure removed for poor fit			NULL = pressure removed for poor fit		
P_kbar 5%	model fit (>0.8 is good)	P (kbar) Filtered	P_kbar Adj%	model fit (>0.8 is good)	P (kbar) Filtered
6.38	0.96	6.38	6.32	0.32	NULL
0.81	0.99	0.81	0.86	0.71	NULL
1.06	0.70	NULL	1.38	0.00	NULL
1.67	0.68	NULL	1.37	0.00	NULL
0.55	0.87	0.55	0.77	0.00	NULL
1.09	0.97	1.09	1.19	0.29	NULL
1.54	0.93	1.54	1.44	0.10	NULL
1.33	0.58	NULL	1.00	0.00	NULL
1.16	0.79	NULL	1.44	0.00	NULL
1.85	0.82	1.85	1.62	0.00	NULL
-0.03	0.75	NULL	0.28	0.00	NULL
2.77	1.00	2.77	2.79	0.90	2.79
1.33	0.71	NULL	1.65	0.00	NULL
1.22	0.84	1.22	1.02	0.00	NULL
1.95	0.99	1.95	2.00	0.77	NULL
2.92	0.99	2.92	2.86	0.58	NULL
1.63	0.57	NULL	1.24	0.00	NULL
1.59	0.80	1.59	1.34	0.00	NULL
6.38	0.96	6.38	6.32	0.32	NULL
0.81	0.99	0.81	0.86	0.71	NULL
1.06	0.70	NULL	1.38	0.00	NULL
1.67	0.68	NULL	1.37	0.00	NULL
0.55	0.87	0.55	0.77	0.00	NULL
1.09	0.97	1.09	1.19	0.29	NULL
1.54	0.93	1.54	1.44	0.10	NULL
1.30	0.59	NULL	0.99	0.00	NULL

Continued from previous page						
H18 5% error Pressure Results			**H18 1%, 1%, 0.7% Error Pressure Results**			
NULL = pressure removed for poor fit			NULL = pressure removed for poor fit			
P_kbar 5%	model fit (>0.8 is good)	P (kbar) Filtered	P_kbar Adj%	model fit (>0.8 is good)	P (kbar) Filtered	
1.16	0.79	NULL	1.44	0.00	NULL	
1.79	0.82	1.79	1.60	0.00	NULL	
-0.03	0.75	NULL	0.28	0.00	NULL	
2.77	1.00	2.77	2.79	0.90		2.79
1.33	0.71	NULL	1.65	0.00	NULL	
1.16	0.84	1.16	1.00	0.00	NULL	
1.95	0.99	1.95	2.00	0.77	NULL	
2.92	0.99	2.92	2.86	0.58	NULL	
1.58	0.58	NULL	1.22	0.00	NULL	
1.59	0.80	1.59	1.34	0.00	NULL	
-0.72	0.92	-0.72	-0.79	0.11	NULL	
0.15	0.46	NULL	-0.32	0.00	NULL	
1.40	0.95	1.4	1.40	0.31	NULL	
2.17	0.86	2.17	1.99	0.00	NULL	
-1.39	0.06	NULL	-2.35	0.00	NULL	
1.50	0.56	NULL	1.10	0.00	NULL	
1.07	0.16	NULL	0.32	0.00	NULL	
-0.29	0.28	NULL	-0.89	0.00	NULL	
-0.13	0.10	NULL	-0.92	0.00	NULL	
-0.68	0.02	NULL	-1.73	0.00	NULL	
1.15	0.56	NULL	0.75	0.00	NULL	
0.46	0.06	NULL	-0.40	0.00	NULL	
-0.01	0.23	NULL	-0.60	0.00	NULL	
-0.04	0.57	NULL	-0.46	0.00	NULL	
1.97	0.63	NULL	2.32	0.00	NULL	
1.66	0.90	1.66	1.84	0.01	NULL	
2.82	0.98	2.82	2.90	0.37	NULL	
1.48	0.86	1.48	1.70	0.00	NULL	
2.70	1.00	2.7	2.73	0.86		2.73
2.56	0.65	NULL	2.92	0.00	NULL	
0.71	0.61	NULL	0.35	0.00	NULL	
0.82	0.81	0.82	0.58	0.00	NULL	
0.81	0.87	0.81	0.63	0.01	NULL	
0.92	0.92	0.92	0.78	0.05	NULL	

Continued from previous page						
H18 5% error Pressure Results			**H18 1%, 1%, 0.7% Error Pressure Results**			
NULL = pressure removed for poor fit			NULL = pressure removed for poor fit			
P_kbar 5%	model fit (>0.8 is good)	P (kbar) Filtered	P_kbar Adj%	model fit (>0.8 is good)	P (kbar) Filtered	
1.50	0.80	1.5	1.27	0.00	NULL	
-0.31	0.93	-0.31	-0.16	0.05	NULL	
0.56	0.99	0.56	0.51	0.64	NULL	
0.77	0.66	NULL	0.43	0.00	NULL	
-0.70	1.00	-0.7	-0.70	0.98		-0.7
1.04	0.68	NULL	0.73	0.00	NULL	
0.41	0.99	0.41	0.48	0.60	NULL	
0.42	0.84	0.42	0.64	0.00	NULL	
0.55	0.95	0.55	0.67	0.13	NULL	
0.28	0.61	NULL	-0.09	0.00	NULL	
0.72	0.46	NULL	0.26	0.00	NULL	
0.53	0.66	NULL	0.20	0.00	NULL	
0.66	0.87	0.66	0.48	0.01	NULL	
0.00	0.99	0	0.06	0.61	NULL	
-0.10	0.89	-0.1	-0.27	0.01	NULL	
-0.09	0.93	-0.09	0.06	0.05	NULL	
0.13	0.99	0.13	0.10	0.77	NULL	
1.29	0.60	NULL	0.91	0.00	NULL	
1.70	0.65	NULL	1.34	0.00	NULL	
1.03	0.68	NULL	0.70	0.00	NULL	
1.25	0.56	NULL	0.82	0.00	NULL	
1.04	0.50	NULL	0.59	0.00	NULL	
1.15	1.00	1.15	1.18	0.93		1.18
0.88	0.15	NULL	1.58	0.00	NULL	
0.38	0.93	0.38	0.53	0.05	NULL	
0.94	0.80	NULL	0.69	0.00	NULL	
0.41	0.31	NULL	-0.18	0.00	NULL	
1.25	0.83	1.25	1.03	0.00	NULL	
0.53	0.65	NULL	0.19	0.00	NULL	
0.65	0.06	NULL	-0.36	0.00	NULL	
0.63	0.11	NULL	-0.25	0.00	NULL	
0.65	0.35	NULL	0.10	0.00	NULL	
2.77	0.98	2.77	2.72	0.50	NULL	
4.46	0.97	4.46	4.55	0.33	NULL	

Continued from previous page						
H18 5% error Pressure Results				**H18 1%, 1%, 0.7% Error Pressure Results**		
NULL = pressure removed for poor fit				NULL = pressure removed for poor fit		
P_kbar 5%	model fit (>0.8 is good)	P (kbar) Filtered		P_kbar Adj%	model fit (>0.8 is good)	P (kbar) Filtered
5.50	0.02	NULL		6.35	0.00	NULL
5.23	0.94		5.23	5.13	0.10	NULL
4.61	0.97		4.61	4.53	0.34	NULL
4.81	0.91		4.81	5.00	0.02	NULL
2.26	0.10	NULL		1.32	0.00	NULL
2.52	0.10	NULL		1.60	0.00	NULL
3.28	0.29	NULL		2.63	0.00	NULL
2.85	0.97		2.85	2.78	0.35	NULL
3.06	0.94		3.06	3.20	0.08	NULL
3.04	0.30	NULL		3.59	0.00	NULL
0.55	0.00	NULL		-0.76	0.00	NULL
2.73	0.59	NULL		3.12	0.00	NULL
2.73	0.89		2.73	2.94	0.01	NULL
1.67	0.70	NULL		1.36	0.00	NULL
1.92	0.46	NULL		1.46	0.00	NULL
2.05	0.81		2.05	1.82	0.00	NULL
1.69	0.81		1.69	1.95	0.00	NULL
1.15	0.98		1.15	1.08	0.43	NULL
2.10	0.74	NULL		2.40	0.00	NULL
0.61	0.62	NULL		0.24	0.00	NULL
1.78	0.09	NULL		0.92	0.00	NULL
3.40	0.83		3.4	3.19	0.00	NULL
3.63	0.58	NULL		3.24	0.00	NULL
1.44	0.23	NULL		0.76	0.00	NULL
0.34	0.16	NULL		-0.41	0.00	NULL
-0.28	0.03	NULL		-1.37	0.00	NULL
3.62	0.70	NULL		3.31	0.00	NULL
3.07	0.33	NULL		2.50	0.00	NULL
2.63	0.31	NULL		2.04	0.00	NULL
1.08	0.10	NULL		0.21	0.00	NULL
3.14	0.57	NULL		2.74	0.00	NULL
3.56	0.41	NULL		3.03	0.00	NULL
1.31	0.19	NULL		0.58	0.00	NULL
0.77	0.09	NULL		-0.11	0.00	NULL

Continued from previous page						
H18 5% error Pressure Results				**H18 1%, 1%, 0.7% Error Pressure Results**		
NULL = pressure removed for poor fit				NULL = pressure removed for poor fit		
P_kbar 5%	model fit (>0.8 is good)	P (kbar) Filtered		P_kbar Adj%	model fit (>0.8 is good)	P (kbar) Filtered
2.89	0.48	NULL		2.43	0.00	NULL
1.75	0.60	NULL		1.38	0.00	NULL
4.38	0.97		4.38	4.29	0.27	NULL
2.19	0.58	NULL		1.79	0.00	NULL
3.06	0.69	NULL		2.74	0.00	NULL
3.42	0.69	NULL		3.11	0.00	NULL
2.52	0.65	NULL		2.18	0.00	NULL
3.32	0.46	NULL		2.84	0.00	NULL
2.42	0.77	NULL		2.16	0.00	NULL
-0.05	0.72	NULL		-0.35	0.00	NULL
2.73	0.31	NULL		2.12	0.00	NULL
3.43	0.33	NULL		2.83	0.00	NULL
4.19	0.93		4.19	4.34	0.05	NULL
0.77	0.30	NULL		0.15	0.00	NULL
1.14	0.79	NULL		0.89	0.00	NULL
4.45	0.47	NULL		4.88	0.00	NULL
2.65	0.75	NULL		2.37	0.00	NULL
4.44	0.98		4.44	4.39	0.52	NULL
0.87	0.13	NULL		0.04	0.00	NULL
2.70	0.84		2.7	2.49	0.00	NULL
1.52	0.97		1.52	1.46	0.39	NULL
2.01	0.98		2.01	2.10	0.36	NULL
2.13	0.97		2.13	2.05	0.35	NULL
3.49	0.64	NULL		3.15	0.00	NULL
3.33	0.64	NULL		2.98	0.00	NULL
4.01	0.96		4.01	3.92	0.23	NULL
0.63	0.77	NULL		0.35	0.00	NULL
2.92	0.70	NULL		2.59	0.00	NULL
2.66	0.97		2.66	2.58	0.38	NULL
2.97	0.52	NULL		2.53	0.00	NULL
6.68	0.05	NULL		7.45	0.00	NULL
4.51	0.55	NULL		4.90	0.00	NULL
2.97	0.99		2.97	3.01	0.79	NULL
2.60	0.75	NULL		2.88	0.00	NULL

Continued from previous page

H18 5% error Pressure Results				H18 1%, 1%, 0.7% Error Pressure Results			
NULL = pressure removed for poor fit				NULL = pressure removed for poor fit			
P_kbar 5%	model fit (>0.8 is good)	P (kbar) Filtered		P_kbar Adj%	model fit (>0.8 is good)	P (kbar) Filtered	
5.27	0.96		5.27	5.40	0.16	NULL	
6.24	0.02	NULL		7.10	0.00	NULL	
5.01	0.97		5.01	5.12	0.26	NULL	
2.10	0.76	NULL		2.37	0.00	NULL	
2.21	0.98		2.21	2.14	0.48	NULL	
2.69	0.92		2.69	2.85	0.03	NULL	
2.65	0.98		2.65	2.62	0.63	NULL	
2.96	0.87		2.96	3.16	0.00	NULL	
2.87	1.00		2.87	2.86	0.98		2.86
4.79	0.99		4.79	4.86	0.57	NULL	
5.28	0.07	NULL		6.06	0.00	NULL	
4.01	0.71	NULL		4.34	0.00	NULL	
3.51	0.65	NULL		3.86	0.00	NULL	
-1.41	0.03	NULL		-2.59	0.00	NULL	
2.73	0.97		2.73	2.65	0.37	NULL	
4.32	0.97		4.32	4.23	0.27	NULL	
3.66	0.80		3.66	3.40	0.00	NULL	
2.32	0.97		2.32	2.23	0.33	NULL	
3.96	1.00		3.96	3.98	0.91		3.98
3.49	0.91		3.49	3.32	0.03	NULL	
3.35	0.68	NULL		3.69	0.00	NULL	
4.47	1.00		4.47	4.49	0.93		4.49
2.42	0.40	NULL		1.86	0.00	NULL	
4.14	0.75	NULL		4.45	0.00	NULL	
2.23	0.91		2.23	2.07	0.03	NULL	
4.24	1.00		4.24	4.28	0.83		4.28
2.06	0.29	NULL		1.38	0.00	NULL	
2.93	0.43	NULL		2.39	0.00	NULL	
2.33	0.96		2.33	2.24	0.28	NULL	
2.94	0.35	NULL		2.31	0.00	NULL	
3.66	0.74	NULL		3.96	0.00	NULL	
2.42	0.58	NULL		2.82	0.00	NULL	
2.09	0.62	NULL		2.46	0.00	NULL	
2.14	0.54	NULL		2.57	0.00	NULL	

Continued from previous page						
H18 5% error Pressure Results			**H18 1%, 1%, 0.7% Error Pressure Results**			
NULL = pressure removed for poor fit			NULL = pressure removed for poor fit			
P_kbar 5%	model fit (>0.8 is good)	P (kbar) Filtered	P_kbar Adj%	model fit (>0.8 is good)	P (kbar) Filtered	
3.99	0.37	NULL	4.53	0.00	NULL	
6.63	0.00	NULL	7.83	0.00	NULL	
6.57	0.00	NULL	7.78	0.00	NULL	
1.88	0.64	NULL	2.25	0.00	NULL	
-2.53	0.01	NULL	-4.03	0.00	NULL	
5.88	0.00	NULL	7.07	0.00	NULL	
-1.90	0.14	NULL	-2.78	0.00	NULL	
5.01	0.00	NULL	6.25	0.00	NULL	
3.87	0.19	NULL	4.49	0.00	NULL	
4.05	0.54	NULL	4.43	0.00	NULL	
4.68	0.07	NULL	5.41	0.00	NULL	
2.57	0.89	2.57	2.39	0.01	NULL	
4.74	0.09	NULL	5.46	0.00	NULL	
3.66	0.44	NULL	4.13	0.00	NULL	
3.55	0.59	NULL	3.94	0.00	NULL	
4.43	0.37	NULL	4.97	0.00	NULL	
2.67	0.94	2.67	2.81	0.10	NULL	
2.09	0.98	2.09	2.18	0.42	NULL	
2.49	0.98	2.49	2.58	0.35	NULL	
2.79	0.44	NULL	2.31	0.00	NULL	
3.92	0.99	3.92	3.97	0.72	NULL	
3.58	0.99	3.58	3.57	0.86		3.57
3.46	0.99	3.46	3.53	0.54	NULL	

Summary:

	5% Error		**Adjusted Error***	
	Unfiltered H18 P (kbar)	Filtered H18 P (kbar)	Unfiltered H18 P (kbar)	Filtered H18 P (kbar)
# Samples	**219**	**93**	**219**	**10**

*σ = 1% For Al2O3, 1% for CaO, 0.7% for MgO

Table A.1: H18 Pressures with 5% error (left) and modified error (right). Modification of the error used in the pressure calculation does not alter the pressure results significantly, however it greatly reduces the number of samples in the filtered dataset.

Appendix C. Major Element PetDb.org Download Parameters

The data were downloaded from PetDb.org database (wwww.earthchem.org/petdb) on 29 of September 2009, using the parameters: Spreading center: Juan de Fuca Ridge and rock classification=igneous: volcanic: mafic: glasses.

The sources of analyses included in this download are: Moore (1970), Barr and Chase (1974), Delaney et al. (1978), Cohen et al. (1980), Ito et al. (1980), Eaby et al. (1984), Christie et al. (1986), Dixon et al. (1986), Liias (1986), Ryan and Langmuir (1987), Dixon et al. (1988), Karsten et al. (1990), Rhodes et al. (1990), Van Wagoner and Leybourne (1991), Wallace et al. (1992), Smith et al. (1994), Cousens et al. (1995), Gaetani et al. (1995), Michael (1995), Melson and O'Hearn (2003), Bezos and Humler (2005), Stakes et al. (2006), Cordier et al. (2007), and Gale et al. (2013)

Appendix D. $Temp_{8.0}$, $Water_{8.0}$, $Fe_{8.0}$, & $Na_{8.0}$ Calculation

$Temp_{8.0}$ normalization corrects for the loss of heat as a magma fractionates to MgO lower than 8.0 wt. %, which allows for the comparison of temperatures along the ridge despite variances in the degree of fractionation. This method is adapted from the method described by Klein & Langmuir (1987) and Langmuir et al. (1992) for $Na_{8.0}$. To perform this calculation, a regression line is fit to a plot of MgO vs. Temperature using the CoHort 6.451 software. The analysis of variance (ANOVA) was performed though the CoStat 6.451 package. The zero P value of for a 1-degree (linear) polynomial indicates that the regression is a good fit. This slope of this regression is used in the following equation to calculate the $Temp_{8.0}$ values:

$$Temp_{8.0} = Temp°C - (10.77 \pm 0.48) * (MgO) + (86.16 \pm 3.84)$$

The reported errors are at the 95% confidence level.

Similarly, water, iron, and sodium are normalized to $Water_{8.0}$, $Fe_{8.0}$, & $Na_{8.0}$ using the equations:

$$H_2O_{8.0} = H_2O_{est} + (0.04 \pm 0.00) * (MgO) - (0.03)$$

$$Na_{8.0} = \mathrm{Na_2}O + (0.15 \pm 0.0) * (MgO) - (1.2)$$

$$Fe_{8.0} = \mathrm{FeO} + (1.19 \pm 0.05) * (MgO) - (9.52)$$

The reported errors are at the 95% confidence level.

Appendix E. Wt.% Water PetDb.org Download Parameters

Water data were downloaded from PetDb.org database

(wwww.earthchem.org/petdb) in two downloads using the following parameters:

Download 1:

Search Criteria:
Longitude/Latitude: NORTH: 49.19 SOUTH: 44.00 WEST: -132.46 EAST: -125.87
Class: All
Alteration: Fresh

Download 2:

Search Criteria:
Polygon: -131.209716796293 49.2767068761308; -127.935791015059 48.8362702190824; -130.045166015049 43.881861304285; -130.880126952551 44.1830518614606; -128.924560546312 48.9377011620857; -128.935546874432 48.9521744057527; -129.122314452561 48.9449383116638
Materials: Igneous

Appendix F. Link to Data Files

Data used for this study can be found at the following link:

https://osu.box.com/v/LHernandezMSDatafiles